NTNU
Norwegian University of
Science and Technology

Modelling of spectroscopic Mueller matrices of ordered nanoplasmonic surfaces using the finite element method

Brage Bøe Svendsen

MSc in Physics
Submission date: August 2017
Supervisor: Morten Kildemo, IFY

Norwegian University of Science and Technology
Department of Physics

Abstract

This thesis is focused on modelling the complete polarization dependent optical response resulting from reflection from periodic nanostructures with a two-dimensional lattice, using the commercial software COMSOL Multiphysics based on the finite element method. An efficient model exploring the COMSOL wave optics module has been developed and the results have been successfully compared to the experimentally recorded Mueller matrices of plasmonic nanostructures previously manufactured in NTNU NanoLab. Three different samples have been targeted, consisting of plasmonic hemispheroidal nanoparticles in square or rectangular lattices on a SiO_2 substrate. The size and shape of the nanoparticles were different for each sample. Their rich optical response, including localized surface plasmon resonances (LSPR), polarization coupling, and strong dependency on Rayleigh anomalies, were reproduced by the COMSOL model. A similar model was further used to simulate a sample of densely packed tilted GaSb cones for photon energies beyond its corresponding experimental work, revealing a strong polarization coupling around 7.5 eV. Model efficiency was optimized to greatly reduce computation time and memory requirements. Further optimization measures have been suggested that could vastly improve performance, which in turn would open up possibilities of modeling more complex and computationally demanding systems.

Preface

This thesis has been carried out as part of the requirements for completing the 2-year master's degree program in physics at the Department of Physics of the Norwegian University of Science and Technology. The project was written under the supervision of Professor Morten Kildemo, starting in October 2016 and finished in August 2017.

I would like to sincerely thank Morten Kildemo for accepting me for this thesis topic, as well as PhD student Per Magnus Walmsness, for their continuous support during every stage of the project.

Brage Bøe Svendsen
Trondheim, Norway
August 2017

Table of Contents

Abbreviations

ABC Absorbing boundary layer

AFM Atomic-force microscopy

AOI Angle of incidence

BZ Brillouin Zone

EM Electromagnetic

EMA Effective medium approximation

EWFD Electromagnetic Waves

FEM Finite element method

FIB Focused ion beam

IR Infrared

LSPR Localized surface plasmon resonance

ME Maxwell’s equations

MES Maximum element size

MM Mueller matrix

PDE Partial differential equation

PML Perfectly matched layers

POI Plane of incidence

RAM Random access memory

RRE Reduced Rayleigh equation

SBC Scattering boundary condition

SEM Scanning electron microscopy

SPPR Surface plasmon polariton resonance

SPR Surface plasmon resonance

UV Ultraviolet

Chapter 1

Introduction

1.1 Background

Recent years have seen an intense research into plasmonics and applications, therein the development of the field of metamaterials and metasurfaces [60]. The main applications of nanoplasmonics is a result of so-called plasmon resonances which enables the ability to i) confine the electromagnetic field into subwavelength volumes, and to ii) enhance the field. In such resonant structures, timevarying electric fields associated with light waves exert a force on the gas of negatively charged electrons inside a metal and drive them into a collective oscillation. At specific frequencies this oscillation is resonantly driven to produce a very strong charge displacement and associated (light) field concentration, known as a localized surface plasmon resonance (LSPR). LSPRs and surface plasmon polaritons (SPP) confine the field near a particle or interface, which has applications ranging from sub-diffraction-limit imaging, through nanophotonics communications to photovoltaics. The design go well beyond simple non-interacting nanoparticles to e.g. structures such as plasmonic nano-antennas [60].

Further applications of this light manipulation can be found in photothermal cancer treatment, in vivo bio-imaging, catalysis, thermal emitters, nonlinear optics, photodetectors, and in engineering of radiative decay [34] [73]. In photovoltaics, plasmonic nanoparticles have shown potential in producing highly efficient solar cells while offering low materials and processing costs [73] [79] [75].

Plasmonics has also been a fundamental sub-unit in the design of the ”meta-atom” in metamaterials, not only supplying the negative dielectric function through metallic rods, but also supplying an effective negative permeability through e.g. split ring resonator designs [69]. Metamaterials unfortunately suffer from large losses and are extremely complicated to manufacture, but recently metasurfaces exploring a two-dimenional lattice of resonator units has become a promising field of research [60]. On the other hand, nanostructured surfaces made out of semiconducting materials are promising for applications within optical and optoelectronic applications such as highly absorbing solar cell units [77]. Modelling of such nanostructures has traditionally been limited to exploring the generalized effective medium theory. However, since effective medium theory relies on structures being much smaller than the wavelength of light (effectively in the quastistatic approximation), this approach is expected to break down for larger structures [3].

Since the plasmon excitation is polarization dependent [54], ellipsometry is a natural candidate for sample characterization as it exploits the polarization aspect of light. Spectroscopic ellipsometry is an established non-invasive method of retrieving valuable amplitude and phase information from metal-dielectric interfaces of thin films, from which one can determine the effective dielectric function and how it relates to the material nanostructure and define exactly the system's plasmonic characteristics [68].

Traditionally, the optical response has been modelled by a stack of plane layers. Nanostructured materials (with or without plasmonic nanoparticles) could be modelled in terms of the generalized effective medium theory, whereas the optical response of the layer can be modelled by an anisotropic layer [27]. The complexity of the structures, and that the dimensions are not strictly subwavelength makes the latter approach insufficient. This is where computational electromagnetics can help out. Furthermore, Mueller matrix ellipsometry covers the complete polarization response from such complex nanostructures. The modelling of the full Mueller matrix from nanostructured samples is the topic of this thesis.

There are several different methods in computational electromagnetics, each with their own advantages and disadvantages depending on the problem at hand [79]. For example, the discrete dipole approximation (DDA) computes electromagnetic scattering and absorption by targets of arbitrary shape, but is limited by requiring a interdipole separation small compared the structural lengths in the target and to the wavelength [19]. The finite difference time domain (FDTD) method has been extensively used in plasmonics [79]. In FDTD, the Maxwell's equations in their differential form are discretized in space and time and the time evolution of electromagnetic near-fields is calculated directly [76]. FDTD is an attractive method due to being relatively easy to implement for specific problems, however, resolving curved and triangular geometries can be challenging. The finite element method (FEM) is another full-wave differential equation solver, it discretizes the system volume into smaller, simpler parts that are numerically easier to solve. These subsets are then re-assembled into a larger system of equations that models the entire problem [42]. FEM is a mature method that is efficient and unconditionally stable[1] [72], and solving Maxwell's equations in the frequency domain allows direct comparison with ellipsometric characterization of experimental data. Another attractive feature is its ability to handle complicated geometries with relative ease, making FEM the numerical method of choice for this thesis.

1.2 Problem formulation

This thesis will investigate methods to simulate the optical properties of periodic metallic nanostructures at oblique angle of incidence using COMSOL Multiphysics with the wave optics module, a commercial finite element method software. There will be a focus on replicating the optical response of structures that have previously been fabricated in the

---

[1] That is, if a wavelength step-size no matter how large can be used without resulting in the type of nonsense results associated with a numerical instability.

NTNU NanoLab and characterized with angle-resolved spectroscopic Mueller matrix ellipsometry. If the model is verifiable through comparison with experimental data, it will be applied to simulate other structures.

1.3 Thesis overview

In the following chapter, an introduction to electromagnetic theory will be given; the polarization of light, Stokes-Mueller formalism, ellipsometry, and electromagnetic interaction with matter including surface plasmons and diffraction grating, before finally introducing the finite element method. Chapter 3 will present the various fabricated nanostructures to be modeled as well as a brief summary of their experimental background. The commercial FEM software COMSOL Multiphysics will be presented in chapter 4, beginning with a general overview of the program before delving further into the wave optics module used to simulate electromagnetic wave propagation. The results and discussion in chapter 5 will be divided into three main parts; a detailed explanation of the modeling process in COMSOL will be given first; next, measures taken to optimize the model and their effects on performance and accuracy are presented; lastly, the simulation results and analysis of each of the four samples are given. Conclusions and recommendations for future work will be given in chapter 6.

Chapter 2

Background Theory

2.1 Polarized light

Light, in accordance with Maxwell's equations, is described as a propagating electromagnetic (EM) wave with fundamental properties such as wavelength, intensity and polarization.

The electric field of a monochromatic plane wave that is completely polarized light and travelling in the $\hat{z}$ direction can be described as a decomposition into two orthogonal field components oscillating in the $\hat{x}$ and $\hat{y}$ directions,

$$\mathbf{E}(z,t) = E_{0x}\cos(\omega t - kz + \delta_x)\hat{\mathbf{x}} + E_{0y}\cos(\omega t - kz + \delta_y)\hat{\mathbf{y}} \tag{2.1}$$

where ω and k are the angular frequency and wave vector of the light, while δ and E_0 are phase and amplitude in their respective directions. In complex notation the field is described as

$$\mathbf{E}(z,t) = E_{0x}e^{i(\omega t - kz + \delta_x)}\hat{\mathbf{x}} + E_{0y}e^{i(\omega t - kz + \delta_y)}\hat{\mathbf{y}}, \tag{2.2}$$

where taking the real part of equation (2.2) results in the physical field. The magnetic field can be described in a similar manner. However, since the magnetic susceptibility of materials studied in this thesis is comparable to that of vacuum, it is usually sufficient to only account for the electric field.

Polarization of light is described by the electric field amplitude E_{0x}, E_{0y} and phase difference $\delta = \delta_x - \delta_y$. If the two components in equation (2.2) have different phases, the oscillating electric field will trace out an ellipse in the plane perpendicular to its direction of propagation. If, for example, $E_{0y} = 0$, the electric field will oscillate only in $\hat{x}$-direction and the light is said to be linearly horizontally polarized [29]. The time dependence in equation (2.2), $e^{(i\omega t)}$, is chosen so that in the case of elliptical polarized light, right circular polarization is defined as a clockwise rotation of the electric field when looking towards the source [32].

The polarization of an electromagnetic wave may also be described in complex vector notation by a so-called Jones vector,

$$\mathbf{E} = \begin{pmatrix} E_{0x} e^{i\delta_x} \\ E_{0y} e^{i\delta_y} \end{pmatrix} = \begin{pmatrix} E_x \\ E_y \end{pmatrix}, \tag{2.3}$$

where the propagator $\omega t - kz$ is usually suppressed when only polarization is of interest [29]. Again, restoring the propagator and taking the real part of equation (2.3) will result in the optical field. The total intensity of the optical field averaged over time is given by

$$I = E_x E_x^* + E_y E_y^*. \tag{2.4}$$

When describing the change of polarization of light after interaction with an optical element, e.g. reflection from a thin film, a Jones Matrix formulation may be used when assuming a linear relation between the components of the emerging beam and the incident beam,

$$\begin{pmatrix} E_x \\ E_y \end{pmatrix}_{out} = \begin{pmatrix} j_{11} & j_{12} \\ j_{21} & j_{22} \end{pmatrix} \begin{pmatrix} E_x \\ E_y \end{pmatrix}_{inc} \tag{2.5}$$

where the 2x2 matrix is called the Jones Matrix and its elements $j_{kl} \quad (k, l = 1, 2)$ are complex reflection or transmission coefficients translating linear interactions of completely polarized light. Reflectance or transmittance, which is the fraction of incident electromagnetic power that is reflected or transmitted by the optical element, is given by $J_{kl} = |j_{kl}|^2$.

2.2 Stokes-Mueller formalism

The Jones formalism provides a description of completely polarized light. However, often in nature and practical cases, light is not a perfectly monochromatic wave[1]. Sunlight, for example, is unpolarized light, meaning that the beam's polarization changes so quickly and randomly that it cannot be determined for any practical purposes. Real-world measurement systems and samples may cause a fraction of the light to become unpolarized. This process where the light's degree of polarization is reduced is called *depolarization*, and describes the percentage of light that has become unpolarized [2]. Another limitation of the Jones formalism regarding experimental work is that detectors measure light intensities, not field amplitudes. There is thus a practical motivation for an alternative representation of light in terms of intensities which also takes into account depolarization.

The Stokes-Mueller formalism may represent quasi-monochromatic light that is unpolarized, partially polarized or completely polarized. A quasi-monochromatic wave will have time-dependent phase factors $\delta_i(t)$ and amplitude $E_i(t)$ that fluctuate slowly compared to the rapid oscillations of the cosinusoids in equation (2.1) [29]. The Stokes vector provide a full description of any polarization state [4],

$$\begin{pmatrix} S_0 \\ S_1 \\ S_2 \\ S_3 \end{pmatrix} = \begin{pmatrix} < E_{0x}(t)^2 > + < E_{0y}(t)^2 > \\ < E_{0x}(t)^2 > - < E_{0y}(t)^2 > \\ 2 < E_{0x}(t) E_{0y}(t) \cos[\delta_y(t) - \delta_x(t)] > \\ 2 < E_{0x}(t) E_{0y}(t) \sin[\delta_y(t) - \delta_x(t)] > \end{pmatrix} = \begin{pmatrix} I_x + I_y \\ I_x - I_y \\ I_{+45^\circ} - I_{-45^\circ} \\ I_r - I_l \end{pmatrix}, \tag{2.6}$$

---

[1] A wave is monochromatic if amplitude and phase factors are constant for all time, as in section 2.1.

where $< ... >$ denotes the time-average, so that S_0 represents the total intensity of the light beam, S_1 is the intensity difference between horizontally and vertically polarized light, and S_2 the difference between $+45°$ and $-45°$ polarized light. Finally S_3 is the difference between right handed and left handed circularly polarized light. Whereas the Jones vector represent light with field amplitude and phase, the Stokes vector represent light with field intensities.

The degree of polarization P is defined as the ratio between the intensity of completely polarized light to the total intensity of the beam. In terms of Stokes parameters this is

$$P = \frac{\sqrt{S_1^2 + S_2^2 + S_3^2}}{S_0}. \tag{2.7}$$

The value $P = 1$ corresponds to completely polarized light, $P = 0$ corresponds to unpolarized light, and $0 < P < 1$ corresponds to partially polarized light.

A change in polarization state, from one Stokes vector to another, due to interaction with an optical element is expressed through the matrix equation $\mathbf{S}_{out} = \mathbf{M}\mathbf{S}_{inc}$, where $\mathbf{M}$ is a 4x4 matrix called the Mueller matrix (MM) of the system. Written out in terms of the elements, this becomes

$$\begin{pmatrix} S_0 \\ S_1 \\ S_2 \\ S_3 \end{pmatrix}_{out} = \begin{pmatrix} M_{11} & M_{12} & M_{13} & M_{14} \\ M_{21} & M_{22} & M_{23} & M_{24} \\ M_{31} & M_{32} & M_{33} & M_{34} \\ M_{41} & M_{42} & M_{43} & M_{44} \end{pmatrix} \begin{pmatrix} S_0 \\ S_1 \\ S_2 \\ S_3 \end{pmatrix}_{inc}, \tag{2.8}$$

where the elements are real numbers that may take values $M_{ij} \in [-1, 1]$. The MM describes the optical element, and contains all the information about what happens to the polarization state during the interaction. The polarization state may be changed by changing the orthogonal field amplitudes unequally (diattenuation), changing the phase (retardance), changing the direction of the orthogonal field components (rotation), or transferring energy from polarized states to unpolarized states (depolarization). Any system's MM may be deconstructed into a succession of optical components, each described by its own MM, i.e. [2]

$$\mathbf{M} = \mathbf{M}_N \mathbf{M}_{N-1} ... \mathbf{M}_1, \tag{2.9}$$

where light propagates from 1 to N.

If the optical system is non-depolarizing, the MM may be fully described by a Jones matrix. For such a system described by the Jones matrix $\mathbf{J}$, the corresponding Mueller matrix is given by [2]

$$\mathbf{M} = \mathbf{A}(\mathbf{J} \otimes \mathbf{J}^*)\mathbf{A}^{-1} \tag{2.10}$$

where $\otimes$ is the Kronecker product and

$$\mathbf{A} = \begin{pmatrix} 1 & 0 & 0 & 1 \\ 1 & 0 & 0 & -1 \\ 0 & 1 & 1 & 0 \\ 0 & i & -i & 0 \end{pmatrix}. \tag{2.11}$$

In the case of reflection from a non-depolarizing sample, in a coordinate system defined by the beam's plane of incidence (POI) where the electric field orthogonal components are directed either parallel to POI (p-polarization) or perpendicular to the POI (s-polarization), the general reflection Jones matrix is

$$\mathbf{r} = \begin{pmatrix} r_{pp} & r_{ps} \\ r_{sp} & r_{ss} \end{pmatrix}, \tag{2.12}$$

see figure 2.1. The matrix elements in equation (2.12) are complex reflection coefficients. The convention of subscript notation is here used such that $r_{\alpha\beta}$ indicates the portion of the initially β-polarized wave that is converted to α-polarization after reflection. The off-diagonal elements therefore describe conversion between the two polarization modes. Conversion equations for the equivalent MM [32], found by inserting the reflection Jones matrix (2.12) into equation (2.10), are listed below

$$M_{11} = \frac{1}{2}(|r_{pp}|^2 + |r_{ps}|^2 + |r_{sp}|^2 + |r_{ss}|^2) \tag{2.13a}$$

$$M_{12} = \frac{1}{2}(|r_{pp}|^2 - |r_{ps}|^2 + |r_{sp}|^2 - |r_{ss}|^2) \tag{2.13b}$$

$$M_{13} = \mathrm{Re}[r_{pp}r_{ps}^* + r_{sp}r_{ss}^*] \tag{2.13c}$$

$$M_{14} = \mathrm{Im}[r_{pp}r_{ps}^* + r_{sp}r_{ss}^*] \tag{2.13d}$$

$$M_{21} = \frac{1}{2}(|r_{pp}|^2 + |r_{ps}|^2 - |r_{sp}|^2 - |r_{ss}|^2) \tag{2.13e}$$

$$M_{22} = \frac{1}{2}(|r_{pp}|^2 - |r_{ps}|^2 - |r_{sp}|^2 + |r_{ss}|^2) \tag{2.13f}$$

$$M_{23} = \mathrm{Re}[r_{pp}r_{ps}^* - r_{sp}r_{ss}^*] \tag{2.13g}$$

$$M_{24} = \mathrm{Im}[r_{pp}r_{ps}^* - r_{sp}r_{ss}^*] \tag{2.13h}$$

$$M_{31} = \mathrm{Re}[r_{pp}r_{sp}^* + r_{ps}r_{ss}^*] \tag{2.13i}$$

$$M_{32} = \mathrm{Re}[r_{pp}r_{sp}^* - r_{ps}r_{ss}^*] \tag{2.13j}$$

$$M_{33} = \mathrm{Re}[r_{pp}r_{ss}^* + r_{ps}r_{sp}^*] \tag{2.13k}$$

$$M_{34} = \mathrm{Im}[r_{pp}r_{ss}^* - r_{ps}r_{sp}^*] \tag{2.13l}$$

$$M_{41} = -\mathrm{Im}[r_{pp}r_{ps}^* + r_{sp}r_{ss}^*] \tag{2.13m}$$

$$M_{42} = -\mathrm{Im}[r_{pp}r_{ps}^* - r_{sp}r_{ss}^*] \tag{2.13n}$$

$$M_{43} = -\mathrm{Im}[r_{pp}r_{ss}^* + r_{ps}r_{sp}^*] \tag{2.13o}$$

$$M_{44} = \mathrm{Re}[r_{pp}r_{ss}^* - r_{ps}r_{sp}^*]. \tag{2.13p}$$

$$\tag{2.13q}$$

Note that there is a clear indication of polarization coupling induced by the sample if the off-diagonal block elements are non-zero.

There are many necessary conditions that must be met for a MM to be physically realizable [2] [51]. Here, however, the subject will only be briefly discussed. The question is which conditions should be imposed on the elements of $\mathbf{M}$ in order for it to correspond to a real physical system. Consider the optical system in figure 2.1. The emerging light, i.e. the resulting Stokes vector $\mathbf{S}_{out}$ after the incident light $\mathbf{S}_{inc}$ is operated on by $\mathbf{M}$, cannot have a degree of polarization larger than one and its total intensity must be positive. In

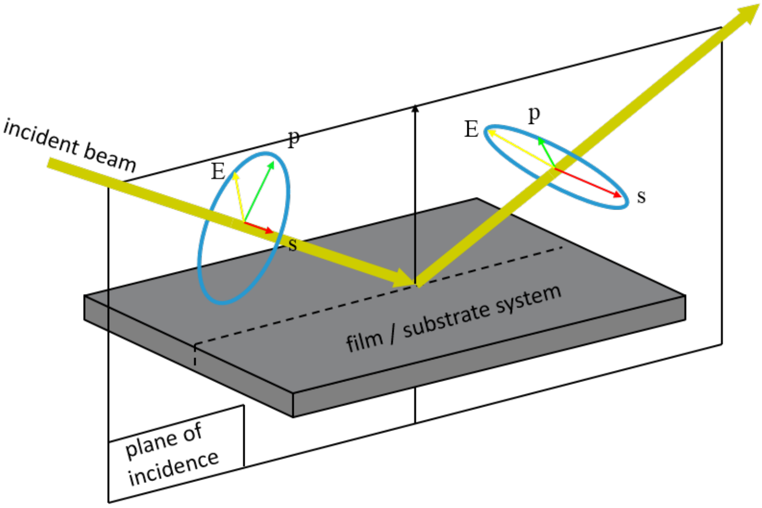

Figure 2.1: Light reflected at the interface between two media. Direction of electric field is defined from the beam's plane of incidence as p-polarization and s-polarization. Source [28].

other words, it must hold that $S_0^2 \geq S_1^2 + S_2^2 + S_3^2$ and $S_0 \geq 0$. What are the conditions on a given MM that will ensure that the output light is partially polarized for any polarization of the input light, or equivalently, when will the degree of polarization P of the output Stokes vector satisfy $P \leq 1$ for any physical input Stokes vector? This is a non-trivial matter and many constraints have been derived [51] [50]. The constraints may even be used for calibration of polarimetric instruments, estimation of experimental errors, and testing computational procedures.

2.3 Ellipsometry

Ellipsometry is an experimental technique for investigating optical properties of thin films and surfaces. It is a form of polarimetry, which is to measure and interpret the polarization state of light. The basic principle of ellipsometry is to measure the change in phase and amplitude of two orthogonal electric field components after reflection or transmission at the sample of interest, see figure 2.1. However, for most samples, an analytic inversion of the ellipsometric equations (discussed in the next section) is not possible and thus the unknown parameters cannot be obtained directly. Instead, a model can be created to calculate a response which is compared to the experimental response. Using regression analysis, fit parameters of the model are adjusted to find a minimum error function between the model data and experimental data. If the results of the assumed model are not fully in agreement with the experimental data, one may go back and redefine its properties e.g. by adding a roughness layer, anisotropy or graded optical properties. This is repeated until a satisfactory fit is found. The quality of the model can be quantified by a mean-square error or another error function. Figure 2.2 presents an overview of this process [18].

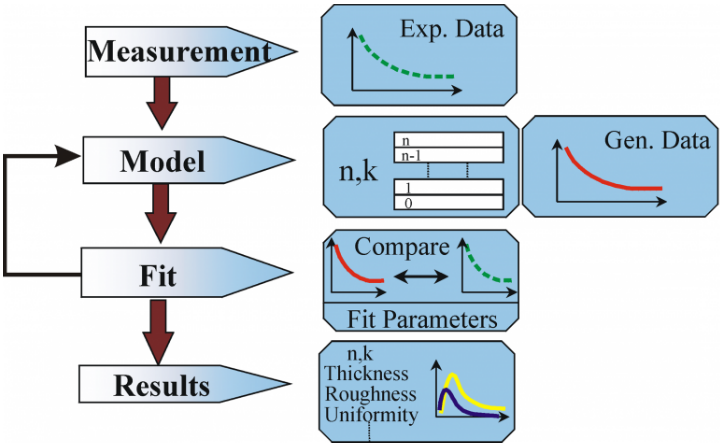

Figure 2.2: Overview of the fit procedure in ellipsometric data analysis. Source [18]

Thus, ellipsometry is an indirect method of retrieving optical properties from a sample, such as its dielectric function or refractive index, thin film thickness, surface roughness and layer composition.

2.3.1 Various forms of ellipsometry

There are mainly three types of ellipsometry; standard, generalized and Mueller-matrix ellipsometry. While the methods are here explained in terms of reflection off a sample, the principle and derivation are similar for transmission ellipsometry [78].

Standard ellipsometry

In standard ellipsometry, a single measurement of the sample-induced change in polarization is performed per wavelength, while assuming no coupling between p- and s-polarization. The reflection Jones matrix, equation (2.12), is therefore diagonal, the sample reflection properties entirely given by r_{ss} and r_{pp}. For light reflected at the interface between two isotropic media 0 and 1 as in figure 2.3, the complex reflection coefficients are the Fresnel equations [4]

$$r_{pp} = \frac{N_1 \cos\theta_0 - N_0 \cos\theta_1}{N_1 \cos\theta_0 + N_0 \cos\theta_1} \tag{2.14a}$$

$$r_{ss} = \frac{N_0 \cos\theta_0 - N_1 \cos\theta_1}{N_0 \cos\theta_0 + N_1 \cos\theta_1} \tag{2.14b}$$

with $N_{0,1}$ being the complex indices of refraction of the two media, θ_0 the polar angles of the incident and reflected beams (which are equal as per the law of reflection), and θ_1 is the refracted angle of the transmitted wave (obeying Snell's law) [31]. The basic quantity measured with an ellipsometer is the ratio

$$\rho = \chi_r / \chi_i, \tag{2.15}$$

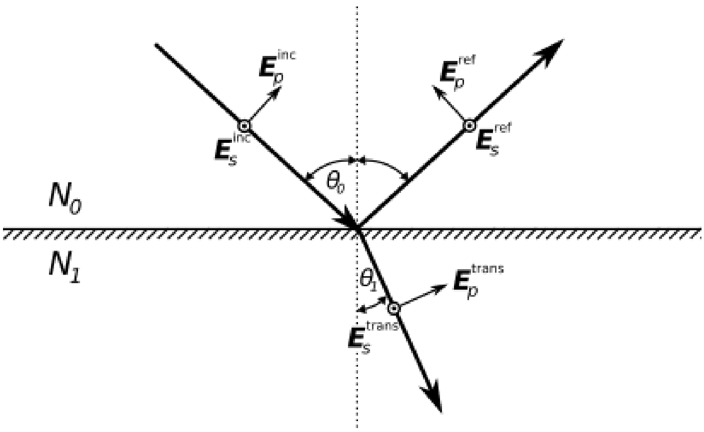

Figure 2.3: Light propagating in a medium with refractive index N_0 is partially reflected and transmitted when encountering a material with different index N_1. The transmitted wave is refracted at an angle θ_1, different from incident angle θ_0, unlike the reflected angle. The polarization state of each wave is defined by the amount of electric field which is p-polarized (parallel to page) and s-polarized (out of page), i.e. in-plane and perpendicular to the plane of incidence, respectively.

where χ_r and χ_i are the complex-number representation of the polarization states of the reflected and incident beams, respectively. Each polarization state is described by the ratio of complex-valued electric fields in the orthogonal p- and s-directions $\chi = E_p/E_s$. As the complex reflection coefficients are defined by the complex reflected and incident electric fields, $r_{pp} = E_{pr}/E_{pi}$ and $r_{ss} = E_{sr}/E_{si}$, we can rewrite equation (2.15) to be

$$\rho = \frac{r_{pp}}{r_{ss}} = \tan\Psi e^{i\Delta}. \tag{2.16}$$

The so-called ellipsometric angles Ψ and Δ are the experimentally determined parameters in standard ellipsometry. The angle Ψ describes the relative change in amplitude, while Δ describes the phase shift.

Generalized ellipsometry

In the case of an anisotropic sample one must generally include polarization coupling, i.e. the off-diagonal reflection Jones matrix elements r_{sp} and r_{ps} will be non-zero. Because of this, generalized ellipsometry requires at least three values of ρ measured at different polarization states χ_i which results in three pairs of (Ψ, Δ). The three complex-valued generalized ellipsometer parameters are defined as

$$\rho_{pp} = \frac{r_{pp}}{r_{ss}} = \tan\Psi_{pp} e^{i\Delta_{pp}} \tag{2.17a}$$

$$\rho_{ps} = \frac{r_{ps}}{r_{pp}} = \tan\Psi_{ps} e^{i\Delta_{ps}} \tag{2.17b}$$

$$\rho_{sp} = \frac{r_{sp}}{r_{ss}} = \tan\Psi_{sp} e^{i\Delta_{sp}}. \tag{2.17c}$$

If assuming a sharp interface between the two media, as in figure 2.3, one may combine equation (2.16) with equations (2.14) and Snell's law while applying $N^2 = \epsilon$ to derive a relation connecting the dielectric functions of the two media,

$$\langle\epsilon\rangle_{pp} = \sin^2\theta_0 \left[\epsilon_0 + \frac{(1-\rho_{pp})^2}{(1+\rho_{pp})^2}\tan^2\theta_0\right], \tag{2.18}$$

known as the *generalized pseudo-dielectric function* [68]. If surface layers can be neglected then $\langle\epsilon\rangle_{pp} = \epsilon_1$. Note that ϵ_0 is the dielectric function of the upper (ambient) media, not the vacuum permittivity.

Mueller-matrix ellipsometry

So far we have assumed no depolarization in the sample. When depolarization occurs, the Jones formalism is no longer valid and one should use the Mueller-matrix formalism in describing how an electromagnetic wave interacts with the elements within an ellipsometer (including the sample). Depolarization may be caused by effects such as thickness non-uniformity, non-coherent reflection and backside reflections from a transparent substrate. Furthermore, information such as s- and p-reflectance, and the isotropic and anisotropic ellipsometry parameters may be extracted from the Mueller matrix. In transmission mode, the MM may be useful to observe effects of s- and p-transmittance, optical rotation and circular dichroism[2].

The reflection MM of a non-depolarizing sample is readily available from equation (2.13). An isotropic sample is fully described by $\rho = \tan\Psi e^{i\Delta} = r_{pp}/r_{ss}$ as there is no cross-polarization, $r_{sp} = r_{ps} = 0$. It is then fairly straight forward to show that the MM in equation (2.13) becomes block-diagonal as it reduces to

$$\mathbf{M} = \frac{|r_{pp}|^2 + |r_{ss}|^2}{2}\begin{pmatrix} 1 & -N & 0 & 0 \\ -N & 1 & 0 & 0 \\ 0 & 0 & C & S \\ 0 & 0 & -S & C \end{pmatrix} \tag{2.19}$$

where N, C and S are introduced as

$$N = \cos 2\Psi \tag{2.20a}$$

$$C = \sin 2\Psi \cos\Delta \tag{2.20b}$$

$$S = \sin 2\Psi \sin\Delta. \tag{2.20c}$$

If the sample in addition is non-depolarizing, these parameters are related as

$$N^2 + C^2 + S^2 = 1. \tag{2.21}$$

Furthermore, the complex reflectance ratio can be expressed as [2]

$$\rho = \frac{C + iS}{1 + N}. \tag{2.22}$$

---

[2] Dichroism is either when light splits up into distinct beams of different wavelengths, or when light rays experience a different absorption coefficient (diattenuation) depending on its polarization state. Circular dichroism is dichroism involving circularly polarized light, i.e. the differential absorption of left- and right-handed light.

In the Mueller matrix approach, an isotropic sample is thus described by three parameters N, C and S, which reduces to two independent parameters if the sample is non-depolarizing.

Because the MM fully describes the polarization change due to a sample, it has been proved that the additional (in principle redundant) information provided greatly reduces the correlations observed between measured parameters compared to using standard spectroscopic ellipsometry. Examples of benefits gained by Mueller matrix formalism are found when characterizing gratings and anisotropic samples [56].

2.4 Interaction between matter and light

The interaction between metals and EM waves can be firmly understood by classical electrodynamics, and even metallic nanostructures of a few nanometers in size may be described in the classical sense without resorting to quantum mechanics [54]. From everyday experience we are well aware of the highly reflective and non-transmittive nature of metals for frequencies up to the visible spectrum. For the lower-frequency regime of microwave and far-infrared (IR) radiation one can in most cases assume the approximation that the metal is a perfect conductor to be valid, due to only a negligible part of the incident radiation actually penetrating into the metal. In the near-IR and visible regime the field penetration is more prominent and leads to increased dissipation. At ultraviolet (UV) frequencies metals become dielectric in character and allow for electromagnetic propagation. The attenuation of transmission will however depend on the electronic band structure of the individual metal. Alkali metals exhibit an ultraviolet transparency, while noble metals such as gold and silver experience strong absorption in this regime due to transitions between electronic bands.

In describing these interactions we first begin with Maxwell's equations (ME) of macroscopic electromagnetism in time domain [31],

$$\nabla \cdot \mathbf{D} = \rho_{ext} \tag{2.23a}$$

$$\nabla \cdot \mathbf{B} = 0 \tag{2.23b}$$

$$\nabla \times \mathbf{E} = -\frac{\partial \mathbf{B}}{\partial t} \tag{2.23c}$$

$$\nabla \times \mathbf{H} = \frac{\partial \mathbf{D}}{\partial t} + \mathbf{J}_{ext}, \tag{2.23d}$$

which links the four macroscopic fields, the dielectric displacement $\mathbf{D}$, the electric field $\mathbf{E}$, the magnetic field $\mathbf{H}$, and the magnetic induction $\mathbf{B}$, with the external charge and current densities ρ_{ext} and $\mathbf{J}_{ext}$. Furthermore, for linear media, the electric displacement field $\mathbf{D}$ is related to polarization $\mathbf{P}$, which describes the dipole moment per unit volume in the material, as [2]

$$\mathbf{D} = \epsilon_0 \mathbf{E} + \mathbf{P} \tag{2.24}$$

with the constitutive relation in frequency domain

$$\mathbf{D} = \epsilon_0 \epsilon \mathbf{E}. \tag{2.25}$$

Here, ϵ_0 is the permittivity of vacuum while ϵ is the relative permittivity of the medium, which is an intrinsic property of the given material describing the frequency-dependent relation between an applied electric field and the induced displacement field. It is also known as the dielectric function, as it will be called in this thesis. The dielectric function is in general complex for metals and other absorbing materials,

$$\epsilon = \epsilon_r + i\epsilon_i \tag{2.26}$$

and its relation to the complex refractive index is $N = \sqrt{\epsilon}$.

2.4.1 The dielectric function of the free electron gas

The optical response of metals can, over a wide frequency range, be explained by a free electron model. That is, a gas of electrons moving against a static background of positive ions. The equation of motion for an electron in the plasma sea under the effect of an external electric field $\mathbf{E}$ can be written as

$$m\ddot{\mathbf{x}} + m\gamma\dot{\mathbf{x}} = -e\mathbf{E} \tag{2.27}$$

with m being the effective optical mass of the electron and e the electron charge. The electron will oscillate in response to the applied field and its motion is damped through collisions described by the characteristic collision frequency γ. Assuming the driving field has a harmonic time dependence, $\mathbf{E}(t) = \mathbf{E}_0 e^{-i\omega t}$, equation (2.27) has a solution describing the electron oscillating as $\mathbf{x}(t) = \mathbf{x}_0 e^{-i\omega t}$. The complex amplitude $\mathbf{x}_0$ includes any phase shifts between the driving field and response, and is given by [54]

$$\mathbf{x}(\omega) = \frac{e}{m(\omega^2 + i\gamma\omega)}\mathbf{E}(\omega), \tag{2.28}$$

where a Fourier transform has been performed. This displacement from its equilibrium due to the applied electric field results in a polarization $\mathbf{P} = -ne\mathbf{x}$, where n is the electron number density. Inserting this into equation (2.28) gives us

$$\mathbf{P}(\omega) = -\frac{ne^2}{m(\omega^2 + i\gamma\omega)}\mathbf{E}(\omega). \tag{2.29}$$

From the relation (2.24) we see that

$$\mathbf{D}(\omega) = \epsilon_0(1 - \frac{\omega_p^2}{\omega^2 + i\gamma\omega})\mathbf{E}(\omega) \tag{2.30}$$

where $\omega_p^2 = ne^2/m\epsilon_0$ is the frequency of the collective oscillation of the valence electrons in the metal called the *plasma frequency*, defined as the frequency where the real part of ϵ is zero [20]. Finally, from the constitutive relation (2.25) we arrive at the dielectric function

$$\epsilon(\omega) = 1 - \frac{\omega_p^2}{\omega^2 + i\gamma\omega}. \tag{2.31}$$

The free electron gas is also known as the Drude model, and thus its dielectric function (2.31) is often called the *Drude response* of such a metal.

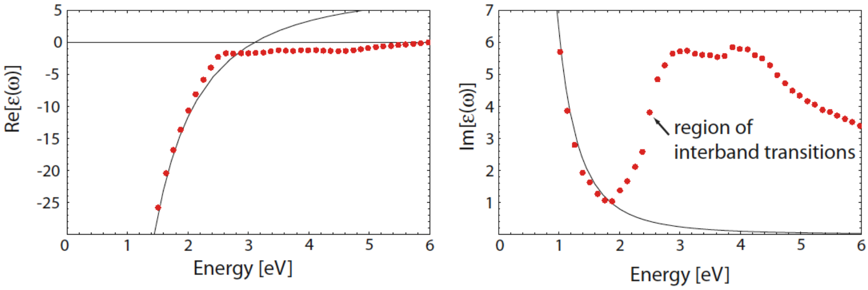

Figure 2.4: The dielectric function $\epsilon(\omega)$ of the free-electron model (solid line) is plotted against experimental values for gold (dots) found in [43]. Validity of the Drude model breaks down for higher energies due to interband transitions. Figure taken from [54].

For noble metals this approach is limited to frequencies below the visual range where interband transitions occur. For such metals an extension is needed in the region $\omega > \omega_p$, where free s-electrons dominates the response while the filled d-band near the Fermi surface causes a highly polarized environment. This residual polarization caused by the positive ion background can be described by adding a term $\mathbf{P}_\infty = \epsilon_0(\epsilon_\infty - 1)\mathbf{E}$ to equation (2.24) so that $\mathbf{P}$ in equation (2.29) now represents polarization due to free-electron displacement [54]. This effect is described by ϵ_∞ and we can rewrite the dielectric function to be

$$\epsilon(\omega) = \epsilon_\infty - \frac{\omega_p^2}{\omega^2 + i\gamma\omega}. \tag{2.32}$$

Figure 2.4 illustrates the validity of the free-electron model in the case of gold. Clearly, the model breaks down at visible frequencies and higher as ϵ_2 increases due to interband transitions.

Lorentz oscillators

A method of overcoming these problems at higher frequencies is to add an oscillator term to the equation of motion (2.27)

$$m\ddot{\mathbf{x}} + m\gamma\dot{\mathbf{x}} + m\omega_0^2\mathbf{x} = -e\mathbf{E} \tag{2.33}$$

so that interband transitions are represented by the classical picture of a bound electron with resonance frequency ω_0. The dielectric function can be found by the same procedure as before, solving the equation of motion (2.33) and combining equations (2.29) and (2.25), resulting in

$$\epsilon(\omega) = 1 - \frac{\omega_p^2}{\omega^2 - \omega_0^2 + i\omega\gamma}. \tag{2.34}$$

The plot in figure 2.5 shows the typical behaviour of a Lorentz oscillator.

There are shortcomings with this simple model as it neglects several types of forces in the derivation [2]; one can more accurately describe the material as a sum of several

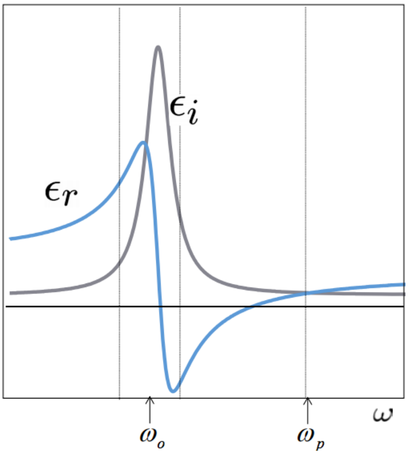

Figure 2.5: Typical behaviour of a Lorentz oscillator. Dispersion of light interacting with the material occurs when real part ϵ_r is non-constant. Absorption occurs when the imaginary part is non-zero, $\epsilon_i \neq 0$. A resonance is centered around ω_0 with half-bandwidth γ. Figure taken from [36].

Lorentz oscillators, generalizing equation (2.34) as

$$\epsilon(\omega) = \epsilon_\infty - \omega_p^2 \sum_j \frac{f_j}{\omega^2 - \omega_j^2 + i\omega\gamma_j} \tag{2.35}$$

where f_j is the oscillator strength with $\sum f_j = 1$. Again, it is convenient to summarize all higher energy frequencies into the real-valued parameter ϵ_∞, describing the relative permittivity at infinite energy, often equating to unity. The Lorentz model is valid only for energies (significantly) lower than the band gap energy.

2.4.2 Dielectric function of solids over a wide frequency range

The optical response function has a few general properties that are caused by causality, i.e. its reaction is only dependent on past events and not future events. This leads to the Kramers Kronig relations [2]. The Kramer Kronig relations are bidirectional mathematical relations that connects real and imaginary parts of complex functions that are analytic in the upper half-plane, thus applicable to response functions of linear systems where the relationship between input and output is causal [1]. A consequence of Kramers Kronig relations is that if one of the functions (real part ϵ_1 or imaginary ϵ_2) are determined for all frequencies, then the other part can be calculated for all frequencies as well.

Consider equation (2.24), which solved for $\mathbf{P}$ is

$$\mathbf{P} = (\epsilon - 1)\epsilon_0\mathbf{E}. \tag{2.36}$$

It is clear that the term $(\epsilon - 1)$ represents the optical response as it relates the electric field $\mathbf{E}$ to the polarization $\mathbf{P}$, i.e. the term gives the relation between the *cause* $\mathbf{E}$ and *effect* $\mathbf{P}$. With basis in equation (2.24) and taking into account causality, that $\mathbf{E}$ must precede a

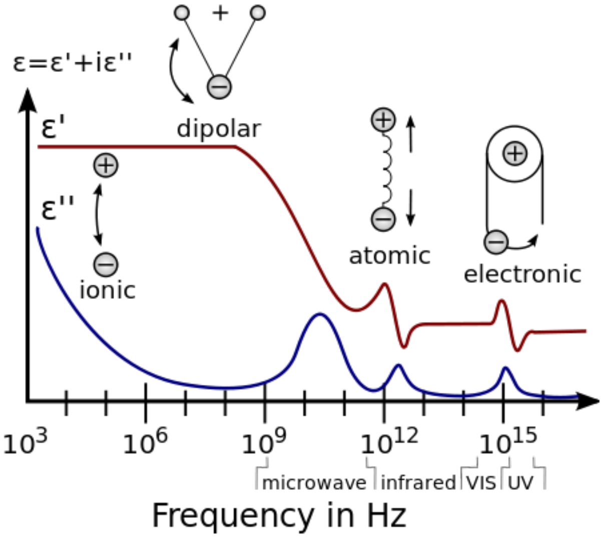

Figure 2.6: Frequency variation of the dielectric function, showing various dielectric mechanisms: ionic and dipolar relaxation, and resonances of vibrational and electric oscillators. Figure from [57].

response $\mathbf{P}$ implying that $\mathbf{P}$ should vanish for $t < 0$, as well as Cauchy's residue theorem for complex functions, it can be shown that the Kramer Kronig integrals are [20] [2]

$$\epsilon_1 - 1 = \frac{2}{\pi}\mathscr{P}\int_0^\infty \frac{\epsilon_2(\omega')\omega'}{\omega'^2 - \omega^2}d\omega' \tag{2.37a}$$

$$\epsilon_2 = -\frac{2\omega}{\pi}\mathscr{P}\int_0^\infty \frac{\epsilon_1(\omega') - 1}{\omega'^2 - \omega^2}d\omega' \tag{2.37b}$$

where $\mathscr{P}$ denotes the principal part of the integral.

Both dispersion (described by ϵ_1) and absorption (described by ϵ_2) originate from the same underlying process, excitation of dipoles in the material. If the dipoles can follow the field instantaneously in a frequency region, there will be no absorption ($\epsilon_2 = 0$). For the same reason there will be no dispersion, as ϵ_1 is constant. In the frequency region around a relaxation (see figure 2.5), the dipoles will still try to match the field but cannot follow it completely. The dipoles will not move as much as at lower frequencies and thus the polarization becomes smaller (ϵ_1 decreases). At the same time absorption occurs ($\epsilon_2 \neq 0$) because energy is tapped from the electromagnetic field into the dipoles and then subsequently into the material. No dispersion can occur if there is no absorption and vice versa. This is the physical interpretation of the Kramer-Kronig relations, that absorption and dispersion are coupled properties of the same phenomenon [2].

Figure 2.6 shows a dielectric function over a wide frequency range. One quickly observes that at each relaxation frequency of ϵ_1 there is an associative peak in absorption ϵ_2. Starting at $\omega = 0$, the dielectric function is composed of contributions from each polarization mechanism (permanent dipoles, vibrational oscillators and electronic oscillators), with the lowest-frequency mechanism contributing the most. As the frequency increases, the permanent dipoles cannot respond and the real part ϵ_1 drops to a value at a frequency low compared to the characteristic vibrational frequency. As the frequency increases through the vibrational region, ϵ_1 oscillates and settles down at a low-frequency limit for electronic modes. For frequencies far above all absorption bands ϵ_1 approaches the free-space value 1; the frequencies are so high that none of the polarization mechanisms can respond, see equation (2.37) [13].

2.4.3 Joule heating

Energy of the light incident on a material can be dissipated into heat. Resistive (or ohmic) heating is a process by which an electric current passing through a conductor produces heat. In microscopic terms, resistive heating is caused by interactions between the moving particles of the electron plasma and the atomic ions of the material. The electrons are accelerated by an electric field causing them to collide with the ions, resulting in random scattered motion. These thermal fluctuations increases the temperature of the system. Resistive heating defined as power input per unit volume due to electric current is [40]

$$\frac{dP_{\text{resistive}}}{dV} = \mathbf{J} \cdot \mathbf{E}. \tag{2.38}$$

Here, $\mathbf{J}$ is the current density defined from the constitutive relation $\mathbf{J} = \sigma\mathbf{E} + \mathbf{J}_{ext}$, where σ is the conductivity of the electron plasma. Solving equation (2.38) with respect to $P_{\text{resistive}}$ we get

$$P_{\text{resistive}} = \int_V \mathbf{J} \cdot \mathbf{E} dV, \tag{2.39}$$

which result in heat dissipation in the material of volume V.

2.4.4 Effective medium approximation

This section will give a rough introduction to effective medium theory, and specifically the Bruggeman effective medium model. Effective medium approximations (EMA) refer to analytical modeling that describe the macroscopic properties of composite materials. A heterogeneous material with inhomogeneities of sizes sufficiently smaller than the wavelength of light will appear as a homogeneous material, i.e. there will be no scattering from the material and its optical properties may be summarized by an effective dielectric function ϵ_{eff} [2]. EMAs are often used to model nanostructured surfaces, metamaterials, surface roughness, or mixed materials. They are convenient when used together with ellipsometric measurements to characterize nanostructures of a sample.

An effective medium model assumes that the macroscopic optical response of a microstructure of heterogeneous multi-phase media may be estimated by a random unit cell (an effective medium) that should not be detectable in an experiment using EM radiation confined to a specified wavelength range. Put differently, the extinction of the random unit cell should be the same as if it were replaced with a material with the effective dielectric function. The Bruggeman effective medium model assumes the material has an aggregate structure as shown in figure 2.7, which demands a random unit cell which guarantees the

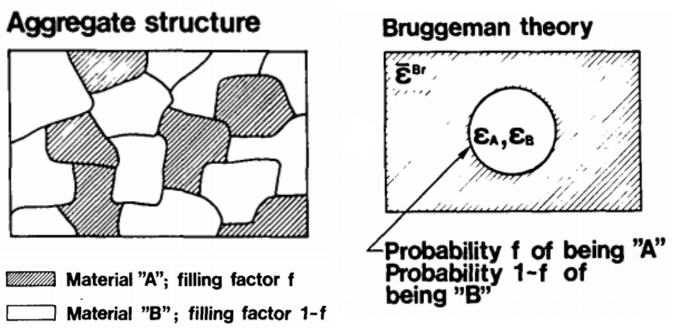

Figure 2.7: (left) An aggregate structure, where two materials are mixed on a random basis, (right) the corresponding random unit cell used to derive the effective dielectric function for the Bruggeman theory. Figure from [67].

structural equivalence of the two constituents. The cell is therefore a sphere whose dielectric function is ϵ_A with probability f_A, and ϵ_B with probability f_B. The Bruggeman effective medium expression is known as

$$0 = f_A \frac{\epsilon_A - \epsilon_{\text{eff}}}{\epsilon_A + 2\epsilon_{\text{eff}}} + f_B \frac{\epsilon_B - \epsilon_{\text{eff}}}{\epsilon_B + 2\epsilon_{\text{eff}}} \tag{2.40}$$

where f_A is the volume fraction of material A and $f_B = 1 - f_A$ is the volume fraction of material B [2].

2.5 Plasmonics

The field of plasmonics explores how electromagnetic fields may be confined and/or enhanced over sub-wavelength dimensions. It is based on the interaction between light and the conduction electrons at a metallic interface or metallic nanoparticles, resulting in an enhanced electromagnetic field over dimensions smaller than the wavelength of light. There are two types of surface plasmons. One is a dispersive electromagnetic wave coupled to the electron plasma of a conducting material propagating along the interface between the conductor and a dielectric. This is called a surface plasmon polariton resonance (SPPR), or just SPP or SPR. The other type is a non-propagating excitation of the electron plasma of metallic nanostructures coupled to an incident electromagnetic field called a localized surface plasmon resonance (LSPR). This thesis will focus on describing the latter.

2.5.1 Localized surface plasmons

LSPRs occur naturally in the scattering of an oscillating electromagnetic field from a small, sub-wavelength conductive nanoparticle. The surface curvature of the particle acts as an effective restoring force on the driven electron-plasma so that a resonance arises, which leads to field amplifications both inside and in the near-field zone outside the particle [54]. The spectral location of the LSPR is characteristic for the size, the shape, the material and the surrounding medium of the nanoparticle.

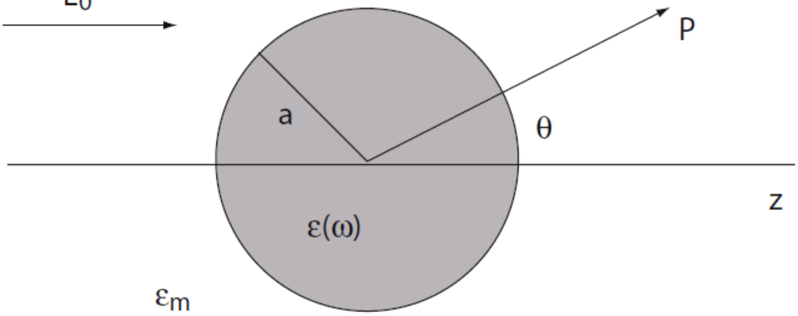

Figure 2.8: A metallic sphere with radius a and dielectric function $\epsilon(\omega)$ placed in an ambient medium with dielectric constant ϵ_m. The particle is subject to an external electrostatic field E_0. Figure taken from [54].

Normal modes

The interaction process between light and a sub-wavelength metal particle with diameter d may be examined by using the *quasi-static approximation*, assuming $d \ll \lambda$. The phase of the harmonically oscillating field is then considered to be practically constant over the particle volume, i.e. the particle is assumed to be surrounded by an electrostatic field. By ignoring spatial retardation effects over the particle the spatial field distribution can be calculated, while the harmonic time dependence may be added to the solution afterwards. This approximation has been shown to be reasonable for spherical and ellipsoidal particles with dimensions below 100 nm when illuminated by visible or near-IR light [54].

We will from here on concider the example of a homogeneous, isotropic sphere of radius a located at the origin in a uniform, static electric field $\mathbf{E} = E_0\hat{\mathbf{z}}$. The surrounding isotropic non-absorbing medium has dielectric constant ϵ_m while the dielectric response of the sphere is $\epsilon(\omega)$. See figure 2.8. The distribution of the electric field $\mathbf{E} = -\nabla\Phi$ can then be calculated from the solution of the Laplace equation $\nabla^2\Phi = 0$ [31]. Since the problem has azimuthal symmetry, the general solution is [40]

$$\Phi(r,\theta) = \sum_{l=0}^{\infty}[A_l r^l + B_l r^{-(l+1)}]P_l(\cos\theta), \tag{2.41}$$

with Legendre polynomials $P_l(\cos\theta)$ of order l, and θ being the angle between z-axis and the position vector $\mathbf{r}$. The potentials must be finite at the origin, the solution for the potentials inside and outside the sphere may therefore be written as

$$\Phi_{in}(r,\theta) = \sum_{l=0}^{\infty} A_l r^l P_l(\cos\theta) \tag{2.42a}$$

$$\Phi_{out}(r,\theta) = \sum_{l=0}^{\infty} [B_l r^l + C_l r^{-(l+1)}] P_l(\cos\theta). \tag{2.42b}$$

The coefficients A_l, B_l, C_l may be determined from the boundary conditions at $r \to \infty$ and $r = a$. On the former limit it is required that $\Phi_{out} \to -E_0 z = -E_0 r\cos\theta$ which requires $B_1 = -E_0$ and $B_l = 0$ for $l \neq 1$. The remaining coefficients are found from the latter limit on the particle surface, by equating tangential components of the electric field outside and inside the sphere at $r = a$, and similarly by equating the normal components of the displacement field. This leads to $A_l = C_l = 0$ for $l \neq 1$, and by calculating the remaining A_1 and C_1 the potentials end up as [40]

$$\Phi_{in} = -\frac{3\epsilon_m}{\epsilon + 2\epsilon_m} E_0 r\cos\theta \tag{2.43a}$$

$$\Phi_{out} = -E_0 r\cos\theta + \frac{\epsilon - \epsilon_m}{\epsilon + 2\epsilon_m} E_0 a^3 \frac{\cos\theta}{r^2}. \tag{2.43b}$$

The last equation (2.43b) may be interpreted physically as Φ_{out} describing the superposition of the applied field and that of a dipole located at the particle center. It is therefore interesting to rewrite Φ_{out} in terms of dipole moment $\mathbf{p}$ as

$$\Phi_{out} = -E_0 r\cos\theta + \frac{\mathbf{p}\cdot\mathbf{r}}{4\pi\epsilon_0\epsilon_m r^3} \tag{2.44a}$$

$$\mathbf{p} = 4\pi\epsilon_0\epsilon_m a^3 \frac{\epsilon - \epsilon_m}{\epsilon + 2\epsilon_m}\mathbf{E_0}. \tag{2.44b}$$

Thus, the applied field induces a dipole moment inside the sphere proportional to the electric field. The radiation of this dipole leads to *scattering* of the plane wave by the sphere, which can be represented as radiation by a point dipole as here. Introducing polarizability α, defined as $\mathbf{p} = \epsilon_0\epsilon_m\alpha\mathbf{E}_0$, results in [3]

$$\alpha = 4\pi a^3 \frac{\epsilon - \epsilon_m}{\epsilon + 2\epsilon_m}. \tag{2.45}$$

Polarizability describes a material's ability to form instantaneous dipoles, or in other words, the relative tendency of a charge distribution to have its charges displaced by an external electric field. We see from (2.45) that the polarizability is proportional to the particle radius cubed, and it is apparent that a resonant behaviour occurs when $|\epsilon + 2\epsilon_m|$ is at a minimum. In the case of a small or slowly varying Im$[\epsilon]$ this resonance condition simplifies to

$$\text{Re}[\epsilon(\omega)] = -2\epsilon_m. \tag{2.46}$$

---

[3] For a particle in air, i.e. $\epsilon_m = 1$, equation (2.45) is more famously known as the Clausius-Mossotti relation when the particle is a sphere.

This is known as the Frölich condition, and the associated mode is called the *dipole surface plasmon* of the metal nanoparticle [54].

From equation (2.46) it is evident that the resonance frequency depends strongly on the dielectric environment: for a Drude metal with a small Im$[\epsilon(\omega)]$ the resonance red-shifts as the dielectric constant of the surroundings ϵ_m increases. Metal nanoparticles are therefore a very promising mean of optical sensing of changes in refractive index.

A consequence of a resonantly enhanced polarizability is an accompanying enhancement in the metal nanoparticle's ability to scatter and absorb light. From a Mie theory approach for particles small compared with wavelength one can find the cross sections for scattering and absorption [13],

$$C_{sca} = \frac{k^4}{6\pi}|\alpha|^2 = \frac{8\pi}{3}k^3a^6\left|\frac{\epsilon-\epsilon_m}{\epsilon+2\epsilon_m}\right|^2 \tag{2.47a}$$

$$C_{abs} = k\mathrm{Im}[\alpha] = 4\pi k a^3\mathrm{Im}\left[\frac{\epsilon-\epsilon_m}{\epsilon+2\epsilon_m}\right] \tag{2.47b}$$

with $k = 2\pi/\lambda$. Equations (2.47) are valid for all spherical particles $a \ll \lambda$ with different material properties from its ambient, no metallic assumption is made in the derivation, and the equations are therefore also valid for dielectric scatterers. Due to the rapid scaling of $C_{sca} \propto a^6$ it is very difficult to pick out small objects from a background of large scatterers. Equations (2.47) also show that for metallic nanoparticles both absorption and scattering (and thus extinction) is resonant at the dipole particle plasmon resonance when the Frölich condition is met.

2.5.2 Particle size and shape effects

Two regimes can be considered when investigating how particle size affects the LSPR: larger particles where retardation effects are non-neglible, and very small metal particles with dimensions smaller than the mean free path of its oscillating electrons. The latter regime regards particles of radius $a < 10$ nm [54], as this thesis does not consider particles of such size we will focus our efforts on the former.

For particles with larger dimensions the quasi-static approximation is no longer valid as there will be significant phase-changes of the driving field over the particle volume. A rigorous electrodynamic Mie theory approach is needed to find the polarizability for such a spherical particle, the interested reader can find the equation and derivation in [33] [59]. For such particles there is found to be an energy shift of the plasmon resonance due to the retardation of the depolarization field[4] inside the particle [59]. Figure 2.9 shows the change in local field enhancement as particle size of silver spheres is increased. The dipole resonance red-shifts and is strongly broadened along with a drastic decrease in enhancement. The spectral shift of plasmon resonance to longer wavelengths suggests that interband transitions (described by an increase in ϵ_2) have less effect as the resonance moves away from the band gap energy [54]. As the particle size increases the dipole plasmon resonance is severely damped, mainly due to *radiation damping* [80]. Radiative

---

[4] In the case that the polarization of the dipoles is induced by an external field, the polarization field $\mathbf{P}$ opposes the applied field $\mathbf{E}$ and is sometimes called a depolarization field.

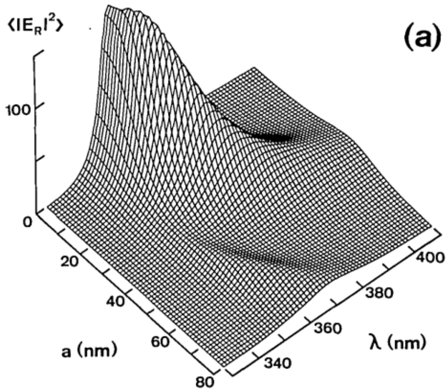

Figure 2.9: (a) Electric field enhancement on the surface of silver spheres of radius a. The radial surface field E_R is normalized by the incident field. Absolute maximum occurs at $a = 12.5$nm for $\lambda_{max} = 357$nm (electrostatic limit $a = 0$nm: $\lambda_{max} = 355$nm). LSPR enhancement decreases for larger particles, in addition it is shifted to longer wavelengths and broadened. The surface field is dominated by dipolar contribution. The smaller resonance for $a > 40$nm is due to quadrupole contribution. Figure taken from [59].

damping is the direct decay of a surface plasmon (the coherent electron oscillation on the metal surface due to coupling with the external EM wave) into photons [49].

Particle shape effects will be briefly investigated by studying an ellipsoid, being the most general smooth particle, in the electrostatics approximation. Consider an ellipsoid with semiaxes $a > b > c$ with a dipole moment induced by a uniform electrostatic field parallel to one of its principal axes. The dipole moment, and hence the polarizability of the ellipsoid, will vary depending on which of the three axes the applied field is parallel to. Then, for an ellipsoid with dielectric function ϵ set in an ambient medium ϵ_m, the polarizability is given by [13]

$$\alpha_i = \frac{4\pi abc}{3} \frac{\epsilon - \epsilon_m}{\epsilon_m + L_i(\epsilon - \epsilon_m)} \qquad i = 1, 2, 3 \tag{2.48}$$

when the electric field is directed along the ith axis of the ellipsoid corresponding to the parameters a, b and c, respectively. Here, L_i are the geometrical factors related to the shape of the particle, where $\sum_i L_i = 1$ and $L_1 \leq L_2 \leq L_3$. For a sphere we have $L_1 = L_2 = L_3 = 1/3$, and (2.48) reduces to equation (2.45).

The resonance of the surface plasmon polariton may be tuned by changing the size and shape of a metallic nanoparticle, as shown in figure 2.10. It is clear that changing the aspect ratio of the particle has greater impact on the resonance position than changing its diameter. The resonance intensity in 2.10b has a maximum for an aspect ratio between 0.3 and 0.4 [79] [7].

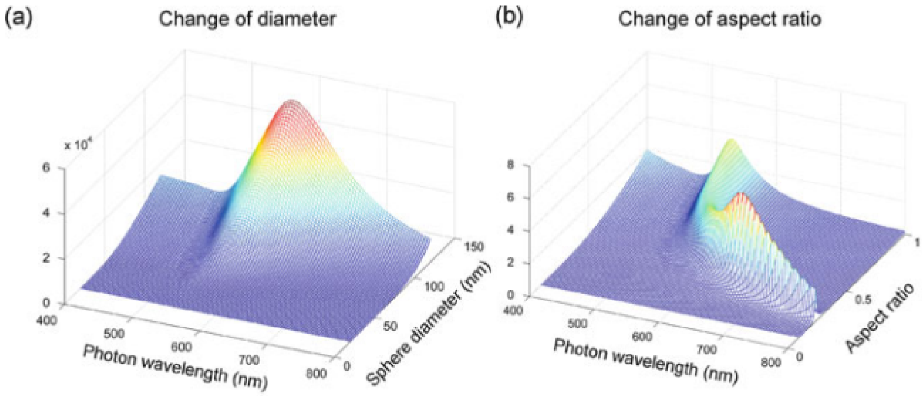

Figure 2.10: Scattering cross section plotted against changes in (a) the diameter and (b) the aspect ratio of a gold nanosphere in the spectrum around a surface plasmon polariton resonance. Figure from [79].

2.5.3 Coupling between LSPRs

Until now we have regarded the LSPR in a single metallic nanoparticle, and the shift in resonance frequency caused by changes in particle shape and size. One may expect additional shifts in frequency when several such particles are brought together, due to electromagnetic interaction between neighbouring localized modes.

The dipolar approximation may be assumed when the particle sizes are much smaller than the interparticle distance, $a \ll d$, so that the particles may be treated as point dipoles. For closely spaced particles, $d \ll \lambda$, the near-field interactions dominate with a distance dependence of d^{-3} (see equation (2.44)) and the particle ensemble may be described as an array of dipoles interacting with their near-field [54]. By considering the Coulomb forces associated with the polarization of particles in an array of interacting point dipole particles, one can intuitively see that interparticle coupling will lead to shifts in the LSPR spectral position when compared to an isolated particle. Figure 2.11 illustrates how the restoring force, acting on the oscillating electrons in each particle, is either increased or decreased by the charge distribution of their neighbouring particles. The particle's internal dipole moment induced by the applied external field affects its neighbouring particle's induced dipole moment. This leads to a blueshift of the plasmon resonance for transversal polarization of the exciting light, and a redshift for longitudinal polarization.

For larger particle seperations the external dipole fields become spherical in shape and the far-field dipolar coupling dominates with a distance dependence of d^{-1} [54]. This coupling via diffraction has been studied for two-dimensional arrays of gold nanoparticles with various lattice constants [5]. Figure 2.12 shows that far-field coupling influences the plasmon resonance both in terms of peak strength and spectral width. The spectral shift and broadening of the plasmon resonances are attributed to the periodicity of a square array. The dipolar fields of neighbouring particles are superimposed with their respective phase shifts, which depend on the interparticle distance [5].

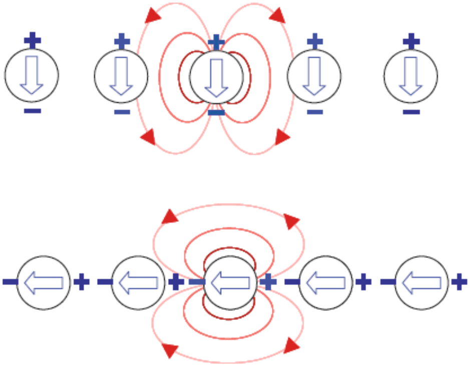

Figure 2.11: Near-field coupling between metallic nanoparticles when light incident from the side is s-polarized (top) and p-polarized (bottom). Thick arrows indicate each particle's internal dipole moment. Figure from [54].

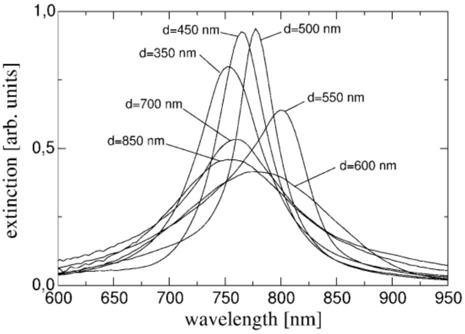

Figure 2.12: Extinction spectra for square two-dimensional gratings of circular gold nanoparticles (height 14 nm, diameter 150 nm) on an indium-tin-oxide coated glass substrate with grating constant d. Figure from [5].

2.6 Diffraction anomalies in periodic nanostructures

Periodic metallic nanostructures are known to show certain intensity anomalies. In 1902 Wood discovered anomalies in his data when studying the spectrum of an optical metallic diffraction grating, remarking that the anomalies were present only for p-polarized light, i.e. when the magnetic field is parallel to the grating grooves [81]. It was later discoverd by Fano that there could be distinguished two types of such anomalies [21]. The first type is an abrupt change in reflectivity appearing at sharply defined wavelengths at a given angle of incidence of the incoming light, known today as *Rayleigh anomalies* [58]. These are independent of the metal on which the grating was ruled on, and are furthermore found to also occur (albeit weakly) for incident light with the electric field polarized parallel to the grooves, i.e. s-polarization, if the grooves are sufficiently deep [55]. The second type is a diffuse anomaly, consisting generally of a minimum and a maximum of intensity, associated with the excitation of a SPP due to both the geometry and the optical properties of the metal grating [55] [21]. A thorough explanation and derivation of the latter type, known as *Wood anomaly*, can be found in [58]. Both anomalies are strongly dependent on the grating geometry, the presence of sharp edges in the profile of the grooves being a necessary condition for their existence [21]. This section will focus on explaining the Rayleigh anomalies.

It was first shown by Rayleigh that these anomalies occur at wavelengths where the diffracted light of a given order disappears at grazing angles along the grating surface [70] [71]. For regular periodic structures of nanoparticles on a transparent substrate, a diffracted beam will disappear as it attempts to cross the boundary between the ambient (usually air) and substrate media. The transition between air and substrate is prohibited due to different dispersion relations for light in both media. The diffraction mode is said to be cut off at a Rayleigh cutoff wavelength λ_R, resulting in a sudden change in reflection. There are two types of Rayleigh cutoff wavelengths for every mode; one for the disappearance of an ”air” diffraction mode, where the mode crosses the boundary from air to substrate; the other for the disappearance of a ”substrate” diffraction mode, crossing the boundary from substrate to air. When light with wavelength λ_R is incident on the array, one of the diffracted waves will travel exactly along the substrate surface and subsequently will interact with other nanoparticles. It is therefore interesting to note that if λ_R is close to the wavelength of an individual nanoparticle's LSPR, very sharp plasmon resonances may be obtained as energy from the incident light is transferred into localized plasmon modes in the narrow wavelength range near the Wood anomaly [52].

The remaining part of this section will derive an equation that can determine all Rayleigh anomalies, i.e. the condition for a scattered or transmitted wave vector along the surface of a diffraction grating.

Consider an array of scatterers where the position of each unit cell describing the periodicity is given by the lattice vector

$$\mathbf{x}^{\mathbf{l}} = l_1\mathbf{a}_1 + l_2\mathbf{a}_2 \tag{2.49}$$

where $\mathbf{a}_{1,2}$ are two noncollinear primitive translation vectors and $\mathbf{l} = (l_1, l_2)$ with $l_{1,2}$ being integers labeling the unit cells. The associated reciprocal lattice is given by

$$\mathbf{G}_{\parallel}^{\mathbf{m}} = m_1\mathbf{b}_1 + m_2\mathbf{b}_2 \tag{2.50a}$$

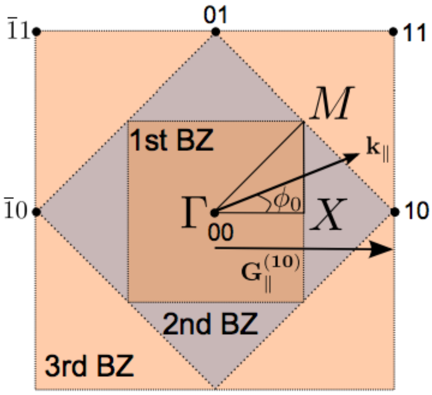

Figure 2.13: Schematic overview of the reciprocal lattice of a square array. Azimuthal angle of incident wave is defined as $\phi_0\angle(\mathbf{G}_{||}^{(10)}, \mathbf{k}_{||})$. The boundary of the first three Brillouin zones are indicated by dotted lines, accompanied by critical symmetry points. Figure taken from [15].

where $\mathbf{m} = (m_1, m_2)$ are integers, $\mathbf{b}_1$ and $\mathbf{b}_2$ denote the primitive translation vectors of the reciprocal lattice defined by $\mathbf{a}_i \cdot \mathbf{b}_j = 2\pi\delta_{ij}, i, j = 1, 2$ [5]. In terms of polar coordinates the reciprocal lattice vector becomes

$$\mathbf{G}_{||}^{\mathbf{m}} = G_{||}^{\mathbf{m}}\langle\cos\phi_{\mathbf{m}}, \sin\phi_{\mathbf{m}}, 0\rangle \tag{2.50b}$$

where $G_{||}^{\mathbf{m}}$ is the length of the reciprocal lattice vector, which for a rectangular lattice ($\mathbf{b}_1 \perp \mathbf{b}_2$) is

$$G_{||}^{\mathbf{m}} = 2\pi\sqrt{\frac{m_1^2}{a_1^2} + \frac{m_2^2}{a_2^2}}. \tag{2.50c}$$

Figure 2.13 shows a schematic diagram of the reciprocal array in the case of a square lattice, $a_1 = a_2 = a$. Azimuthal angle of the incident light is defined as the angle ϕ_0 between the vectors $\mathbf{k}_{||}$ and $\mathbf{G}_{||}^{(10)}$ as shown in the figure, where $\mathbf{k}_{||} = k\sin\theta_0\langle\cos\phi_0, \sin\phi_0, 0\rangle$ is the component of incident wave vector parallel to the substrate surface. Similarly, the angle $\phi_{\mathbf{m}}$ of reciprocal lattice point $\mathbf{m}$ is the angle between $\mathbf{G}_{||}^{(10)}$ and $\mathbf{G}_{||}^{\mathbf{m}}$.

Let us now define the diffraction wave vector into the air or substrate, parallel to the interface, as [53]

$$\mathbf{q}_{||}^{\mathbf{m}} = \mathbf{k}_{||} + \mathbf{G}_{||}^{\mathbf{m}}. \tag{2.51}$$

The dispersion of Rayleigh anomalies in a two-dimensional planar grating follows the relation $\mathbf{q}_{||}^{\mathbf{m}} = \mathbf{q}^{\mathbf{m}}$, which suggests that

$$\left|\mathbf{q}_{||}^{\mathbf{m}}\right|^2 = n_i^2 k^2 \tag{2.52}$$

---

[5] Kronecker delta, $\delta_{ij} = \begin{cases} 1, & \text{if } i = j, \\ 0, & \text{if } i \neq j. \end{cases}$

is the condition for a grazing diffracted wave, where n_i is the refractive index of either ambient or substrate, depending on which side of the interface the light is approaching from. By using equations (2.50)-(2.52) one may derive an equation determining all Rayleigh anomalies, resulting in [15]

$$k^2 - \frac{2\sin\theta_0 G_{\|}^{\mathbf{m}} \cos(\phi_m - \phi_0)}{n_i^2 - \sin^2\theta_0} k - \frac{(G_{\|}^{\mathbf{m}})^2}{n_i^2 - \sin^2\theta_0} = 0, \tag{2.53}$$

that is, solving equation (2.53) with respect to $k = 2\pi/\lambda_R$ for a given angle of incidence (θ_0, ϕ_0) tells us which wavelengths of incident light that will result in diffracted modes propagating exactly along the air/substrate interface.

It is known that for a wave in a periodic medium whose wave vector terminates on the boundary of a Brillouin zone (BZ), satisfy the condition of diffraction [48]. Therefore, for a square lattice, inserting $G_{\|}^{\bar{1}0}$, $G_{\|}^{\bar{1}\bar{1}}$, or $G_{\|}^{\bar{2}0}$ as $G_{\|}^{\mathbf{m}}$ in equation (2.53) results in the boundaries of the first, second or third Brillouin zones, respectively, when solved over $\phi_0 \in [0°, 45°]$ for a fixed polar angle of incidence θ_0 and refractive index n_i. The boundaries of the 1st and 2nd BZ of a two-dimensional square lattice are shown in figure 2.13.

2.6.1 Decay length of normal component

It is of interest to note the decay length of evanescent waves associated with the cut-off diffraction orders produced by periodic nanostructures, particularly the component normal to the substrate surface. For the square array, the normal component of the longitudinal wave vector of the first order, $k_z^{(1)} = [k^2 - (2\pi/a + k_{\|})^2]^{1/2}$, is imaginary, where k and $k_{\|}$ are the magnitudes of the total and transverse wave numbers of the incident light. The next order is $k_z^{(2)} = [k^2 - (2\pi/a - k_{\|})^2]^{1/2}$. The decay length δ of the evanescent field is defined as the distance for which the field amplitude has decayed by a factor e^{-1}, and is here given by [30]

$$\delta = \frac{1}{\mathrm{Im}[k_z^{(1)}]} = \left[\left(\frac{2\pi}{a} - k_{\|}\right)^2 - k^2\right]^{-1/2}. \tag{2.54}$$

For sub-wavelength sized structures we have $k \ll 2\pi/a$, so that equation (2.54) reduces to $\delta \approx a/(2\pi)$ [30].

2.7 Finite element method

The finite element method (FEM) is a numerical method for finding approximate solutions to boundary value problems for partial differential equations (PDEs). It is applicable to many physical problems, such as finding the electric potential in an electrostatic environment where the potential is a solution of the Laplace equation ($\nabla^2\phi = 0$) and the boundary conditions are the interface conditions of the electromagnetic fields. The main advantage of the FEM lies in its ability to handle arbitrary geometries via unstructured meshes of the domain of interest. For the vast majority of physical geometries and problems, their PDEs cannot be solved analytically. The FEM divides the model into smaller elements of geometrically simpler shapes and solves these numerically easier subsets before assembling them together in a larger system of equations that models the entire problem.

2.7.1 The general principle

The finite element method will here be formulated using the weighted residual method, although it may also be described by the variational method [42]. A boundary value problem can be defined by a governing differential equation in a domain Ω,

$$\mathcal{L}\phi = f, \tag{2.55}$$

where $\mathcal{L}$ is a differential operator, f is the excitation or force function, and ϕ is the unknown quantity to be solved. In order to numerically solve the governing equation one must first discretize it. Discretization implies looking for an approximate solution ϕ_h to equation (2.55) in a finite-dimensional subspace to Hilbert space so that $\phi \approx \phi_h$.[6] This suggests that the approximate solution may be expanded as a linear combination of a set of *basis functions* v_i that belong to the subspace, so that [39]

$$\phi_h = \sum_{i=1}^{N} \phi_i v_i \tag{2.56}$$

where ϕ_i are the unknown expansion coefficients. The weighted residual method attempts to determine ϕ_i by first inserting equation (2.56) into (2.55), then integrate with a *weighting function* w_j over the entire domain Ω, which results in [41]

$$\int_\Omega w_j \mathcal{L}\left(\sum_{i=1}^{N} \phi_i v_i\right) \mathrm{d}\Omega = \int_\Omega w_j f \mathrm{d}\Omega. \tag{2.57}$$

Finally, given a set of weighting functions and applying the boundary conditions of the problem, equation (2.57) will define a set of linear algebra equations that can be solved for ϕ_i. By Galerkin's method [42] one chooses $w_j = v_j$, so that (2.57) becomes

$$\sum_{i=1}^{N} \phi_i \int_\Omega v_j \mathcal{L}(v_i) \mathrm{d}\Omega = \int_\Omega v_j f \mathrm{d}\Omega \qquad j = 1, 2, ...N \tag{2.58}$$

or equivalently [41]

$$\sum_{i=1}^{N} A_{ji}\phi_i = b_j \qquad j = 1, 2, ...N \tag{2.59a}$$

where

$$A_{ji} = \int_\Omega v_j \mathcal{L}(v_i) \mathrm{d}\Omega \tag{2.59b}$$

---

[6] A Hilbert space is an infinite-dimensional *function space*, which in simplified terms can be viewed as a collection of functions that can be conveniently manipulated in the same way as ordinary vectors in Euclidean space.

$$b_j = \int_\Omega v_j f \mathrm{d}\Omega. \tag{2.59c}$$

In matrix form, equation (2.59) becomes

$$\mathbf{A}\vec{\phi}_h = \mathbf{b} \tag{2.60}$$

where $\vec{\phi}_h = \{\phi_1, ..., \phi_i, ..., \phi_N\}$ is the vector of unknowns, and $\mathbf{A}$ is a $N \times N$ matrix known as the *system matrix* [39].

In short, FEM is a systematic way of first converting functions in an infinite dimensional function space (Hilbert space) to functions in a finite dimensional function space, and then to ordinary vectors (in a vector space) that are tractable with numerical methods.

2.7.2 Discretizing the domain

Classical methods for solving boundary-value problems such as the Ritz and Galerkin methods require a trial function defined over the entire solution domain which must represent, at least approximately, the true solution of the problem [42]. This is very difficult, often impossible, for two- or three dimensional problems having irregularly shaped solution domains. This can be overcome by dividing the entire domain into small subdomains and employ test (basis) functions defined over each subdomain. These test functions tend to be much simpler because of the small size of the subdomains, thus meaning that the variation of the unknown function to be solved (ϕ above) is less drastic over each subdomain.

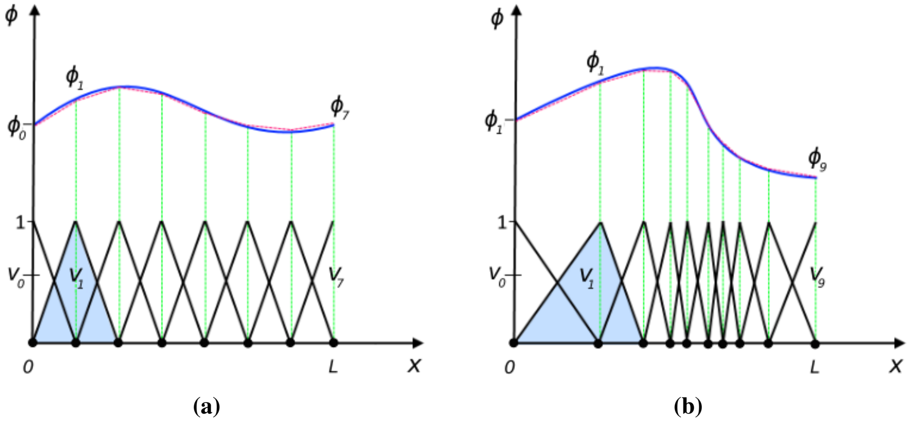

Figure 2.14: A one-dimensional domain is divided into segments (elements). The function ϕ is approximated to ϕ_h (marked in dashed red line) by linear combinations of linear basis functions v_i (solid black lines). Nodes are marked as black dots. Figures (a) and (b) illustrates different distributions of the elements. Modified figure from [39].

Equation (2.56) discretizes the original problem (2.55) into N subdomains using linear combinations of basis functions. Figure 2.14 illustrates this principle for a 1D problem. The solution domain $(0, L)$ is divided into small segments called *finite elements*, and the joints between them are known as *nodes*. An important feature of the basis functions is that they are non-zero only within the nearest neighbours of its respective node. Here, the basis function $v_i(x)$ has a value of 1 at node i, which decreases linearly to zero to the neighbouring nodes. The goal is to make the elements small enough so that the unknown solution over each element can be obtained by linear interpolation between the values of $\phi(x)$ at the two ends of the element. In other words, the denser the mesh, the closer the approximate solution will be to the physical solution.

Note that in figure 2.14a the elements are uniformly distributed over the domain. This does not have to be the case, in figure 2.14b more elements are concentrated in the region where the gradient of $\phi(x)$ is larger. An important advantage of FEM is that it offers great freedom in the selection of discretization. It is also worth mentioning that other interpolating functions may be chosen besides linear functions, depending on the problem at hand.

2.7.3 Assembling the subdomains

The next step in a FEM procedure is to combine all the local equations for all elements used for discretization. This process is known as *assembly*. One major advantage of the FEM lies in its ability to define basis functions that are supported only over a small geometrical region. This implies that the integral in the left-hand side of equation (2.58) is zero everywhere except for the few regions where v_i and v_j overlap, and thus the system matrix $\mathbf{A}$ becomes sparse. With a very sparse system matrix the linear system can be generated and solved efficiently [41].

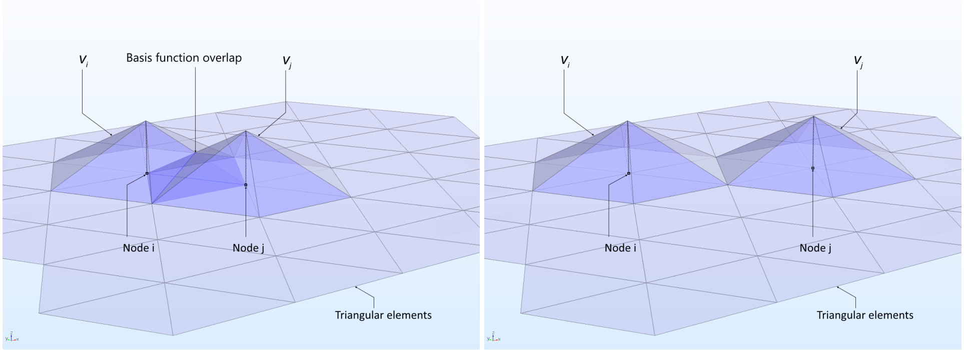

(a) **(b)**

Figure 2.15: A 2D domain discretized with triangular elements, basis functions v have a value of 1 at the corresponding node and zero on all other nodes. (a) Two neighbouring nodes that share an element have overlapping basis functions. (b) Two basis functions that do not share elements and thus have no basis function overlap, although they do have a common element vertex. Edited figure from [39].

Such basis functions are visualized in figure 2.15 where a 2D domain is discretized into a triangular mesh with linear basis functions with a value of 1 at their respective nodes and zero on all other nodes. In figure 2.15a two neighbouring nodes i and j are depicted. Their respective basis functions share two triangular elements and will thus have a non-zero contribution to the system matrix, as per equation (2.59b). If $i = j$ there is a complete overlap of the two basis functions. In figure 2.15b the nodes are further apart and share no elements except having a common element vertex. When there is no overlap between v_i and v_j their contribution A_{ij} to the system matrix is zero. Hence, in each row of $\mathbf{A}$ there will only be a few non-zero entries no matter how large the dimension of the matrix is. and the memory required to store the system matrix is thus proportional to $O(N)$ [41]. After imposing boundary conditions to obtain the final form of the matrix equation (2.60), it can be efficiently solved by linear solvers that exploit properties of sparse matrices [41]. FEM is therefore very suitable for large-scale applications with a large number of unknowns.

2.7.4 Finite element analysis of vector fields

The formulation of the finite element method so far is applicable to scalar fields. However, as all electrodynamic problems in three dimensions deal with vector electromagnetic fields, there is clear motivation to extend the formulation to include vector fields. This section will not go into details, but will rather mention the most important steps. The derivation is similar to section 2.7.1, but involves using vector basis functions which assigns degrees of freedom to the edges rather than to the nodes of the elements [42].

A typical electrodynamic problem involves finding the electric field $\mathbf{E}$ by solving Maxwell's equations (2.23) subject to certain boundary conditions. The problem may be reduced to solving a single vector wave equation with well defined boundary conditions. As before, instead of solving these equations directly, a weak form solution may be sought by introducing vector weighting functions $\mathbf{W}_j$ and integrating over the entire domain Ω. Discretization is obtained by first dividing the domain into small finite elements, typically triangular elements for a 2D domain and tetrahedral elements for a 3D domain. Within each element, $\mathbf{E}$ is interpolated using a set of discrete values. However, using the approach in section 2.7.1 — where the unknown field is assigned to a few points (nodes) on the element and then interpolated elsewhere using a set of scalar interpolation functions — turns out to be very problematic; a series of difficulties arise when applying boundary conditions to the interpolated $\mathbf{E}$-field [42] [41].

A better approach is to assign the tangential components of $\mathbf{E}$ along each edge of the element, $\mathbf{E}$ is then interpolated elsewhere by using a set of vector basis functions. For example, the field $\mathbf{E}^{(e)}$ in a triangular element e can be interpolated as [41]

$$\mathbf{E}^{(e)}(x,y) = \mathbf{V}_{12}^{(e)}(x,y)E_{12}^{(e)} + \mathbf{V}_{23}^{(e)}(x,y)E_{23}^{(e)} + \mathbf{V}_{31}^{(e)}(x,y)E_{31}^{(e)} \tag{2.61}$$

where $E_{lk}^{(e)}$ denotes the tangential components of $\mathbf{E}$ at the edge that connects nodes l and k of element e, and $\mathbf{V}_{lk}^{(e)}$ is the corresponding interpolation or basis function. Figure 2.16 illustrates the vector basis functions for element e. It is clear from the figures that the vector basis functions only have tangential components along their associated edge. They ensure tangential continuity of the interpolated field while allowing the normal component to be discontinuous[7]. Therefore, vector basis functions can be used to expand the vector field $\mathbf{E}$ accurately.

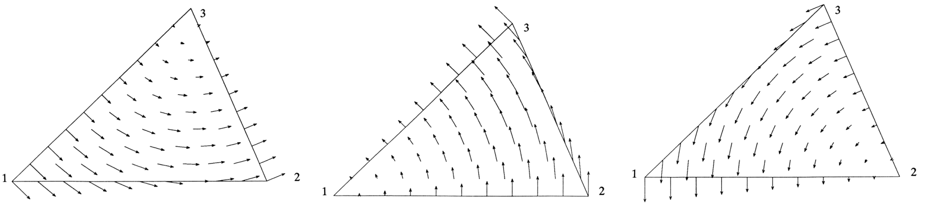

(a) **(b)** **(c)**

Figure 2.16: Vector basis functions for a triangular element e with the nodes 1, 2 and 3. (a) $\mathbf{V}_{12}^{(e)}$, (b) $\mathbf{V}_{23}^{(e)}$, and (c) $\mathbf{V}_{31}^{(e)}$ are the vector basis functions assigned along their corresponding element edges. Figure from [42].

When the electric field is interpolated in each element using tangential values at the element edges, the interpolated field $\mathbf{E}$ in the entire domain Ω can be expressed as

$$\mathbf{E} = \sum_{i=1}^{N_{\text{edge}}} \mathbf{V}_i E_i \tag{2.62}$$

where N_{edge} is the total number of edges, E_i denotes the tangential component of $\mathbf{E}$ at the ith edge, and $\mathbf{V}_i$ is the corresponding vector basis function. A system matrix equation, a vector field equivalent to equation (2.60), can then be found in a similar manner as in section 2.7.1; substituting equation (2.62) into the weak form solution of the wave equation and imposing the boundary conditions [41].

This has been an attempt at a more simplified explanation of the finite element method, focusing more on intuitive understanding rather than gritty mathematics (while at the same time not ignoring it entirely). The assembly process to form the system of equations (2.60), for example, is a much more intricate matter than presented, especially for vector fields.

2.7.5 Domain truncation methods

Electromagnetic problems often involve wave propagation in domains that extends to infinity. In numerical models this is usually overcome by truncating the computational domain to a finite domain, with external artificial boundaries that let waves pass through without any reflection. The most commonly used truncation techniques are the *artificial* (or absorbing) *boundary conditions* (ABC) and *perfectly matched layers* (PML). ABC techniques are more general than PML, however, PML can provide orders of magnitude lower reflections [64].

---

[7] At the interface between two different media the elecromagnetic field is in general discontinuous. Specifically, the component of the displacement field $\mathbf{D}$ perpendicular to the boundary between media A and B is discontinuous in the amount $D_{\text{A}}^{\perp} - D_{\text{B}}^{\perp} = \sigma_f$, while the parallel component of the electric field $\mathbf{E}$ is continuous across the boundary, $E_{\text{A}}^{\parallel} - E_{\text{B}}^{\parallel} = 0$. [31]

Scattering boundary condition

A form of ABC are is the *scattering boundary condition* (SBC), which is an approximation of the Sommerfeld radiation condition. The Sommerfeld condition is one of the first transparent boundary conditions formulated for wave-type problems, and can be written for 2D fields as

$$\lim_{r\to\infty} \sqrt{r}\left(\frac{\partial E_z}{\partial r} + ikE_z\right) = 0 \tag{2.63}$$

when the EM wave is propagating in the xy-plane and the E-field is polarized in the z-direction. This condition is exactly non-reflecting when the boundary lies infinitely far away from the source. Obviously, the Sommefeld condition can not be applied exactly to a finite modeling domain so an approximation of equation (2.63) must be made,

$$\mathbf{n} \cdot (\nabla E_z) + ikE_z = 0 \tag{2.64}$$

which is known as the first-order SBC [25].

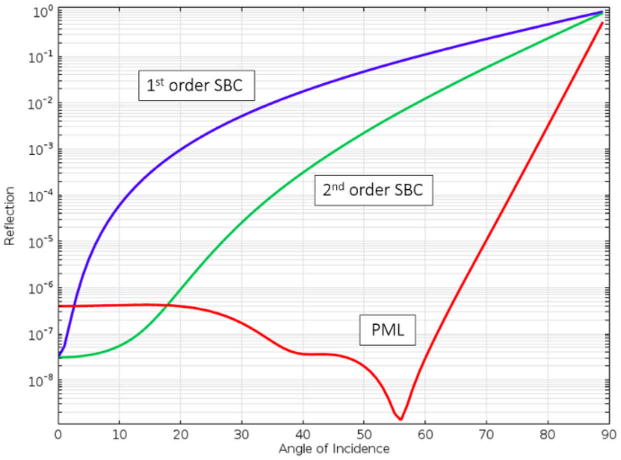

Figure 2.17: Reflection of a plane wave incident at the first- and second-order SBC, and PML boundaries with respect to angle of incidence. Figure from [25] where the data is from a FEM simulation using COMSOL Multiphysics.

A significant limitation to SBC is that it is only perfectly transparent for scattered (outgoing) waves at normal incidence to the boundary [37]. Second-order SBC is also possible which reduces reflection uniformly, see figure 2.17. However, there is still 10% reflection at an incidence angle of around 75°.

Perfectly matched layers

Perfectly matched layers were first introduced in 1994 by Berenger [9] for use with Maxwell's equations. As the name suggests, PMLs are absorbing boundary *layers* in contrast to absorbing boundary *conditions* of ABC. The layer is an artificial anisotropic absorbing material placed adjacent to the edges of the grid, as depicted in figure 2.18. As a wave propagates through the absorbing layer it is exponentially decayed. Even if it reflects off the outer boundary, the returning wave will be exponentially tiny after one round trip. PML is special in that it does not reflect at the interface between the physical domain and the absorbing layer, whereas one would otherwise expect reflection in the transition from one material to another [44].

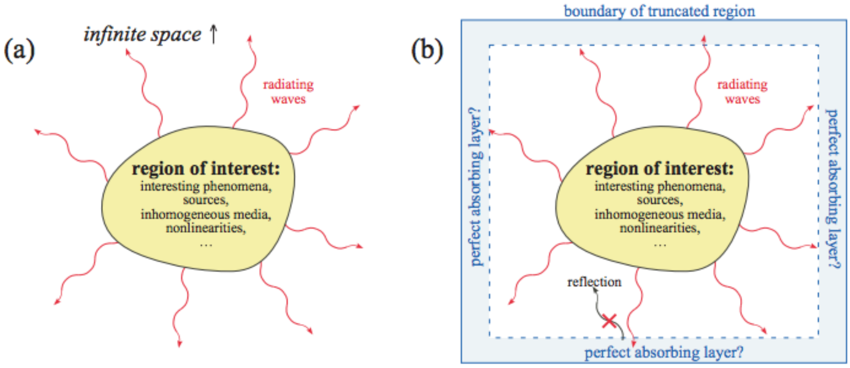

Figure 2.18: (a) A typical wave-equation problem; a region of interest where relevant phenomena are being investigated, from which some radiation escapes to infinity. (b) The same problem where space has been truncated to a finite computational domain. Absorbing layers are placed adjacent to the edges. A *perfect* layer should absorb the outgoing waves without reflection from the edge of the absorber. Figure from [44].

The original formulation by Berenger [9] was based on splitting the EM wave solutions into a sum of two artificial fields inside the PML region. Later, it was found that the PML could be derived from a modified form of Maxwell's equations based on stretched coordinates [17]. This complex-coordinate approach is essentially based on analytic continuation of Maxwell's equations into complex spatial coordinates where the fields are exponentially decaying [44]. In implementing PML to the finite element method, the preferred approach is to consider the PML as an anisotropic medium, a derivation can be found in [41].

PML is perfectly reflectionless only when solving the exact wave equations. As soon as the problem is discretized (as in FEM) to an approximate wave equation, the analytical perfection of PML is no longer valid. The PML is still an absorbing material; the discrete waves within the layer are still being attenuated. However, the boundary between the PML and the regular medium is no longer reflectionless, but these reflections are small as long as the discretization is a good approximation of the exact wave equation [44]. To further minimize this reflection it is desirable to use a mesh in the PML that aligns with the anisotropy in the material properties [25]. In figure 2.19 the appropriate PML meshes are shown for 2D circular and 3D spherical domains, with 5 layers uniformly distributed.

In figure 2.17 a plane wave is incident on either a SBC or a PML boundary, modelled in the FEM software COMSOL Multiphysics [25]. The PML reflects the least amount across the widest range, however, there is still reflection when the incident wave is almost parallel to the boundary. A major advantage of PML over ABC in general, is that their absorbing performance can be improved systematically by simply increasing the number

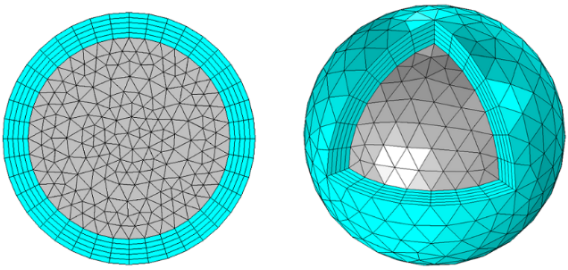

Figure 2.19: Appropriate meshes for 2D and 3D spherical PMLs. Figure from [25].

of layers [41]. The flexibility of FEM also permits the use of non-rectangular PMLs.

It is worth to note that PMLs do not absorb evanescent solutions to the wave equation [11] [12]. Numerical reflection observed in wave-structure interaction problems may therefore be interpreted as the reflection of evanescent fields surrounding the structures [12]. A simple fix is to make sure the computational domain large enough so that the evanescent waves decay before hitting the boundary.

Chapter 3

Experimental

This chapter will introduce the experimental samples that will be investigated by computational FEM models. Background information about their fabrication and characterization processes will be given, as well as any special considerations that had to be taken into account when implementing them into COMSOL that would differentiate them from their experimental counterparts. A total of four nanostructures will be studied in this thesis, three of them were created as part of the thesis work of Brakstad [14] and the final sample was prepared as part of the doctorate dissertation of Aas [35].

3.1 Hemispheroidal gold particles on SiO_2 substrate

In the thesis works of Brakstad [14], several 3-material nanostructures were manufactured consisting of Au-nanoparticles on a flat SiO_2 substrate in air. The substrates were covered with a thin gold film by an e-beam evaporator[1] before the nanostructures were milled out with focused ion beam (FIB) microscopy[2]. The nanostructures appeared as Au hemispheroids distributed in a square or rectangular pattern on a glass surface, see figure 3.1. Three chosen structures from this work will henceforth be discussed, known as sample 6, sample 5A and sample 5B. The deposited Au film thickness before milling were 40nm (samples 5A and 5B) and 20nm (sample 6). These samples were characterized by scanning electron microscopy[3] (SEM) images and MM ellipsometer measurements [14], while samples 5A and 6 were further discussed in detail by M. Kildemo et al. [15] [47]. The ellipsometric measurements done in [14] were performed with a RC2 ellipsometer provided by J.A. Woollam Co., with spectral range from 210 nm (5.9 eV) to 1700 nm (0.73

---

[1] Electron beam physical vapor deposition; a vacuum deposition method used to produce thin films and coatings. An electron beam evaporates atoms from a target anode under high vacuum, causing everything in the vacuum chamber to be coated with a thin layer of the anode material [61].

[2] FIB systems use a finely focused beam of ions (usually gallium) that can be operated at low beam currents for sample imaging or high beam currents for surface manipulation of the sample via sputtering or milling [62].

[3] SEM is a type of electron microscope that produces images by scanning the surface of a sample with a focused beam of electrons. The electrons interact with the atoms of the sample which produces signals that contains information about the surface composition and topography.

eV). In addition, full azimuthal rotational measurements (varying ϕ_0) were done for three polar angle of incidences, θ_0, in order to identify symmetries caused by any anisotropic geometries in the fabricated samples. For all samples there were found next to zero depolarization. They were also shown to exhibit rich optical responses supporting LSPRs [14].

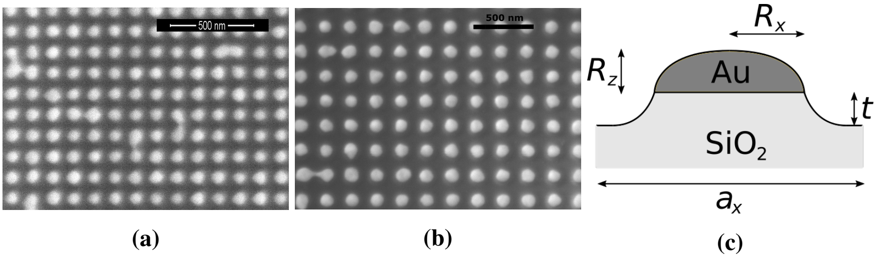

(a) (b) (c)

Figure 3.1: SEM images of (a) sample 6 and (b) sample 5A. (c) Cross-section in xz-plane of the unit cell setup of the gold hemispheroidal particles on a glass substrate.

An unintended effect of the milling process caused an over-etching into the substrate of several nanometers, suggesting that each Au particle on all the samples lies on top of a dielectric mound, as sketched in figure 3.1c (however, the exact shape of the mound can only be speculated). This can also be observed by close inspection of figure 3.1b, where a vague mound geometry can be made out surrounding each particle. The geometry of all three samples are characterized by their lattice constants $a_{x,y}$, Au particle radii $R_{x,y,z}$ and the thickness t of the SiO$_2$ mound as depicted in figure 3.1c.

3.1.1 Sample 6

Sample 6 was originally made in an attempt to fabricate small dots operating within the quasi-static approximation arranged in a square array, ideally with particle radius 20 nm and lattice constant 125 nm [14]. However, after the milling, the particles were derived from SEM images to be hemispheroids with lateral radius $R_{xy} = 38$nm and lattice constant $a_{xy} = 125$nm, see figure 3.1c. A SEM image of the sample is shown in figure 3.1a. Through a combination of atomic-force microscopy[4] (AFM) and SEM images, the total height of particle and mound were roughly estimated to be 40 nm. The relative contributions from the particle height R_z and mound height t to the total height were difficult to estimate. The perpendicular radius R_z was initially assumed to be equal to the thickness of the Au thin film of 20 nm. However, COMSOL simulations using 20 nm for both particle and mound height resulted in a redshift of the LSPR compared to experimental data. Under the assumption that the lateral parameter estimations were accurate, a parameter sweep of R_z and t was performed in the COMSOL model of sample 6. The set of parameters with a resulting LSPR resonance closest resembling that of the experimental results were chosen. This concluded in $R_z = 32$ nm and $t = 8$ nm, where the particle height exceeds the initial

---

[4] AFM is a type of scanning probe microscopy. Information about the sample is gathered by probing the surface with a mechanical cantilever with a sharp tip attached to its end. Forces between the tip and the sample leads to a deflection of the cantilever which is measured by a detector [63].

film thickness. However, the uncertainty associated with the profiling of the total height must be emphasized.

3.1.2 Sample 5A

Sample 5A was originally created as one in a series of similar nanostructures to investigate how the distance between the Au spheres influence the LSP resonance energy. Ideally, the sample was designed to have radius 40 nm and lattice constant around 208 nm [14]. SEM images after milling found the parameters to be 52 ± 7 nm and 210 ± 18 nm for radius and lattice, respectively [14], see figure 3.1b. In an attempt to more accurately determine the sample parameters, a Bedeaux-Vlieger formalism [8] was initially used by fitting the experimental data sets with respect to the morphological parameters of the spheroidal lattice (R_{xy}, R_z, a_{xy}) using the GranFilm software[5] [47] [15]. Further research [6] using an algorithm based on the reduced Rayleigh equation[6] (RRE) [74] found the lattice to be rectangular and the Au particle slightly elliptic in the lateral direction. The mound thickness was also adjusted [6]. The final sample 5A parameters used in the simulations are found in table 3.1.

3.1.3 Sample 5B

Sample 5B is a biaxial anisotropic system due to the high eccentricity of the Au particles and rectangular lattice, as seen in figure 3.2a, with ideal lattice constants $a_1 \approx 312$ nm and $a_2 \approx 454$ nm. The ellipses were milled out of a 40 nm Au film. After milling, SEM images (see figure 3.2b) found minimal Au redeposition on the sample, and with parameters $R_1 \approx 19 \pm 19$ nm, $R_2 \approx 50 \pm 8$ nm and $a \approx 495 \pm 26$ nm [14]. The sample was created for the purpose of observing how different dielectric functions in each of the three spatial directions would present itself in the ellipsometric data.

The same RRE optimization process was done for sample 5B parameters as for sample 5A. A mound thickness of around 15 nm was found by studying the total height profile from AFM images and subtracting particle height R_z found from the parameter fitting procedure. An indication of a dielectric mound can also be observed around each Au particle by close inspection of figure 3.2b. The sample was found to be computationally demanding when implementing it into COMSOL, due to the extreme amount of finite elements to solve in such a large unit cell system. In fact, the COMSOL model did not yield a solution which converged for the lowest desirable wavelength (210 nm) for this sample[7]. A compromise of sacrificing the dielectric mound had to be made in order to solve the model for a satisfactory low wavelength (further explained in section 5.5.2), since resolving the mesh in the curved mound geometry requires a significant amount of elements for all wavelength iterations. In other words, sample 5B was simulated with a flat substrate surface (no mound).

---

[5] `http://web.phys.ntnu.no/~ingves/Software/GranFilm/`

[6] The reduced Rayleigh equation was combined with the angle-resolved spectroscopic Mueller matrix ellipsometric data to produce a numerically efficient and reliable method for reconstructing the geometrical parameters of the 2D photonic crystal [6].

[7] The mesh resolution, or in other words the amount of elements, will depend on the size of the geometry compared to the wavelength. See sections 4.2.2 and 5.1.3.

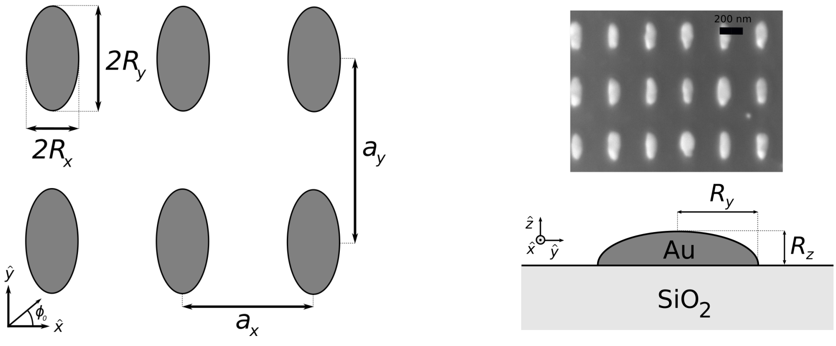

(a) (b)

Figure 3.2: (a) Top view schematic of sample 5B. Azimuthal angle of the incident beam ϕ_0 is defined along positive x-direction. (b) Above: SEM image of sample 5B. Below: schematic side view of the sample when neglecting the mound.

The geometric parameters that ended up being used in COMSOL simulations for the three samples are summarized in table 3.1.

Table 3.1: Parameters (given in nanometers) for different samples of gold hemispheroidal particles defined by the radii R_x, R_y and R_z over a SiO2 substrate, evenly distributed on a grid defined by lattice constants a_x and a_y. Each particle lies on top of a SiO2 mound of height t, except sample 5B which lies on a flat substrate.

	Sample 6	Sample 5A	Sample 5B
a_x	125	207.2	315.4
a_y	125	209.9	443.9
R_x	38	60.3	47.4
R_y	38	61.3	113.2
R_z	32	34.8	34.4
t	8	36.9	0

3.2 Tilted GaSb cones

Ion beam sputtering of flat surfaces can in some circumstances lead to spontaneous formation of nanoscale patterns, a phenomena which could open alternative ways of controlling the surface roughness of functional materials [65]. A distinct type of pattern formation can be found for sputtering on certain semiconductors, like GaSb. These materials form pillar patterns, and GaSb is considered to be the most conspicuous example [65].

In the works of [35], densely packed GaSb nanocones are formed by sputtering a clean

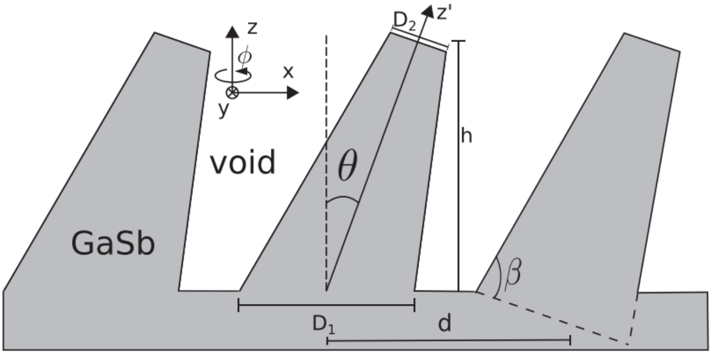

Figure 3.3: Tilt angle θ of the GaSb nanocones, the height h, the bottom and top diameters D_1 and D_2, the average distance to nearest neighbour d, and base angle β. Sketch taken from [35].

GaSb substrate by low energy Ar+ ions using ion beam sputtering (IBS)[8]. A misalignment of the ion gun caused a slight tilt of the cones, which were originally intended to be directed normal to the substrate surface [35]. A sketch visualizing the cone geometry is shown in figure 3.3, defining the tilt angle θ, height h, nearest neighbour distance d, and the bottom and top diameters D_1 and D_2.

Ellipsometric characterization of such structures are particularly interesting since shadowing effects can render atomic force microscopy ineffective [66]. The anisotropic electronic characteristics of the sample was determined by spectroscopic Mueller matrix ellipsometry, using a RC2 ellipsometer from J.A. Woollam Co., where Bruggeman effective medium model was applied to model the spectroscopic data [35]. The anisotropic Bruggeman model is essentially a generalization of equation (2.40) for ellipsoidal inclusion by applying the polarizability of an ellipsoid (2.48). Through mathematical models, parameters like the tilt of the cones θ, the relative diameters D_1 and D_2, and the average height of the cones h were found [35]. Average cone separation d was found using another non-destructive technique called Grazing-Incidence Small-Angle X-ray Scattering (GISAXS) where surface sensitivity is obtained by using a grazing incident angle of X-rays [35]. AFM analysis found the cones to be distributed with six nearest neighbours, which allows an assumption of a hexagonal lattice [35]. GISAXS was also used to confirm film anisotropy induced by the nanopillar tilt [35]. These sample parameters are summarized in table 3.2.

The main motivation of modeling these tilted GaSb cones is to attempt a continuation of the COMSOL model for other periodic nanostructures than the gold hemispheroids on glass substrate, which the model initially will be tailored for. The nanocones differ greatly from the other samples in both size, shape, and material properties. The dense cone distribution should not be represented by a square lattice, meaning that the model must be expanded to include support for hexagonal lattices. The secondary objective is to

---

[8] IBS is a sputter deposition method in which the target is external to the ion source. An ion beam strikes and sputters a target of material, which then coats the substrate tilted toward the target with the sputtered material. The properties of the resulting film will depend on the target material properties and on the ion sputter beam parameters (flux, energy, etc.) as well as the chamber ion source-target-substrate configuration.

Table 3.2: Parameter values for tilted cones of GaSb as found in [35].

h	39 nm
θ	4.8°
D_1	d
D_2	0.04d
d	40 nm
β	64°

attempt a high energy simulation up to 24 eV to model the response the ellipsometer and the anisotropic Bruggeman model[9] is unable to capture.

---

[9] EMA models are limited to structures sufficiently smaller than the wavelength of light, i.e. the electric field is assumed to be constant over an inclusion in the mixed material so that the phase of the wave is approximately the same over the size of the inclusion. Models taking into account retardation effects must be applied for smaller wavelengths.

Chapter 4

COMSOL Multiphysics

4.1 Introduction to COMSOL

COMSOL Multiphysics is a commercial finite element analysis, solver, and simulation software for desktop computers designed for various disciplines in physics and engineering, namely within electrical, mechanical, fluid and chemical applications. It supports coupling phenomena, or multiphysics, where a simulation may treat multiple models or multiple physical phenomena simultaneously. Typically this involves solving coupled systems of partial differential equations.

The main product is COMSOL Desktop, which supports a unified workflow for cross-disciplinary model building. Several add-on products are available to the software, each categorized according to application areas, namely Electrical, Structural & Acoustics, Fluid & Heat, Chemical, Multipurpose and Interfacing. Examples of add-on modules are the plasma module, semiconductor module, structural mechanics module, microfluids module, corrosion module, and the particle tracing module, to name a few [37]. This thesis will work solely on the wave optics module, which will be introduced in the next section. The software has an integrated user-interface environment, as exemplified in figure 4.1, where the way of operation of the software remains the same regardless of which application module is installed. Using the built-in physics interface together with a vast support for material properties, one may build models by defining physical quantities such as geometry, material properties, boundary conditions, sources and fluxes, rather than defining the underlying equations. The software will internally compile a set of equations to represent the entire model. However, equation-based modeling is also supported [37].

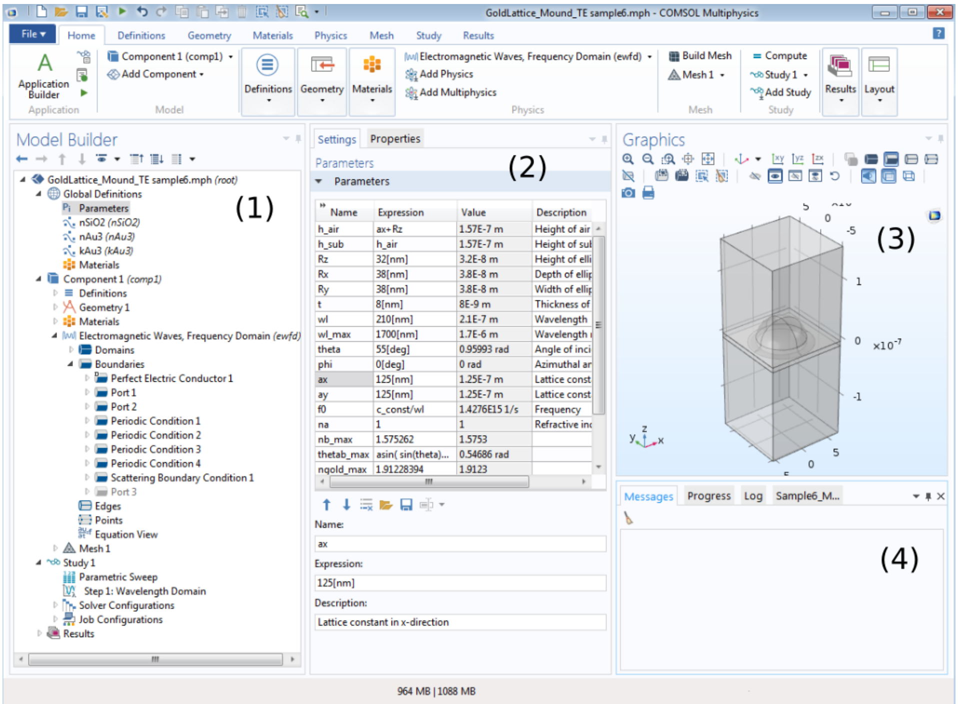

Model Builder

- GoldLattice_Mound_TE sample6.mph *(root)*
  - Global Definitions
    - Parameters
    - nSiO2 *(nSiO2)*
    - nAu3 *(nAu3)*
    - kAu3 *(kAu3)*
    - Materials
  - Component 1 *(comp1)*
    - Definitions
    - Geometry 1
    - Materials
    - Electromagnetic Waves, Frequency Domain *(ewfd)*
      - Domains
      - Boundaries
        - Perfect Electric Conductor 1
        - Port 1
        - Port 2
        - Periodic Condition 1
        - Periodic Condition 2
        - Periodic Condition 3
        - Periodic Condition 4
        - Scattering Boundary Condition 1
        - Port 3
      - Edges
      - Points
      - Equation View
    - Mesh 1
  - Study 1
    - Parametric Sweep
    - Step 1: Wavelength Domain
    - Solver Configurations
    - Job Configurations
  - Results

Settings Properties

Parameters

Parameters

Name	Expression	Value	Description
h_air	ax+Rz	1.57E-7 m	Height of air
h_sub	h_air	1.57E-7 m	Height of sul
Rz	32[nm]	3.2E-8 m	Height of elli
Rx	38[nm]	3.8E-8 m	Depth of ellip
Ry	38[nm]	3.8E-8 m	Width of ellip
t	8[nm]	8E-9 m	Thickness of
wl	210[nm]	2.1E-7 m	Wavelength
wl_max	1700[nm]	1.7E-6 m	Wavelength
theta	55[deg]	0.95993 rad	Angle of inci
phi	0[deg]	0 rad	Azimuthal ar
ax	125[nm]	1.25E-7 m	Lattice const
ay	125[nm]	1.25E-7 m	Lattice const
f0	c_const/wl	1.4276E15 1/s	Frequency
na	1	1	Refractive inc
nb_max	1.575262	1.5753	
thetab_max	asin(sin(theta)...	0.54686 rad	
ngold_max	1.91228394	1.9123	

Name:
ax
Expression:
125[nm]
Description:
Lattice constant in x-direction

964 MB | 1088 MB

Figure 4.1: The user interface in COMSOL Desktop. (1) Model builder; overview of the model. Right-clicking a node will access context-sensitive menus. (2) Settings window; clicking a node in the model builder will display associated settings (3) Graphics window; presents interactive graphics for the Geometry, Mesh and Results nodes. (4) Information window; will display vital information during and after simulations such as solution time, simulation progress, mesh statistics and result tables.

4.1.1 Model builder

A COMSOL model is controlled through the *Model builder*, seen in figure 4.1, which essentially is a model tree containing the functionality and operations for building, solving, and displaying the results of a model. It consists of the main nodes *Global Definitions* (where global parameters and materials used throughout the model are defined), *Component* (the fundamental part of the model containing the model geometry with its associated physics, mesh and variables that are local to the component), *Study* (where study steps are defined that form a solver configuration that computes the solution for the study) and *Results* (contains tools for post-processing and analyzation of the results).

The Component node further consists of subnodes *Definitions*, *Geometry*, *Materials*, one or several physics interfaces, and *Mesh*. Some of these are explained in more detail below,

- The model geometry is defined by a sequence geometric objects and operations under the Geometry node in the Model Builder. Geometries can be formed as a combination of solid objects using Boolean operations like union, intersection, and difference. Furthermore, 3D objects can be formed by defining 2D solids and then extruding or revolving these into 3D solids.

- In the Material node material properties are assigned to the geometric domains. The materials may be chosen from an integrated materials library, or user-specified materials defined under the Global Definitions node.
- The physics interface varies depending on which add-on module the user has chosen. In the example figure 4.1, the physics interface is *Electromagnetic Waves, Frequency Domain* (EWFD), which is part of the Wave Optics module.
- The Mesh node specifies how the geometry should be discretizied. The user may customize their own mesh or automatically generate a physics-controlled mesh based on the configurations set in the associated physics interface.

4.2 The wave optics module

The Wave Optics Module extends the functionality of COMSOL's physics interface to include dedicated tools for electromagnetic wave propagation in linear and nonlinear optical media. The module can be used to solve EM wave problems at optical frequencies (corresponding to wavelengths in the nm to μm region) in either frequency- or time-domain in optical structures. It supports inhomogeneous and anisotropic materials, media with gains and losses, and complex-valued material properties.

4.2.1 S-parameters

Scattering parameters (S-parameters) are used to characterize the response in high-frequency problems. In the Wave Optics module of COMSOL, electromagnetic waves can be excited by *ports*, which is also where EM energy enters and exits the model. In 3D models, ports are fictitious planes placed on the boundaries. To convert EM field patterns on a port to a quantity describing its wave-like nature it is necessary to introduce these S-parameters. S-parameters are complex-valued, frequency dependent matrices describing the transmission and reflection of electromagnetic waves at different ports.

S-parameters originate from transmission-line theory and are defined in terms of transmitted and reflected voltage waves. There is assumed to be no reflection directly at a port. For a model with n ports, the S-parameters are [38]

$$S = \begin{pmatrix} S_{11} & S_{12} & \dots & S_{1n} \\ S_{21} & S_{22} & \dots & S_{2n} \\ \vdots & \vdots & \ddots & \vdots \\ S_{n1} & S_{n2} & \dots & S_{nn} \end{pmatrix} \tag{4.1}$$

where S_{11} is the voltage reflection coefficient at port 1, S_{21} is the voltage transmission coefficient from port 1 to port 2, and so on. The reflectance/transmittance coefficients are obtained as $|S_{ij}|^2$.

S-parameter calculations

The S-parameters are defined in terms of the electric field. Consider a model containing several ports labeled 1, 2, 3, ... and that the electric field patterns $\mathbf{E}_1$, $\mathbf{E}_2$, $\mathbf{E}_3$, ... of the fundamental modes on these ports are known. Assume that the fields are normalized with respect to the integral of the power flow across each port cross section, respectively. Port 1 is excited using the fundamental eigenmode. The computed electric field $\mathbf{E}_c$ on port 1 then consists of the excited field plus the reflected field, which can be expanded in terms of the mode fields as [42]

$$\mathbf{E}_c = \mathbf{E}_1 + \sum_{i=1} S_{i1}\mathbf{E}_i, \tag{4.2}$$

whereas the computed field on all the other port boundaries are given by

$$\mathbf{E}_c = \sum_{i=1} S_{i1}\mathbf{E}_i. \tag{4.3}$$

Note that in this case $S_{ij} = 0$ for all $j \neq 1$ as there are no fields being excited on other ports than port 1. The S-parameter for mode k is then given by multiplying the field delivered to port k with the conjugate of field for mode k, and integrating over the port boundary. The first three S-parameters are given by [38]

$$S_{11} = \frac{\int_{\text{port1}}(\mathbf{E}_c - \mathbf{E}_1)\cdot\mathbf{E}_1^* dA_1}{\int_{\text{port1}}\mathbf{E}_1\cdot\mathbf{E}_1^* dA_1} \tag{4.4a}$$

$$S_{21} = \frac{\int_{\text{port2}}\mathbf{E}_c\cdot\mathbf{E}_2^* dA_2}{\int_{\text{port2}}\mathbf{E}_2\cdot\mathbf{E}_2^* dA_2} \tag{4.4b}$$

$$S_{31} = \frac{\int_{\text{port3}}\mathbf{E}_c\cdot\mathbf{E}_2^* dA_3}{\int_{\text{port3}}\mathbf{E}_3\cdot\mathbf{E}_2^* dA_3} \tag{4.4c}$$

To get S_{22} and S_{12} port 2 can be excited in the same way.

4.2.2 The *Electromagnetic Waves, Frequency Domain* interface

The Electromagnetic Waves, Frequency Domain (EWFD) interface in COMSOL's Wave Optics module is used to solve for time-harmonic electromagnetic field distributions. The main governing equation in the interface is the time-harmonic wave equation for the electric field. The EWFD supports study types in wavelength and frequency domains (among others [38]), used for source driven simulations for a single wavelength/frequency or a sequence of wavelengths/frequencies.

For this physics interface, the maximum mesh element size should be limited to a fraction of the wavelength. Thus, the domain size that can be simulated scales with the wavelength and the amount of available computer memory. By default, COMSOL Multiphysics uses second-order elements[1] to discretize the governing equations [26], in contrast to the first-order elements illustrated in figures 2.14 and 2.15 with linear basis functions. As a

---

[1] Element order refers to the type of basis function used.

bare minimum, two elements per wavelength are then necessary to solve the problem[2], but such a coarse mesh would result in poor accuracy.

In order to properly resolve the wavelength, at least five second-order elements per wavelength are typically used to resolve a wave propagating through a dielectric medium [24]. Local material properties should also be taken into account. In other words, a physically reliable solution requires the mesh to have a *maximum element size* (MES) no larger than

$$\text{MES} \leq \frac{\lambda}{5n}, \tag{4.5}$$

where n is the refractive index of the given region. For discretization into first-order elements, at least 10 linear elements are required per wavelength [38].

Periodic structures

Periodic structures may be modelled by truncating the domain into a single cell with periodic conditions on selected boundaries to set up a periodicity. A typical type of periodic condition used for models involving plane waves interacting with periodic structures is *Floquet periodicity*, which ensures a phase shift between the tangential components of the wave. The phase shift is determined by a wave vector and the distance between the source and destination [38].

When modelling periodic structures, *periodic ports* can be used to define wave direction and polarization of the wave that enters the model. Periodic ports also compute the reflected and transmitted diffraction orders as a function of incident angles and wavelength, in addition to the fundamental mode [23].

---

[2] The idea is fundamentally similar to the Nyquist sampling theorem in signal processing, which states that in order to recover all Fourier components of a waveform, the sampling rate must be at least twice the highest frequency of the signal.

Chapter 5

Results and discussion

This chapter begins with a discussion surrounding the development of the COMSOL model. First, a detailed explanation of how to set up the model is given in 5.1, followed by measures taken to optimize its performance and accuracy in 5.2. In sections 5.3-5.6 the results and analysis of each sample simulations will be given. The experimental data will be briefly presented first before discussing the COMSOL results.

The entire simulation process, including set-up of model and calculations, were performed on a desktop computer equipped with 32 GB RAM and an Intel Core i7-3930K CPU with 6 physical cores (each with 2 logical cores) operating at clockspeed 3.20 GHz, and running on a 64-bit Windows 7 operating system.

5.1 Implementation of samples into COMSOL

All samples presented in chapter 3 were implemented as a single cell with periodic conditions simulating the infinite periodic 2D lattice. The protruding gold semispheres lies in a square or rectangular lattice, while the densely packed distribution of the tilted GaSb cones were modeled as a hexagonal lattice.

The model set-up is similar for all the structures, especially for the gold hemispheroidal nanostructures, as they all have square or rectangular lattices and differ only by the numerical values of their sample parameters. The GaSb cones model is in principle exactly the same, differing only in particle geometry and lattice type. Samples 6, 5A and 5B were exposed to light waves incident with polar angle $\theta_0 = 55°$, while the GaSb cones were excited by light with $\theta_0 = 45°$.

5.1.1 Geometry and materials

Creating the geometries in COMSOL is a straightforward manner of combining solid blocks and ellipsoids with Boolean operations as previously mentioned in section 4.1.1. The mound region was created by first defining its cross-section, then sweeping it along the rim of the base of the Au particle, as depicted in figure 5.1. The finished geometries for all the samples can be seen in figure 5.2, while figure 5.3 shows the entire computational domain.

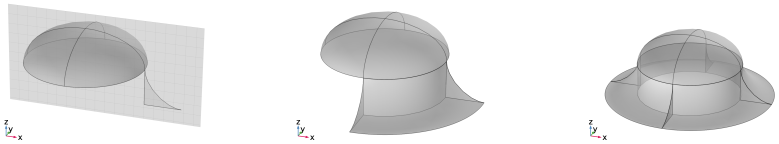

Figure 5.1: The creation of the dielectric mound. The mound cross-section is defined in a workspace placed in the xz-plane, before being swept along the base of the Au particle creating a solid 3D object.

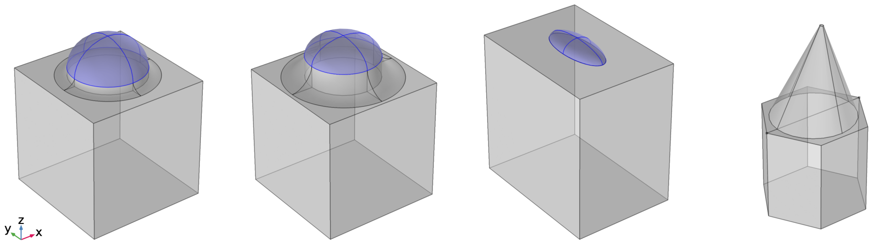

(a) **(b)** **(c)** **(d)**

Figure 5.2: The physical geometries of the various periodic nanostructures implemented into COMSOL; (a) sample 6, (b) sample 5A, (c) sample 5B, and (d) tilted GaSb cones. Highlighted blue areas in (a)-(c) marks Au domains. Air domains and PMLs are hidden for improved visibility.

The materials used in the models were defined by complex refractive indices of Au, SiO_2, and GaSb. The refractive indices were linearly interpolated imported data tables identical to the ones used in the ellipsometric modelling of the experimental results. The gold and glass dielectric functions were retrieved from the J.A. Woollam database, where the Au dielectric function was found to be in good correspondence with that extracted from the ellipsometric measurements done on the gold film [14]. The GaSb dielectric function in the range $0.6 - 24$ eV was determined using a combination of ellipsometry and synchrotron-based vacuum-UV ellipsometry [46].

5.1.2 The EWFD interface

Two periodic ports were defined as entry and exit boundaries of the physical domain: one on the top boundary of the physical air domain (port 1) and one on the bottom boundary of the substrate domain (port 2), see figure 5.3a. Port 1 excites an EM wave with polar angle of incidence (AOI) θ_0 and azimuthal AOI ϕ_0, while also absorbing outgoing (reflected) waves. Port 2 is a listener node, absorbing outgoing (transmitted) waves polar incident at an angle $\theta_1 = \arcsin[\sin\theta_0 n_{\text{air}}/n_{\text{sub}}(\lambda)]$ and azimuthal incidence $\phi_1 = \phi_0$. Each periodic port is additionally equipped with diffraction ports absorbing specific modes. Most notably, port 3 (top) and port 4 (bottom) read waves of the fundamental mode polarized orthogonal to the wave entering the model. The incident wave excited at port 1 is linearly polarized in either p- or s-polarization, with electric field amplitude 1 V/m. Floquet periodicity is applied to boundaries shown in figures 5.3b and 5.3c

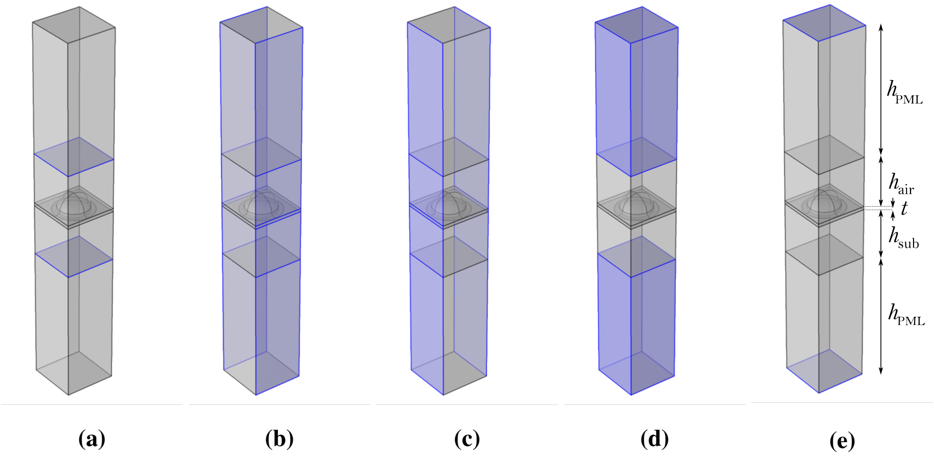

(a) **(b)** **(c)** **(d)** **(e)**

Figure 5.3: Setup of the EWFD interface; (a) top highlighted boundary: port 1 and port 3, bottom highlighted boundary: port 2 and port 4; (b)-(c) periodic boundary conditions subject to Floquet periodicity; (d) PML domains; (e) SBC boundaries. In addition, the heights of PML region h_{PML}, air domain h_{air}, substrate domain h_{sub} and mound thickness t are defined.

PML domains are shown in figure 5.3d, while the physical domain is considered to be the volume between port 1 and 2. Because a PML region acts as an infinite open domain, any boundary conditions and material properties must be carried over to the PML region. Thus, the PML domain share the same Floquet periodicity as the physical domain as figures 5.3b and 5.3c shows. The upper and lower PML domains also share the refractive indices of the interior region they are adjacent to, i.e. air and substrate, respectively. First order SBC were implemented in addition to PMLs to further reduce reflection at normal incidence and were not expected to have noticeable influence on computation cost. These boundaries are shown in figure 5.3e.

5.1.3 Meshing

Periodic boundaries must have compatible meshes. That is, boundary layers on opposing sides must be equal in order to properly simulate the infinite structure. Using figure 5.3b as an example, the meshed boundary of the highlighted walls must be exact copies of each other, and similarly for the highlighted walls in figure 5.3c.

In choosing the maximum element size, a satisfactory compromise between accuracy and computational memory usage was found to be

$$\text{MES} = \frac{\lambda}{6n_i}, \tag{5.1}$$

where n_i is the (real part) refractive index of either air, $\mathrm{SiO_2}$, Au, or GaSb. Convergence tests were performed with mesh factors $1/5$, $1/6$ and $1/8$, where all three gave reasonably similar results (not shown) so that we could assume a convergence limit was within close vicinity. Mesh factor $1/8$ proved to be extremely costly in terms of computation time and memory usage, while the (assumed[1]) increase in accuracy was marginal. A convergence limit appeared to be approached already at factor $1/5$, while the computations were completed six times faster than a similar simulation with $1/8$ mesh factor. The difference in solution time and memory usage was not merely as drastic between mesh factors $1/5$ and $1/6$ in terms of what the desktop computer could handle, so equation (5.1) was deemed to be adequate.

5.1.4 Study steps

The models were solved with a parametric sweep over wavelength λ with stepsize $\Delta\lambda = 5$ nm over a wide spectrum, typically 210 nm to 1600 nm which is approximately the same as the detection range of the RC2 ellipsometer used in the experimental works. For each wavelength, a full 360 degree sweep was performed for azimuthal AOI ϕ_0 with stepsize $\Delta\phi_0 = 5^\circ$ using a study extension called *auxiliary sweep*. Auxiliary sweep uses the solution from a previous parameter as a trial function for the current parameter, thus essentially re-using a previously calculated system matrix (equation (2.60)). Being relieved the burden of assembling the system matrix for every iteration of ϕ_0 will in principle greatly reduce the computation time compared to iterating through a regular parameter sweep where COMSOL solves the problem for each parameter from scratch[2].

COMSOL uses an internal convergence criterion where the iterations will be prematurely terminated if the relative tolerance exceeds the relative error computed [37]. These models use the default relative tolerance of 0.01%.

5.1.5 S-parameter conversion

The model is limited to excite only one specified polarization during the computation process. In order to derive a Mueller matrix response, two separate simulations must be run; one where the incident wave is p-polarized, and the other s-polarized. However, two instances of the COMSOL application may run simultaneously on the desktop computer which in practice halves the computation time.

The complex reflection coefficients are found from waves absorbed at ports 1 and 3, i.e. S-parameters S_{11} and S_{31}, so that

$$r_{pp} = S_{11}^{(p)} e^{i\xi} \tag{5.2a}$$

$$r_{sp} = S_{31}^{(p)} e^{i\xi} \tag{5.2b}$$

$$r_{ps} = S_{31}^{(s)} e^{i\xi} \tag{5.2c}$$

$$r_{ss} = S_{11}^{(s)} e^{i\xi} \tag{5.2d}$$

---

[1] Converging result does not always mean correct result.

[2] Source: private communcations with COMSOL support team and online forums.

where $S_{i1}^{(k)}$ specifies a k-polarized wave excited from port 1 and absorbed on port i, and $\xi = 2k_z d = 2kn_a \cos\theta_0 d$ where n_a is the refractive index of the ambient (air), θ_0 is the incident polar angle, and d is the distance from reflection point to the port. The exponential factor accounts for the phase shifts induced between the ports and the virtual interface at the top of the Au particles or GaSb cones. We remind the reader that the notation $r_{\alpha\beta}$ indicates conversion from β-polarization to α-polarization after reflection. Similarly, one may find the complex transmission coefficients from ports 2 and 4,

$$t_{pp} = S_{21}^{(p)} e^{i\gamma} \tag{5.3a}$$

$$t_{sp} = S_{41}^{(p)} e^{i\gamma} \tag{5.3b}$$

$$t_{ps} = S_{41}^{(s)} e^{i\gamma} \tag{5.3c}$$

$$t_{ss} = S_{21}^{(s)} e^{i\gamma} \tag{5.3d}$$

where γ accounts for phase shifts between the ports during transmission.

With the complex reflection and transmission coefficients readily available, one may find the complete Mueller matrix by equations (2.13a) - (2.13q). While the common factor $e^{i\xi}$ must be included for the estimation of the complex $r_{\alpha\beta}$, it can be neglected for the MM calculation since the MM is an intensity representation. Ellipsometry angles in equations (2.17a) - (2.17c) and the pseudo dielectric function from equation (2.18) may now also be calculated. The COMSOL S-parameters were imported into MATLAB where these quantities were calculated and plotted.

5.1.6 Joule heating

Energy of the incident light dissipated into a material as heat can be found from equation (2.39) and integrating over the volume of the material of interest. COMSOL calculates resistive heating with the integrated function

$$\texttt{ewfd.Qrh} = \frac{1}{2}\sum_i \texttt{realdot}(J_i, E_i) \qquad i = x, y, z \tag{5.4}$$

given in SI units W/m^3, where $\texttt{realdot}(a, b)$ treat the complex numbers a and b as if they were real-valued vectors of length 2 and return their dot product [37]. Equation (5.4) resembles equation (2.38); heat dissipated over a volume $P_{\text{resistive}}$ is found by integrating equation (5.4) over a selected region, for example the gold particles as marked in figures 5.2a-c.

5.1.7 Electric field norm

Integrated in COMSOL is the possibility to plot certain physical quantities as functions of spatial placement in the computational domain, typically presented in cross-sections of the geometry. The electric field norm is one such quantity which is useful to visualize the distribution of the electric field. It is defined as

$$\texttt{ewfd.normE} = \left[\sum_i \texttt{realdot}(E_i, E_i)\right]^{1/2} \qquad i = x, y, z \tag{5.5}$$

and given in SI units $\mathrm{V/m}$. It can in simplified terms be considered the amplitude of the electric field, $E_{\text{norm}} = \sqrt{E_x^2 + E_y^2 + E_z^2}$. We will use the notation E_{norm} when presenting results of equation (5.5), for simplicity.

5.2 Optimization of model

A great amount of effort has been put into finding ways to improve computational performance of the models, in order to reduce memory usage and thus solution time. While FEM is an efficient simulation tool for full wave solutions of highly customizable geometries, 3D models quickly places a high requirement on the computer's hardware, specifically random access memory (RAM) [22]. There are two main reasons for optimizing the COMSOL model; the first one simply being that it's practical not having to wait days or even weeks for a simulation to complete; the other being that a more efficient model leaves the user with the possibility to model more complex structures or define more demanding study steps. In fact, without the measures taken in this section, none of the results presented later in the chapter would be possible to simulate. The thesis work began with a simple model of sample 6[3] with a no mound geometry (flat substrate) or absorbing elements such as PMLs or SBCs, working only for a single azimuthal angle of incidence. COMSOL spent around 3 minutes per wavelength for either TE or TM polarization at this point, while running out of memory when attempting to solve e.g. sample 5A. In comparison, the optimizied model presented here use 10 seconds per wavelength at one incident angle for sample 6, while furthermore including its mound geometry.

5.2.1 Effect of PML implementation

One of the major problems encountered during the development of the model, was its inability to account for the onset of diffracted modes, resulting in nonsensical output for energy regions where Rayleigh anomalies occur. This behaviour was likely due to unwanted numerical reflection of diffracted waves on the port boundaries. Inserting PMLs on the backside of each port as shown in figure 5.3d immediately solved the problem. In figure 5.4 we can see the effect of the PML implementation for sample 6. The model is observed to be working for $E > 4.2$ eV, although the implementation brought with it an artifact seen as a slight oscillation for energies $2.8 - 3.7$ eV. The spectral shift and dampening of the LSPR seen around 2.1 eV is not due to the PML, but is attributed to the dielectric mound. The implementation of PMLs was also found to significantly reduce computational requirements in terms of both memory usage and computation time, which is supported by literature [9] [10]

The height of PML domain is supposedly not a critical factor, as the equations within the PML are scaled with respect to the length of the PML. Dialog with COMSOL support suggested a PML height equal to the wavelength, but seeing as the simulations are calculated for a large spectrum of wavelengths, the height was more or less arbitrarily set to

---

[3] Sample 6 is considered to be the least computationally demanding sample due to its short lattice constants causing a small volume unit cell domain that needs fewer finite elements to discretize compared to the other samples.

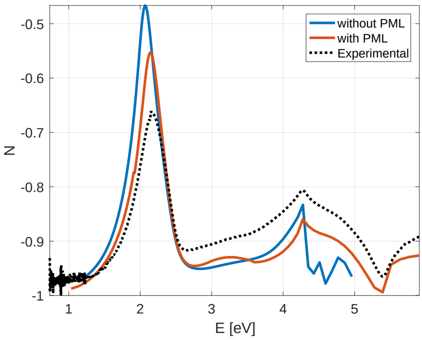

Figure 5.4: Mueller matrix element $N = m_{12}$ of the experimental data (dotted line) of sample 6 at incidence angle $(\theta_0 = 55^\circ, \phi_0 = 0^\circ)$, together with an early version COMSOL model without PML or SiO_2 mound (blue line) and the finalized model with both PML and mound implemented (red line). The latter is also found in figure 5.10.

$h_{\text{PML}} = \lambda_{\text{max}}/3$, as seen in figures 5.5c and 5.5d.

5.2.2 Meshing improvements

Physics dependent mesh

Early models meshed the computational domain indiscriminately, resulting in an extremely fine resolved mesh distributed equally throughout the volume and thus a very large amount of finite elements. Later versions made the mesh dependent on the refractive index. In figure 5.5a one can see that the air domain has slightly coarser mesh than the glass substrate, while the Au particle is even more detailed due to the higher refractive index of gold, but also due to the curvature of the geometry.

At first, models with this element size configuration used the same mesh throughout the simulation. The mesh would then be built with regards to the smallest wavelength, $\text{MES} = \lambda_{\text{min}}/(6n)$, where in most cases $\lambda_{\text{min}} = 210$ nm. The mesh would look like figure 5.5a for all wavelengths, meaning that for the vast majority of iterations the simulation is computed for an unnecessarily detailed mesh. A dynamic meshing system was introduced which rebuilt the mesh every iteration of wavelength, so that longer wavelengths use coarser mesh while still being able to properly resolve the wave. Figure 5.5b exemplifies this for $\lambda = 800$ nm. This implementation has significant impact on computation time, see table 5.1 for the real-time computation of the meshes seen in figure 5.5.

The new setup also included the option of rebuilding the mesh less frequently, which is useful in cases where generating a new mesh every wavelength iteration is computationally demanding and time consuming.

Computation time for each wavelength iteration increases exponentially with decreasing wavelength. This is best shown in the model of GaSb cones, as it is simulated for wavelengths down to 90 nm. Figure 5.6 shows logarithmic plots of calculation time and memory usage as a function of wavelength, as well as the number of elements the mesh consists of at a given wavelength, illustrating how computation time is dependent on the

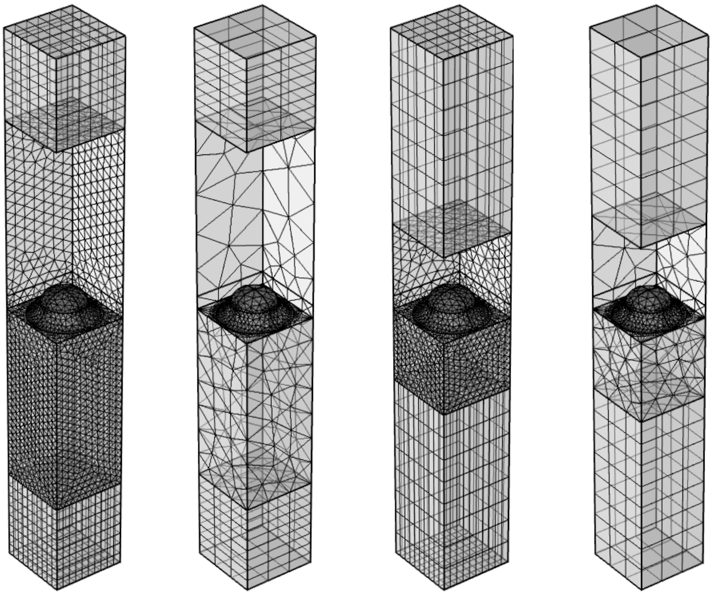

(a) $\lambda = 210$ nm **(b)** $\lambda = 800$ nm **(c)** $\lambda = 210$ nm **(d)** $\lambda = 800$ nm

Figure 5.5: Distribution of mesh elements for different wavelengths and geometry parameters for sample 5A. In (c)-(d) the distance from the top of the gold particle to PML (and, thus, also the port) is reduced to be the same as the lattice constant. Meanwhile, the height of PML region is increased to $h_{\text{PML}} = \lambda_{\text{max}}/3$. Number of mesh elements for each are shown in Table 5.1. Note from inspection that the number of PML elements remain the same from (a) to (c), and from (b) to (d). Outer walls of air domain are hidden for clarity.

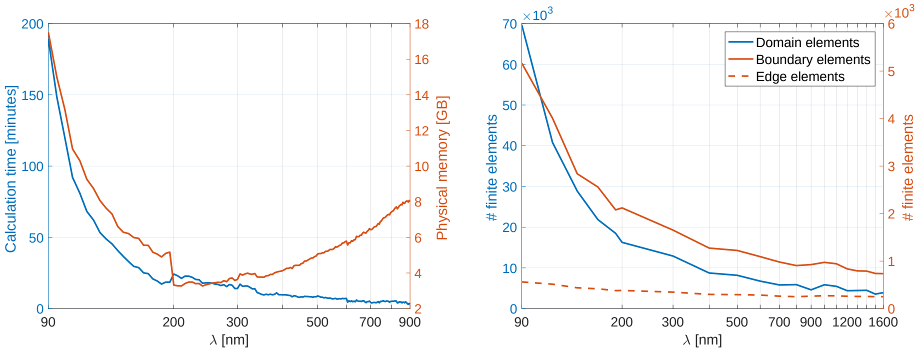

(a) **(b)**

Figure 5.6: Computer performance in calculation of the tilted GaSb cones, where each iteration of wavelength (stepsize 5 nm) includes an auxiliary parametric sweep of azimuthal rotation ϕ_0 valued from 0° to 355° (stepsize 5°). (a) Calculation time (in minutes) as well as amount of physical memory used (unit in gigabytes) at a given wavelength iteration. Incident wave is TE polarized. (b) Number of elements at a given wavelength iteration.

amount of finite elements to solve. Due to the simulation being computationally demanding, it had to be split into smaller segments where each segment (run separately) calculated their own region of wavelength. The sharp changes at 200 nm and 900 nm is where one segment is finished and another begins. This is further explained in section 5.6. In the GaSb cone model, the number of elements seem to stagnate around 700 nm, suggesting that it is unnecessary to further update the mesh beyond this point, as it would not result in fewer elements to solve in order to reduce computation time.

The exponentially decreasing computation time with increasing wavelength seen in figure 5.6 is a trend common for all the samples simulated. It is clear that implementing a physics dependent mesh has an extreme effect on the total computation time for each simulation. With it, the TE simulation for the GaSb cones were completed in 2 days and 2 hours, whereas the same simulation running for a constant mesh configured for the lowest wavelength would take almost 40 days to complete!

Reducing volume of computational domain

Throughout most of the thesis work the height of both air and substrate domains remained a constant $h_{\text{air}} = h_{\text{sub}} = 500$ nm for most simulations as seen in figures 5.5a and 5.5b, so that the distance from the point of reflection to ports were comparable to the wavelength. Reducing the size of this domain without affecting accuracy of results would greatly improve computational performance.

When using domain-backed ports as here[4], the port locations does not matter and should correctly extract the plane-wave component from the field regardless of distance[5]. However, the distance to the PML domains *does* matter. PMLs do not dampen evanescent diffraction orders, so that these must decay before reaching the PML [11] [12]. The decay length of the evanescent waves are given by equation (2.54), and for sub-wavelength nanostructures the criterion for neglecting evanescent wave-coupling with the PMLs becomes $h_{\text{air, sub}} \gg a_{x,y}/(2\pi)$, where $h_{\text{air, sub}}$ is the height of the air or substrate domain defined in figure 5.3e and $a_{x,y} = \max(a_x, a_y)$ is whichever lattice constant is the largest for the sample [30]. A more practical criterion for the minimum distance from reflection point to PML is then

$$h_{\text{air, sub}} > \frac{a_{x,y}}{2}, \tag{5.6}$$

for nanostructures with periodicity smaller than the wavelength [30]. In the thesis COMSOL models, the distance from the base of the Au or GaSb particles ($z = 0$) to the top port ($z = h_{\text{air}}$) was set to

$$h_{\text{air}} = a_{x,y} + R_z \tag{5.7a}$$

for the gold hemispheroidal samples, and

$$h_{\text{air}} = d + h \tag{5.7b}$$

for the tilted GaSb cones. The distance to the bottom port was set equal to h_{air}, except for the GaSb model where it was halved, $h_{\text{sub}} = h_{\text{air}}/2$, due to the absorptive nature of the GaSb substrate.

---

[4] The ports are backed by the PML domains, see figures 5.3a and 5.3d.

[5] Source: private communication with COMSOL support team.

As seen in figure 5.5 and table 5.1, reducing the volume of the physical domain drastically reduce the amount of elements to solve and hence reduces the required amount of RAM and computation time, particularly at lower wavelengths. Without this volume reduction some of the sample results to be presented would not be possible to calculate, considering that certain simulations pushed the limits of the desktop computer even after reducing the computational domain (specifically the GaSb cones),

In conclusion, all the above-mentioned changes to the COMSOL model have greatly decreased the computational cost on memory, and reduced computation time (particularly when computing lower wavelengths). They have furthermore improved accuracy in the results, especially in higher energy regions where diffracted modes occur.

Table 5.1: Performance differences when comparing size of computational volume and wavelengths for sample 5A. Computation time and memory usage is tracked for a single wavelength TE wave at one fixed angle of incidence $\phi_0 = 0°$. Fixed volume: constant height for air and substrate domains $h_{\text{air}} = h_{\text{sub}} = 500$ nm regardless of sample parameters, as well as fixed PML height of half the size of air domain. Reduced volume: height of computational domain is equal equation (5.7a). From left to right, each column correspond to figure 5.5a-d.

	Fixed volume		Reduced volume	
	@ 210 nm	@ 800 nm	@ 210 nm	@ 800 nm
# domain elements	49 587	8 089	28 249	7 741
# boundary elements	6 028	2 197	4 432	2 055
# edge elements	602	356	522	328
Physical memory	9.94 GB	2.13 GB	6.26 GB	1.91 GB
Computation time	71 s	6 s	36s	6 s

5.3 Sample 6

5.3.1 Experimental data

The normalized Mueller matrix of the experimental data can be found in figure 5.7. The elements are plotted as contour polar plots with the radius corresponding to photon energy E and polar angle corresponding to incident azimuthal angle ϕ_0. Below the MM a SEM image of sample 6 is included together with the schematic of a square reciprocal lattice defining ϕ_0 as zero along $\Gamma - X$. A localized surface plasmon resonance is observed for all angles at energy 2.1 eV. There is also a small amount of polarization coupling observed at this energy in the block off-diagonal elements. A stronger conversion between polarizations is observed between the X- and M-point at higher energies. This conversion between s-polarization and p-polarization is also seen for the ellipsometric angles Ψ_{sp} and Ψ_{ps} in figure 5.8. Rayleigh anomalies have been superposed as white and black lines in both figures, which will be more thoroughly explained in the next section.

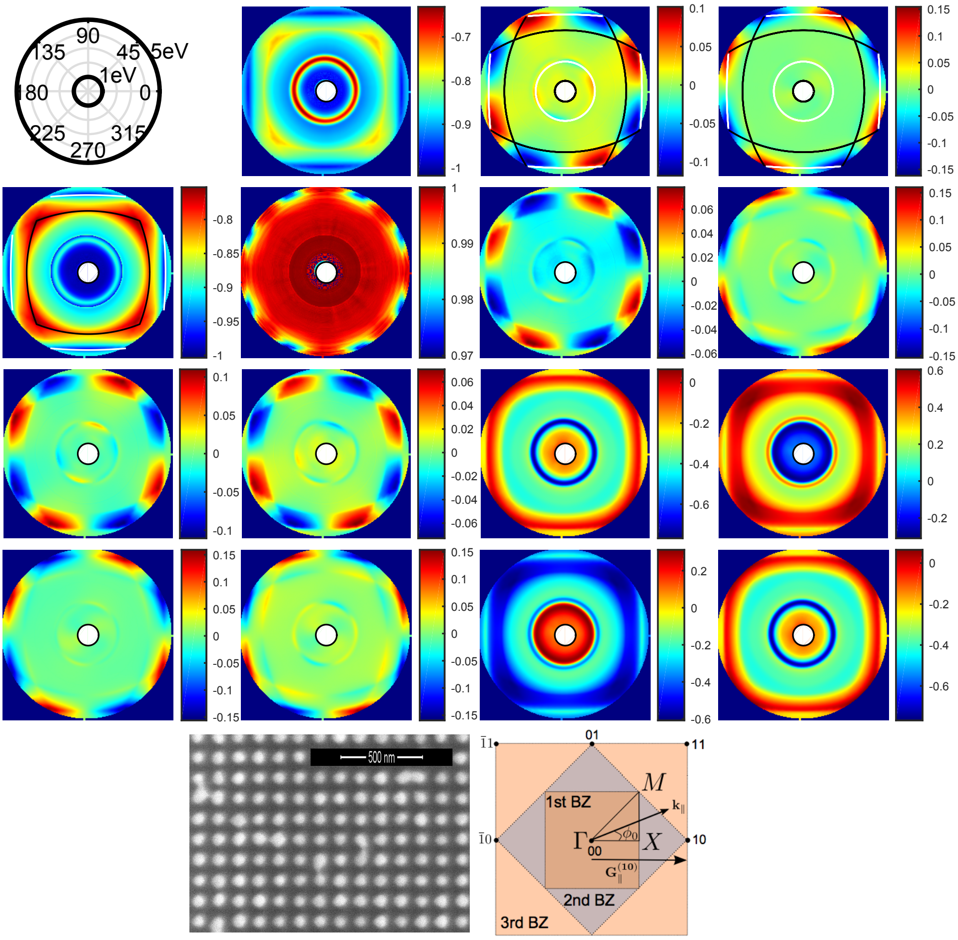

Figure 5.7: The experimental MM of sample 6, where the energy is plotted radially and the rotation angle is the azimuthal angle ϕ_0, and the polar AOI is $\theta_0 = 55°$. Inner circle corresponds to 0.73 eV while outer circle coresopnd to 5.9 eV. Rayleigh lines are superposed in elements m_{21}, m_{13} and m_{14}. The two latter elements have additionally the LSPR highlighted as a white circle at 2.1 eV. A scaling has been applied to m_{21} for improved visibility. Data from [14]. A SEM image of sample 6 next to a schematic of a square reciprocal lattice defining incidence angle ϕ_0 has been included below the MM.

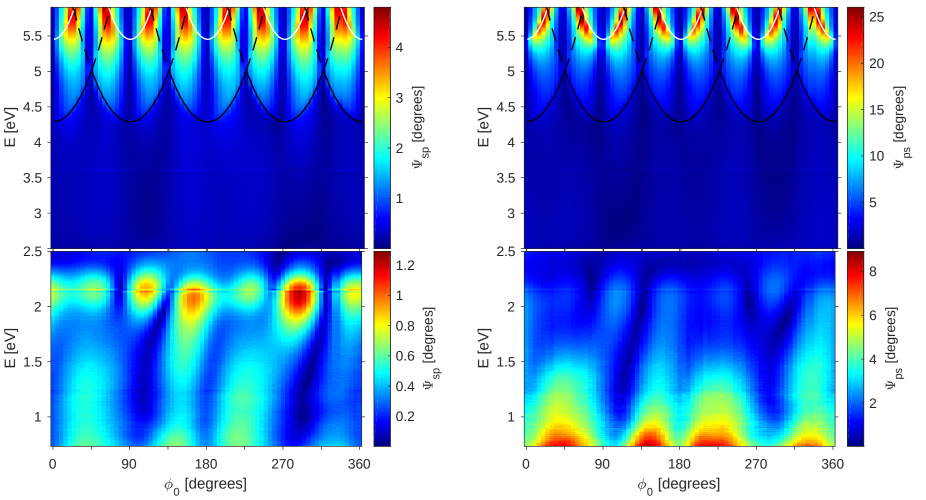

Figure 5.8: Contour plots of Ψ_{sp} (left) and Ψ_{ps} (right) as functions of photon energy and azimuthal angle of the incident light for experimental sample 6, fabricated in [14]. Rayleigh lines are superposed for SiO_2 substrate (black lines) and air (white lines).

5.3.2 COMSOL simulation

Sample 6 was first simulated with a fixed height of the computational domain, similar to figures 5.5a-b. At a polar AOI $\theta_0 = 55°$ for the wavelengths $\lambda = 210 - 1200$ nm and azimuthal AOI $\phi_0 = 0° - 360°$, the total elapsed real-time it took to complete the COMSOL simulation (also known as the *wall time*) was 312 hours and 35 minutes, including both TE and TM simulations, when performed on the desktop computer with hardware as specified in the introduction to this chapter. However, these two were running simultaneously on the same computer, effectively reducing the actual time spent by half. By default, COMSOL uses the total number of available physical CPU cores during calculations. Assuming that the code is well balanced in that each core does approximately the same amount of work, the *CPU time* using COMSOL can be estimated as the wall time multiplied by the number of physical cores. In this case the CPU time becomes 78 days, 3 hours and 30 minutes! At a later stage, the simulations were run again for a reduced height of the computational domain similar to figures 5.5c-d, which reduced the wall time to approximately 82 hours without affecting accuracy of the results. On average, this is about 10 seconds wall time per wavelength per azimuthal angle.

The normalized MM of the COMSOL simulated data can be found in figure 5.9, and can be compared to experimental results in figure 5.7. In figure 5.10 the experimental data is compared to the COMSOL data in terms of the MM elements $N = m_{12}$, $C = m_{33}$, and $S = m_{34}$ for three selected angles. Despite minor numerical differences, the LSPR is observed at the same spectral position, and also the peaks and dips associated with Rayleigh anomalies (discussed below). The COMSOL simulation is found to be in good correspondence with the experimental data. It is interesting, however, to note an additional polarization coupling observed at around 3 eV in elements m_{31} and m_{32} in figure 5.9,

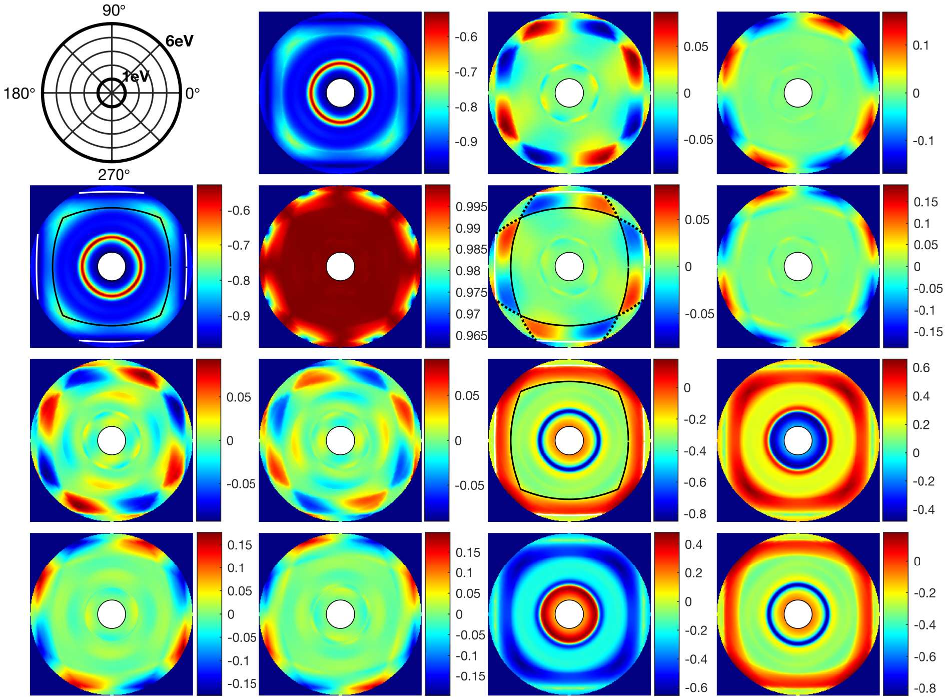

Figure 5.9: Contour plots of MM elements for sample 6 as simulated in COMSOL for $\theta_0 = 55°$, where photon energy E and azimuthal angle ϕ_0 of the incident light corresponds to the radius and angle in each polar plot, respectively. The inner circle of the plots denote the lower limit photon energy of 1.03 eV, while the outer circle corresponds to 5.9 eV. In elements m_{21} and m_{33} the Rayleigh lines for BZ-1 in glass (black line) and air (white line) are shown, while element m_{23} in addition includes the extended Rayleigh line for BZ-1 in glass.

which is not observed in the experimental data. As already seen in figure 5.4, where N of the experimental data is compared to two COMSOL models with and without the dielectric mound, the presence of a dielectric mound beneath the Au particles causes a blueshift and dampening of the plasmon resonance located at 2.1 eV.

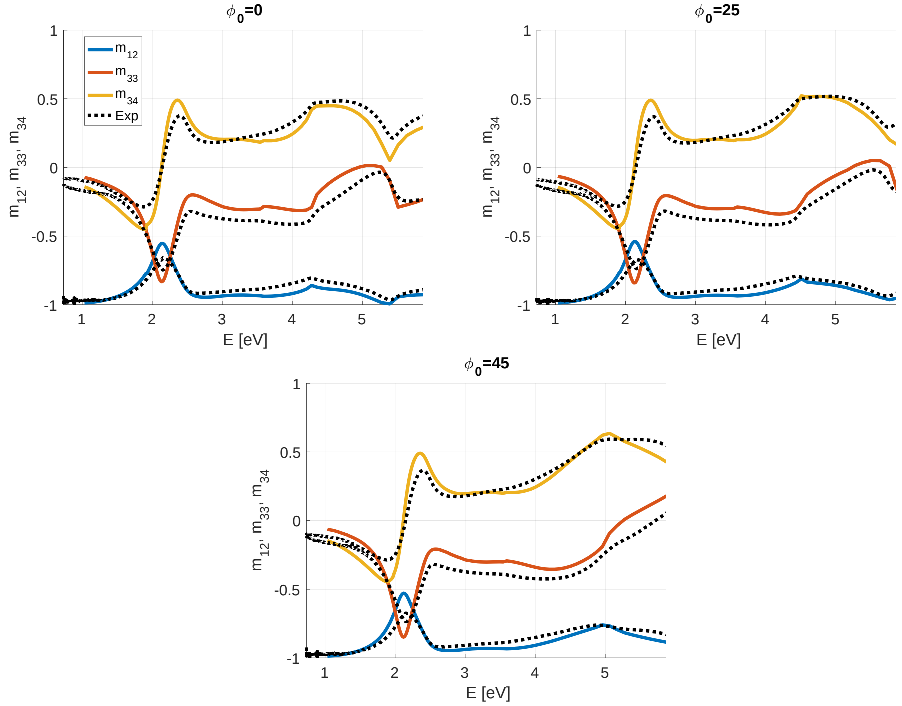

Figure 5.10: Sample 6 comparison between simulation (solid colored lines) and experimental data (black dashed lines) of the MM elements m_{12}, m_{33} and m_{34}.

The expression for the Rayleigh anomaly condition, equation (2.53), is used to find for which wavelength and incidence azimuthal angle a particular diffraction order is propagating along the sample surface. These are superposed in figure 5.9 and hereby referred to as *Rayleigh lines*. The black lines correspond to the onset of the first diffraction mode in substrate (SiO_2) while the white lines similarly correspond to the first diffraction mode in the ambient (air). The dashed lines serves as *extended* Rayleigh lines, which are defined as those lines calculated from equation (2.53) for e.g. $\phi_0 \in [45°, 90°]$ using $\mathbf{G}_{\parallel}^{\bar{1}0}$. The solid lines may be specified as *reduced* Rayleigh lines, if using a corresponding example, they are the solutions of (2.53) in the same interval of azimuthal angles using $\mathbf{G}_{\parallel}^{0\hat{1}}$.

One can observe that the MM is nearly block-diagonal, i.e. the MM is similar to equation (2.19) for non-depolarizing isotropic samples, for photon energies up till about 4 eV. The LSPR is observed as a near-perfect circle around 2.1 eV in all block diagonal elements. Rayleigh lines corresponding to the boundary of the 1st BZ in air (white lines) and substrate (black semi-square) are superposed in MM elements m_{21} and m_{33}. In element m_{23} the extended Rayleigh lines are additionally included. A slight polarization coupling is observed around the LSPR in the off-block-diagonal elements, while a stronger polarization conversion is clearly observed in the regions surrounding the Rayleigh lines of the same elements.

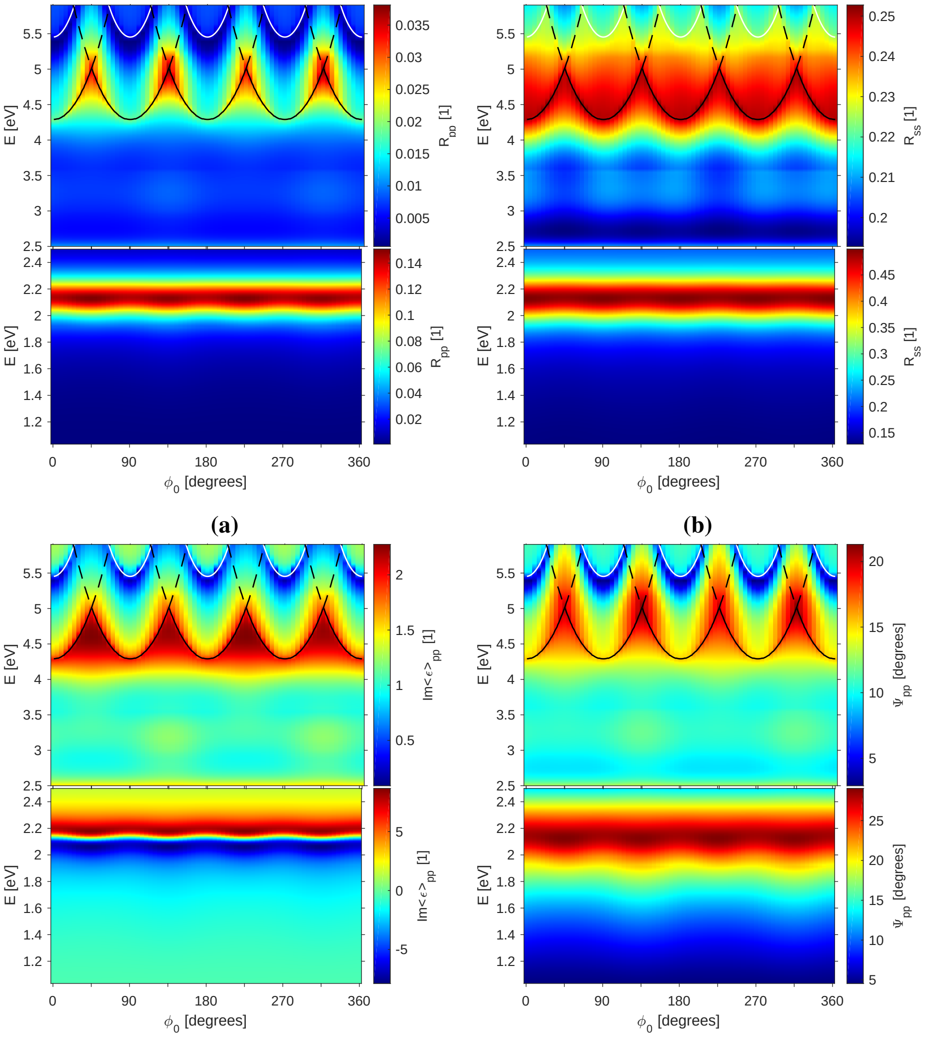

(a) (b) (c) (d)

Figure 5.11: Contour plots of simulated (a) R_{pp} (b) R_{ss} (c) Im$\langle\epsilon_{pp}\rangle$ and (d) Ψ_{pp} as functions of photon energy E and azimuthal angle ψ_0 for sample 6. Rayleigh lines corresponding to the 1st BZ are included as white and black lines for air and substrate, respectively. Extended Rayleigh lines are also included as dashed lines. Due to the strong LSPR around 2.1 eV, separate colorbars are plotted for energies above and below 2.5 eV.

Reflectance coefficients R_{pp} and R_{ss} as functions of photon energy and incident azimuthal angle can be found in figures 5.11a and 5.11b, respectively. The LSPR can be seen at 2.1 eV, fluctuating slightly. In order to better visualize the features weaker than the strong LSPR, a different colorbar is used for energies $E > 2.5$ eV. The optical response at these energies are attributed to the Rayleigh anomalies related to grazing diffracted waves just at the onset of diffracted orders [15]. In figures 5.11d and 5.11c the imaginary part of the pseudo-dielectric function $\mathrm{Im}\langle\epsilon_{pp}\rangle$ and the ellipsometric angle Ψ_{pp} are presented. Note that m_{12} from figure 5.10 and Ψ_{pp} have similar profiles. Rayleigh lines for glass corresponding to 1st BZ are seen to follow peaks in Ψ_{pp}, while for air they follow dips. The same peaks and dips can also be seen in m_{12} of figure 5.10. The Rayleigh lines for glass are observed at peaks in R_{pp} at the M-point, i.e. $\phi_0 = 45°$ in figure 5.11a. In R_{ss}, the extended Rayleigh lines for glass are seen to act as boundaries of a region with medium-sized peaks. It must be emphasized that reflection of p-polarized light R_{pp} is observed to resonate only at the M-point for these energies. This is not immediately clear from ellipsometric data or the MM.

As already seen in figure 5.11 a small dispersion of the LSPR is observed around 2.1 eV. In figure 5.12a the peak value of Ψ_{pp} at the LSPR is plotted as a function of the incident azimuthal angle, together with the wavelength λ_{LSPR} at which Ψ_{pp} is at maximum. Obviously, using a smaller stepsize for the wavelength would smoothen out the latter curve. The peak resonance of the LSPR exhibit a small dependency on the azimuthal angle of incidence. Given the uniformity of sample 6 ($R_x = R_y$ and $a_x = a_y$) one might expect a 45° symmetry, i.e. a folding can be done of the results at this angle. The figures of R_{pp} and R_{ss} seem to confirm this, however, there can be observed small anomalies to this symmetry in the LSPR when comparing the azimuthal angles 45° and 135° in figure 5.12. On the other hand, the numerical difference of the two peaks might be small enough to be dismissed as numerical errors during the calculation. There is also a curious antisymmetry observed at energies $E > 4.5$ eV for R_{ps} in figure 5.13, whereas R_{sp} withholds the 45° symmetry. Regrettably, due to a glitched nonphysical behaviour at lower energies for R_{sp}, one might question the validity of the accuracy of the TE simlation for all energies. Furthermore, this antisymmetry is not observed for experimental Ψ_{ps} in figure 5.8.

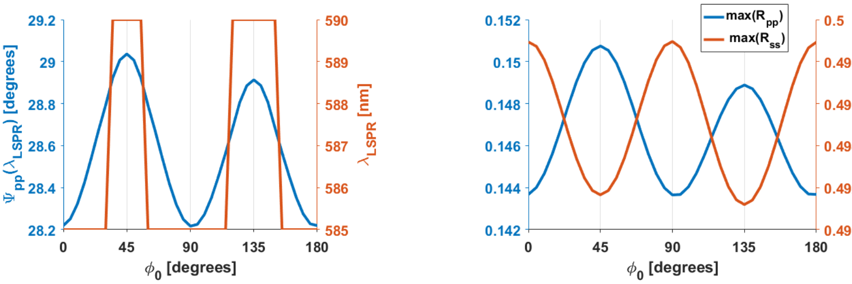

(a) (b)

Figure 5.12: (a) Peak values of Ψ_{pp} for sample 6 at LSPR wavelengths λ_{LSPR}, plotted together with the wavelength at which the plasmon resonance peaks for a given ϕ_0; (b) Azimuthal angle dependency of reflectances for p-polarized and s-polarized light R_{pp} and R_{ss}, respectively, at plasmon resonance wavelengths shown in (a).

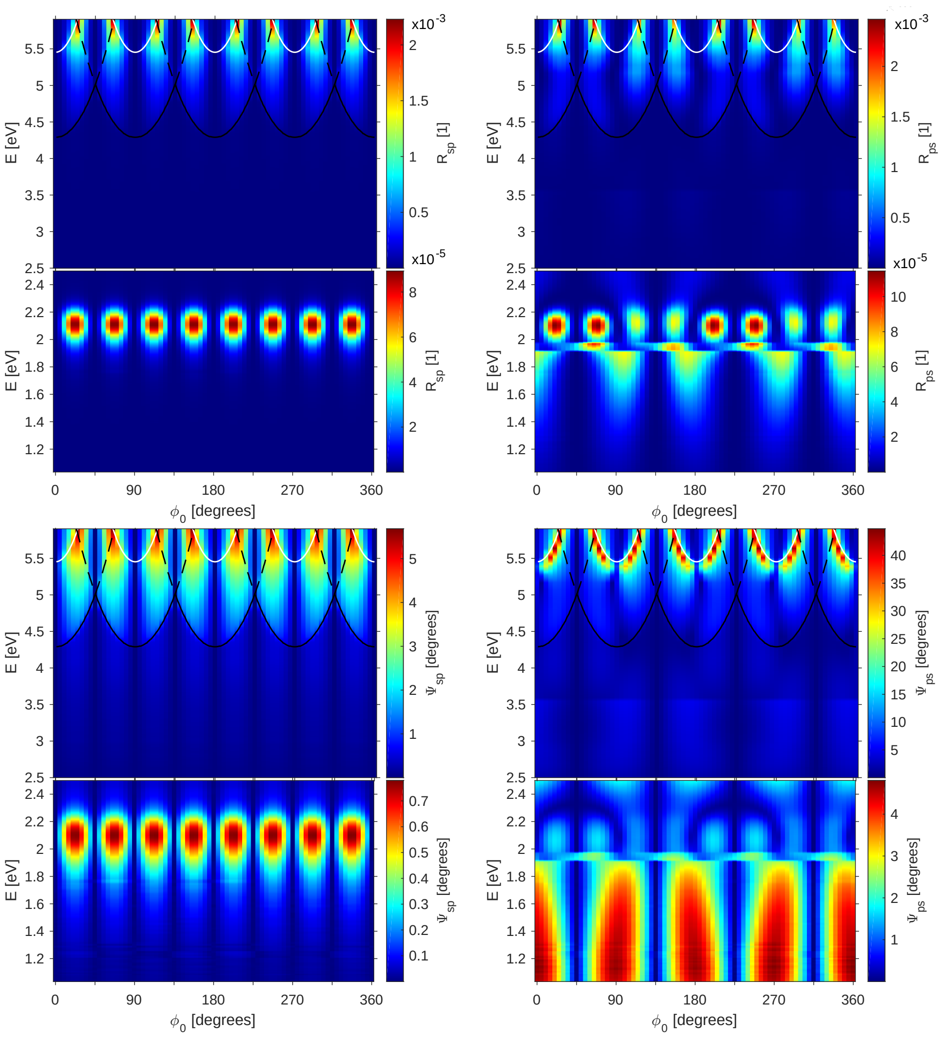

(a) **(b)**

Figure 5.13: Contour plots of (a) R_{sp} (b) R_{ps} (c) Ψ_{sp} and (d) Ψ_{ps} for sample 6. For reasons of clarity, separate colorbars are implemented for energies $E > 2.5$ eV.

The polarization coupling observed in the MM is more visible in the contour plots of R_{sp}, R_{ps}, Ψ_{sp} and Ψ_{ps} found in figure 5.13. The aforementioned artifact observed in R_{ps} (and thus Ψ_{ps}) is seen to besmirch the data for $E < 2.5$ eV. Similar behaviour is not observed in the results of the other samples and is therefore considered to be an error specifically in the TE simulation of sample 6, although the exact cause is unknown.

Assuming the simulated R_{ps} is accurate to a certain extent for energies above the glitch, we note that $R_{ps} \approx R_{sp}$ yet Ψ_{ps} is overall different from Ψ_{sp}. This is because the ellipsometric amplitude angles are defined with different denominators, $\Psi_{ps} =$

$\arctan|r_{ps}/r_{pp}|$ and $\Psi_{sp} = \arctan|r_{sp}/r_{ss}|$, see equation (2.15). With this in mind, comparing the experimental and simulated polarization coupling shown in figures 5.8 and 5.13, respectively, suggests an approximately equal conversion between both polarizations of the reflected light for the experimental sample as well, i.e. $R_{sp} \approx R_{ps}$, for energies $E > 2.5$ eV.

The sample is observed to be pseudo-isotropic along the X- and M- points, i.e. $\phi_0 = 0°, 45°$, while conveying polarization conversion which resonates at $\phi_0 = 22.5°$ around the LSPR energy and at the meeting point between the extended Rayleigh line for glass and reduced Rayleigh line for air. The strongest polarization coupling is observed to be confined between the two Rayleigh lines. The miniscule polarization conversion around 2.1 eV in Ψ_{sp} (and R_{sp}) is much more well-defined than the experimental counterpart in figure 5.8, where noise effects may make an appearance.

Figures 5.14 and 5.15 visualize the electric field norm E_{norm} in the 3D space surrounding the Au particle and mound area. Red isosurface correspond to the strongest field (barely visible) while dark blue is weaker. The LSPR is seen to be dipolar in nature and strongly concentrated along the bottom edge of the gold particle.

Resistive heating has been calculated from equation (5.4) and integrated over the Au particle volume of sample 6. Figure 5.16 shows a contour plot of heat dissipation $P_{\text{resistive}}$ into the gold particle as a function of the energy E and azimuthal angle ϕ_0 of the incident light. The reader is reminded that the incident electric field has amplitude 1 V/m. For energies below 2.5 eV the heat loss is uniform for all azimuthal angles. It is observed that peaks in $P_{\text{resistive}}$ follow Rayleigh lines of the substrate, while Rayleigh lines of the ambient air are recognized by dips in $P_{\text{resistive}}$. In other words, the sample suffer from increased heat losses at the Rayleigh lines.

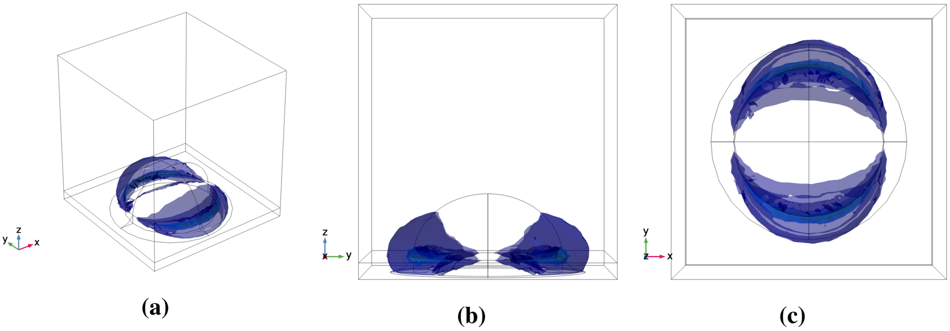

(a) (b) (c)

Figure 5.14: The electric field norm E_{norm} plotted for five layers of isosurface when incident wave is TE polarized at wavelength $\lambda_{\text{LSPR}} = 585$ nm and azimuthal angle $\phi_0 = 0°$, i.e. propagating along $\hat{x}$-direction at polar incidence $\theta_0 = 55°$. (a) General view (b) $\hat{x}$ is pointing out of paper (c) $\hat{z}$ is pointing out of paper.

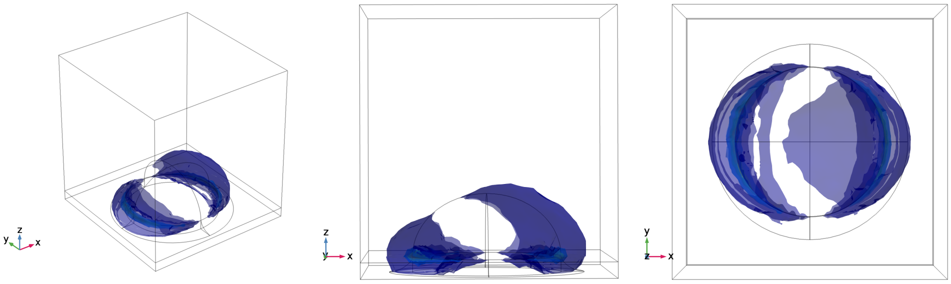

(a) **(b)** **(c)**

Figure 5.15: The electric field norm E_{norm} plotted for five layers of isosurface when incident wave is TM polarized at wavelength $\lambda_{\text{LSPR}} = 585$ nm and azimuthal angle $\phi_0 = 0^\circ$, i.e. propagating along $\hat{x}$-direction at polar incidence $\theta_0 = 55^\circ$. (a) General view (b) $\hat{y}$ is pointing into the paper (c) $\hat{z}$ is pointing out of paper.

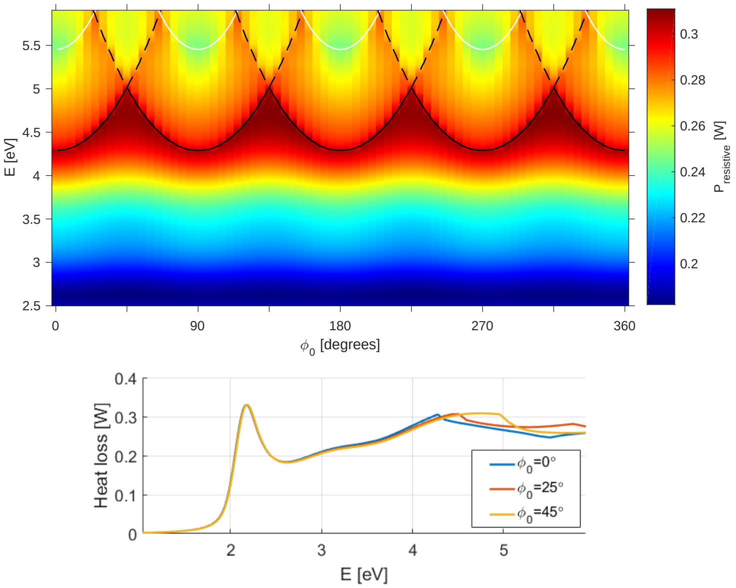

Figure 5.16: Top: Contour plot of $P_{\text{resistive}}$, resistive heat loss over the volume of the gold particles in sample 6, with respect to photon energy and azimuthal angle of the incident light. Rayleigh lines corresponding to the 1st BZ in air (white lines) and glass substrate (black lines) have been superimposed. Bottom: Same plot but the full energy spectrum for a few chosen values of ϕ_0, illustrating isotropic behaviour below 2.5 eV.

5.4 Sample 5A

5.4.1 Experimental data

The normalized MM elements of the experimental data [14] is found in figure 5.17, while a SEM image of sample 5A next to a conceptual sketch of its reciprocal lattice is found in figure 5.18. The MM reveal a rich optical response [15]. A plasmon resonance is observed around 2.1 eV with associated polarization coupling in the block off-diagonal elements. The response for energies above the LSPR is observed to follow the Rayleigh lines for both air and SiO_2 substrate.

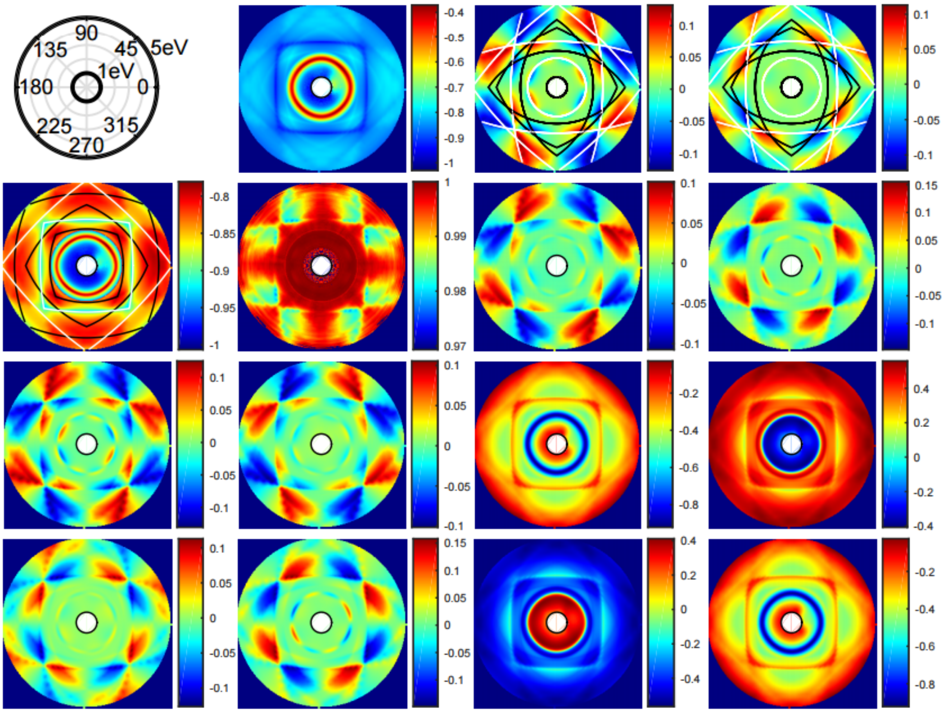

Figure 5.17: Contour plots of the elements of the *experimental* normalized Mueller matrix for sample 5A with incident polar angle $\theta_0 = 55°$, as found in [15]. The inner circle of each element corresponds to 0.73 eV while the outer corresponds to 5.90 eV. In element m_{21}, the Rayleigh lines corresponding to 1st BZ and 2nd BZ in air (white lines) and glass substrate (black lines) have been superimposed. In elements m_{13} and m_{14} the extended Rayleigh lines are additionally superimposed, together with a white circle at around 2.1 eV highlighting the LSPR resonance. A scaling has been applied for elements m_{21} and m_{22} for energies below 2.5 eV; in this range $m_{2j} = \mathrm{sgn}(m_{2j})|m_{2j}|^{1/4}$, where $j = 1, 2$.

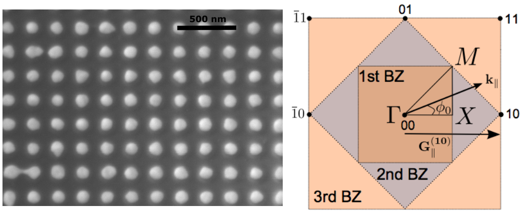

Figure 5.18: SEM image of sample 5A next to a sketch of the reciprocal lattice.

5.4.2 COMSOL simulation

Due to the symmetry of the sample (see table 3.1), it was deemed sufficient to simulate only for the first half of the azimuthal angles, then mirroring the results to gain the full rotational optical response. The total wall time, including both TE and TM simulations, each running for wavelengths $\lambda = 210 - 1600$ nm with stepsize $\Delta\lambda = 5$ nm and an auxiliary sweep of incident azimuthal angles $\phi_0 = 0° - 180°$ with stepsize $\Delta\phi = 5°$, was 38 hours and 50 minutes. In practice the actual simulation run-time is halved as both TE and TM simulations were running simultaneously. The approximate CPU time is 9 days and 17 hours when assuming the workload was at all times evenly distributed among the six CPU cores. Each of the two simulations used at most around 9.5 GB RAM during the calculation, and spent 23 minutes solving $\lambda = 210$ nm for all the incident angles whereas $\lambda = 1600$ nm for all angles was completed in 1 min 40 seconds, which corresponds to 37 seconds and 3 seconds per wavelength per azimuthal angle, respectively.

The reflectances R_{ss} and R_{pp} from both TE and TM simulations with respect to the energy and azimuthal angle of the incident beam can be found in figures 5.19a-b. One immediately observes patterns forming in the higher energy region as well as a strong LSPR resonance around 2 eV. Ellipsometric angle Ψ_{pp} and the imaginary part of the pseudo dielectric function, $\mathrm{Im}\langle\epsilon\rangle_{pp}$, are presented in figures 5.19c-d. Here, Rayleigh lines have been superposed revealing an optical response highly dependent on the diffracted modes along the surface. The very same Rayleigh lines can be observed in the reflectances in figures 5.19a-b without the aid of the drawn lines. The Rayleigh lines correspond to the 1st and the 2nd BZ in air (white lines) and substrate (black lines), as well as the 3rd BZ in substrate (top black solid line). These lines are also overlaid in the contour plots of R_{sp}, R_{ps}, Ψ_{sp} and Ψ_{ps} in figure 5.25, and in the normalized MM in figure 5.21.

The LSPR is seen to fluctuate with respect to the incident azimuthal angle, which is further investigated in figure 5.20. In figure 5.20a, where the resonance is represented by Ψ_{pp}, we see that the wavelength at which the LSPR is located (λ_{LSPR}) is also shifted as the amplitude of the resonance fluctuates. Here we are reminded that the jagged lines are due to the relatively large stepsize of wavelength when inspecting such a narrow region. On average, the LSPR is located at $\lambda_{\text{LSPR}} = 625$ nm. Compared to the average LSPR position of the experimental sample, $\lambda_{\text{LSPR}}^{(\text{exp})} = 608$ nm, it might suggest that the sample parameters used in COMSOL are not entirely accurate. It is clear from these figures that sample 5A does not hold a perfect 45 degree symmetry, or even a 90 degree symmetry. Why this is, will be discussed in section 5.4.4.

The main features of the optical response for photon energies above the LSPR can be

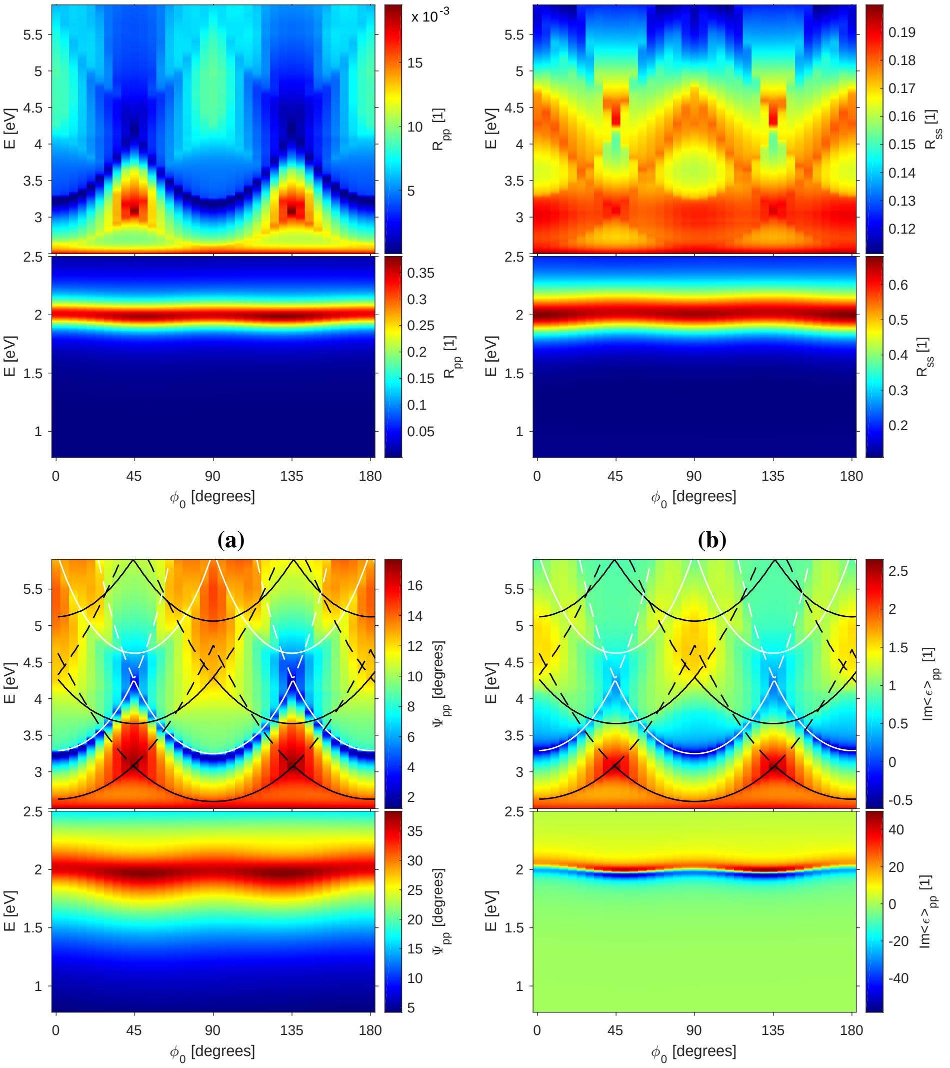

(a) **(b)**

(c) **(d)**

Figure 5.19: Simulation results of sample 5A represented by contour plots of (a) R_{pp} (b) R_{ss} (c) Ψ_{pp} and (d) $\mathrm{Im}\langle\epsilon\rangle_{pp}$, as functions of energy E and azimuthal angle ϕ_0 of the incident beam. Due to the strong LSP resonance around 2 eV, all plots have independent colorbars for energies above and below 2.5 eV. In (c)-(d), Rayleigh lines for air (white) and substrate (black) are superposed, including the extended Rayleigh lines (dashed lines). Sorted by increasing energy, the solid Rayleigh lines correspond to BZ-1 (SiO_2), BZ-1 (air), BZ-2 (SiO_2), BZ-2 (air) and BZ-3 (SiO_2).

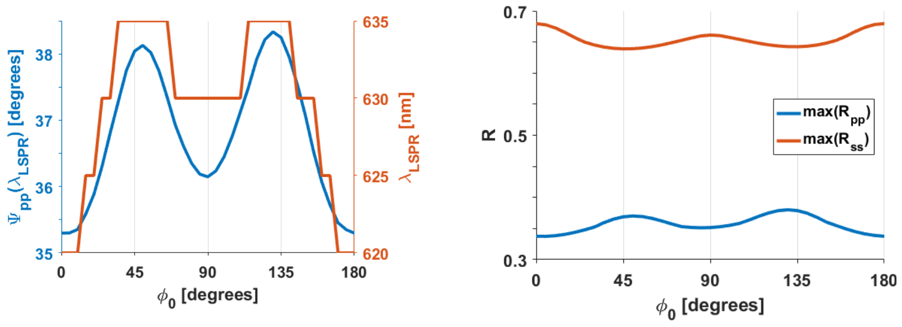

(a)

(b)

Figure 5.20: (a) Peak values of Ψ_{pp} at LSPR wavelengths λ_{LSPR} for sample 5A, plotted together with the wavelength at which the plasmon resonance peaks for a given ϕ_0; (b) Azimuthal angle dependency of reflectances for p-polarized and s-polarized light R_{pp} and R_{ss}, respectively, at plasmon resonance wavelengths shown in (a).

described by estimating the Rayleigh line. Boundaries of 1st and 2nd BZ in air are clearly visible in the block-diagonal elements of the MM contour plot in figure 5.21. For example, in the $m_{12} = m_{21}$ elements they are seen as sharp dips. Seeing as the MM to a certain extent follows the block-diagonal form of equation (2.19), one can assume to observe a similar dip in Ψ_{pp}, as is shown in figure 5.23. The strong dips in R_{pp} for BZ-1 in air tells us that mainly p-polarized light is coupled into the grazing diffracted mode, as the reflected light contains a reduced amount of p-polarized light at this Rayleigh line. In contrast, the peaks in R_{pp} at BZ-1 in the SiO_2 substrate shows an enhanced reflection of p-reflectance of the reflected beam at the Rayleigh line condition.

The normalized MM of the experimental and simulated data can be found in figures 5.17 and 5.21, respectively, and comparisons between experimental and COMSOL data of MM elements m_{12}, m_{33} and m_{34} at three specific azimuthal angles are found in figure 5.22. The COMSOL model is found to be highly accurate in the LSPR region, and a good qualitative correspondence with higher energies. Note, however, that the off-block-diagonal elements have overall larger values in the simulated MM compared to the experimental MM, which suggest a stronger structure-induced anisotropy in the COMSOL model. This implies that the modeled dielectric mound is not quite true to its experimental counterpart, differing in shape or size or both, in which case would suggest that the estimated height profile is not as accurate as we thought. It is observed that the block-diagonal MM approach of equation (2.19) can safely be assumed at angles $\phi_0 = 0°, 90°$ as polarization coupling only appears at other angles.

In figures 5.23 and 5.24, Ψ_{pp} and $\text{Im}\langle\epsilon\rangle_{pp}$ for angles $\phi_0 = 0° - 45°$ are stacked on top of each other for COMSOL and experimental data, respectively. Rayleigh lines are hand drawn into the plots, as well as the LSPR which shows a slight dispersion with respect to ϕ_0 for both experimental and simulated results. Due to the transparency of the substrate, grazing diffracted beams inside the glass substrate are also observed. Enhanced peaks of 1st BZ of SiO2 substrate at the M point, i.e. $\phi_0 = 45°$, for energies around $E^{sub}_{BZ-1} = 3.1$

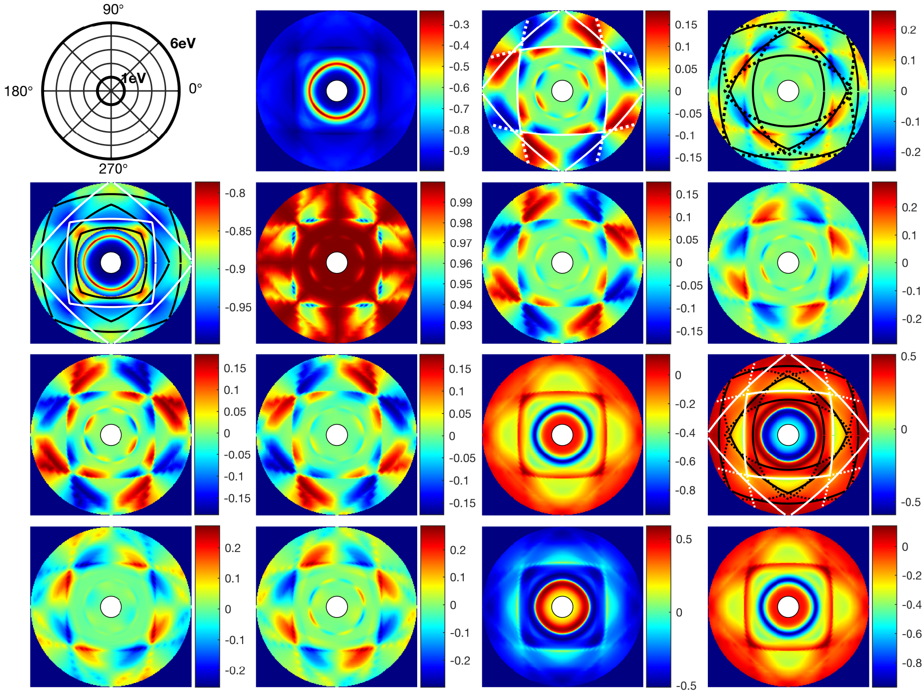

Figure 5.21: Contour plots of MM elements of sample 5A simulated in COMSOL with respect to photon energy E and azimuthal angle ϕ_0 of the incident light. Rayleigh lines are shown for both air (white lines) and glass substrate (black lines). Extended Rayleigh lines are included as dotted lines in elements m_{13}, m_{14} and m_{34}. In m_{21}, reduced Rayleigh lines (i.e. boundaries of BZ) are superposed for the 1st BZ (innermost semi-square) and the 2nd BZ (tilted semi-square) can be seen for both air and substrate, as well as the 3rd BZ for SiO$_2$ (outermost black semi-square). The LSPR resonance can be seen as circles around 2 eV. In order to more clearly observe nuances in m_{21} for higher energies, a scaling has been applied for $E < 2.5$ eV, in this region $|m_{12}|^{1/6}\text{sign}(m_{21})$ where sign() indicates the signum function. The innermost thick-lined circle in the schematic, replacing the trivial m_{11} element, corresponds to 0.78 eV while the outer circle corresponds to 5.9 eV.

eV. The same peak in the experimental data is found at 3.08 eV [15]. A weaker, but broader peak is visible at the X point for the glass Rayleigh line at $E^{\text{SiO}_2}_{BZ-2} = 4.28$ eV, or at 4.15 eV in the experimental data. These peaks are visible in figures 5.23 and 5.24, but also in the contour plots in figures 5.19 and 5.21 when inspecting the 1st and 2nd Rayleigh lines for the substrate at azimuthal angles $\phi_0 = 45°, 0°$, respectively.

The polarization coupling of the reflected light observed in figure 5.25 and in the block off-diagonal elements of the MM in figure 5.21 is seen to be strongly dependent on the Rayleigh lines in air. Looking at R_{pp} and R_{ss} in particular, peaks of conversion are observed along the reduced Rayleigh line for BZ-1 in air in the region surrounding the M-point, while no conversion is observed at exactly $\phi_0 = 45°$. There is also noted an equal amount of conversion between both polarizations. Strong polarization conversion is

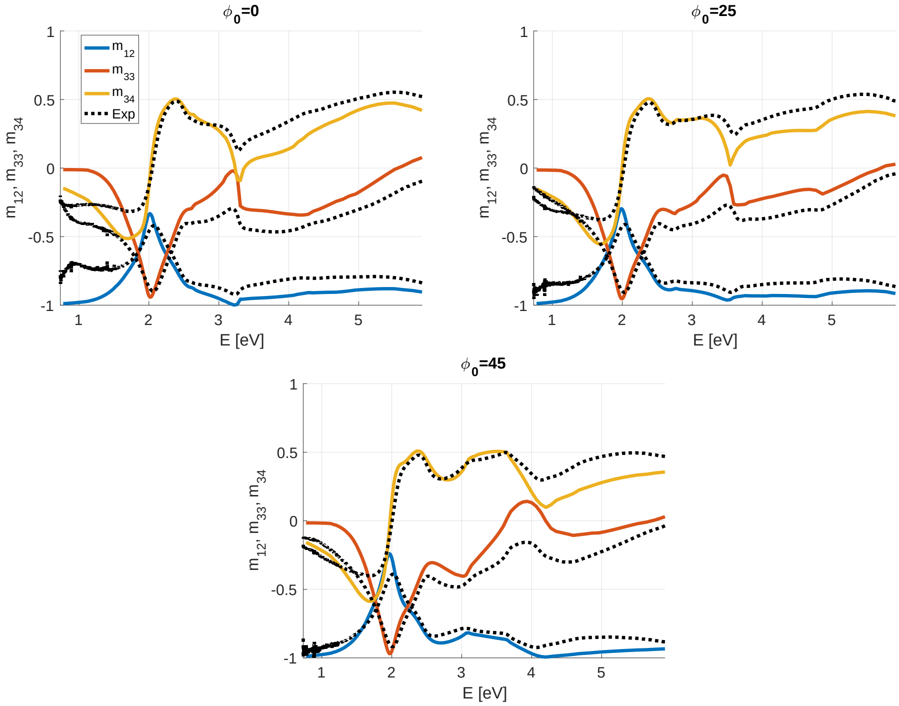

Figure 5.22: Normalized MM elements m_{12}, m_{33} and m_{34} compared with experimental data for sample 5A.

also found around the LSPR energy, as already mentioned, observed at azimuthal angles $\phi_0 = 22.5°, 67.5°$ etc. It is clear from observing the varying degree of coupling strength at these conversion resonances in figure 5.25 that the sample has a $90°$ symmetry.

Joule heating in terms of $P_{\text{resistive}}$ integrated over the Au particle volume is found in figure 5.26. Heat dissipation is found to be uniform up until about 2.5 eV, where it becomes highly influenced by the Rayleigh lines.

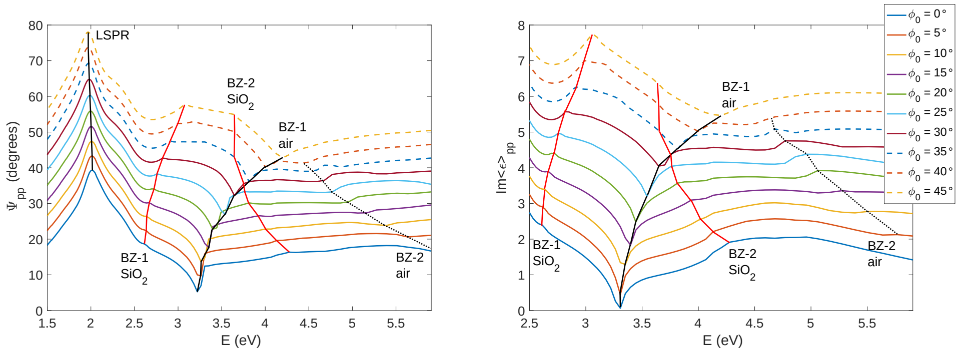

Figure 5.23: Ψ_{pp} (left) and Im$\langle\epsilon_{pp}\rangle$ (right) for COMSOL simulated sample 5A for azimuthal angles $\phi_0 = 0° - 45°$ in steps of $\Delta\phi_0 = 5°$. Approximate Rayleigh lines are hand drawn in both figures. A slight dispersion of the LSPR can be seen around 2 eV. For reasons of clarity, Ψ_{pp} plots are offset by $4°\kappa$ and Im$\langle\epsilon_{pp}\rangle$ by 0.52κ, where $\kappa = \phi_0/\Delta\phi_0$.

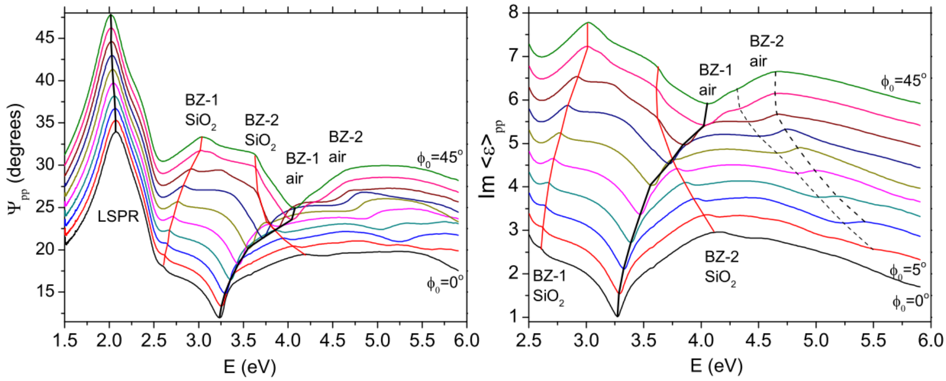

Figure 5.24: Experimental data of sample 5A of Ψ_{pp} and Im$\langle\epsilon_{pp}\rangle$ for azimuthal angles of incidence from $\phi_0 = 0°$ to $\phi_0 = 45°$ in steps of $\Delta\phi_0 = 5°$, as found in [15]. Three approximate Rayleigh lines are hand drawn, while the location of BZ-2 in air is more unclear. Ψ_{pp}-curves are offset by $1.4°\kappa$ and the Im$\langle\epsilon_{pp}\rangle$-curves by 0.2κ, where $\kappa = \phi_0/\Delta\phi_0$.

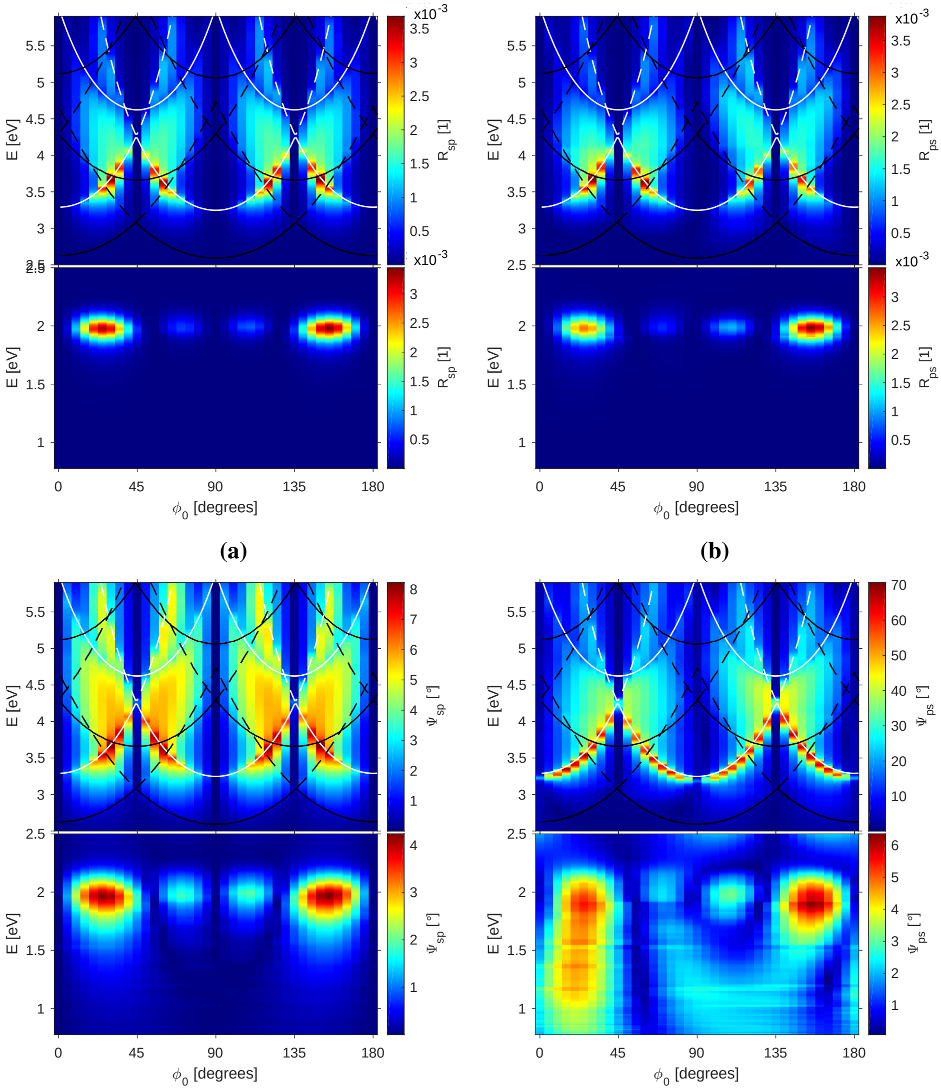

(a) **(b)** **(c)** **(d)**

Figure 5.25: Contour plots of (a) R_{sp} (b) R_{ps} (c) Ψ_{sp} and (d) Ψ_{ps} for sample 5A. Rayleigh lines for air (white) and substrate (black) are shown in the same manner as figures 5.19c-d.

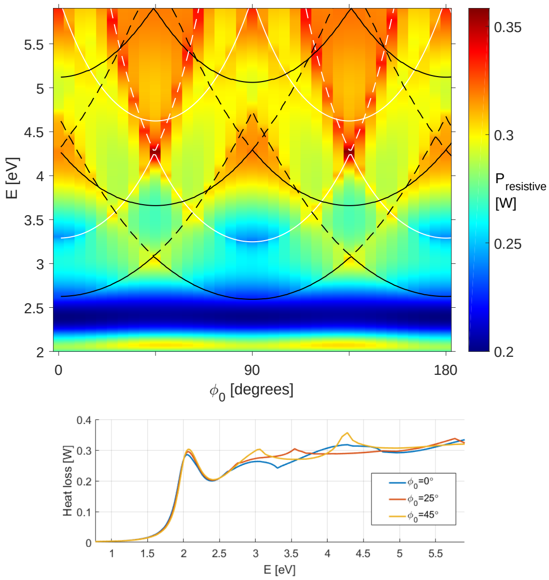

Figure 5.26: Top: Contour plot of resistive heat loss in units Watts over the volume of the gold particles in sample 5A, with respect to photon energy and azimuthal angle of the incident light. Rayleigh lines are indicated by solid (reduced) and dashed (extended) lines for air (white) and substrate (black). Bottom: Same plot but with the full energy spectrum for a few chosen values of ϕ_0.

5.4.3 Field distribution

This section is mainly focused on showcasing COMSOL's capability to visualize the full wave field amplitude inside the computational domain. The electric field norm E_{norm} is presented here at certain wavelengths and azimuthal angles of incidence, see equation (5.5).

In figure 5.27 the 3D field distribution of the LSPR resonance at 2 eV is visualized as a set of isosurfaces, each layer representing an increasing field strength; dark blue is a relatively weak field while the red isosurface (barely visible along the particle edge) show the maximum field amplitude at this wavelength and incident angle. Figure 5.28 attemps to show the evolution of the LSPR as a function of wavelength, as it plots E_{norm} for wavelengths surrounding the LSPR at $\phi_0 = 0°$ at a cross-section in the xy-plane located in the middle between the base of the Au particle ($z = 0$) and the bottom of the mound ($z = -t$). As in sample 6, the LSPR is seen to be strongly concentrated around the rim of base of the Au particle at $z = 0$. The response is observed to be mainly dipolar. This may be applicable to detecting whether molecules that are sensitive to the plasmon resonance are located next to the particles or on top of them.

Figure 5.29 attempts to show the field distribution in a short wavelength spectrum where $\phi_0 = 25°$, a region that has shown to exhibit polarization conversion. The motivation was to try to further understand the origin of the polarization coupling phenomenon observed both around the LSPR and around the Rayleigh lines, through direct inspection of the field distribution. Figure 5.30 shows plots of E_{norm} in the xy-plane at $z = 0$ for different azimuthal angles ϕ_0 at a wavelength of relatively large polarization coupling, $\lambda = 350$ nm (or 3.54 eV). Observe that the field distribution is symmetric with respect to the plane of incidence at angles of no polarization coupling $\phi_0 = 0°, 45°, 90°$, but that is not the case for $\phi_0 = 25°, 65°$.

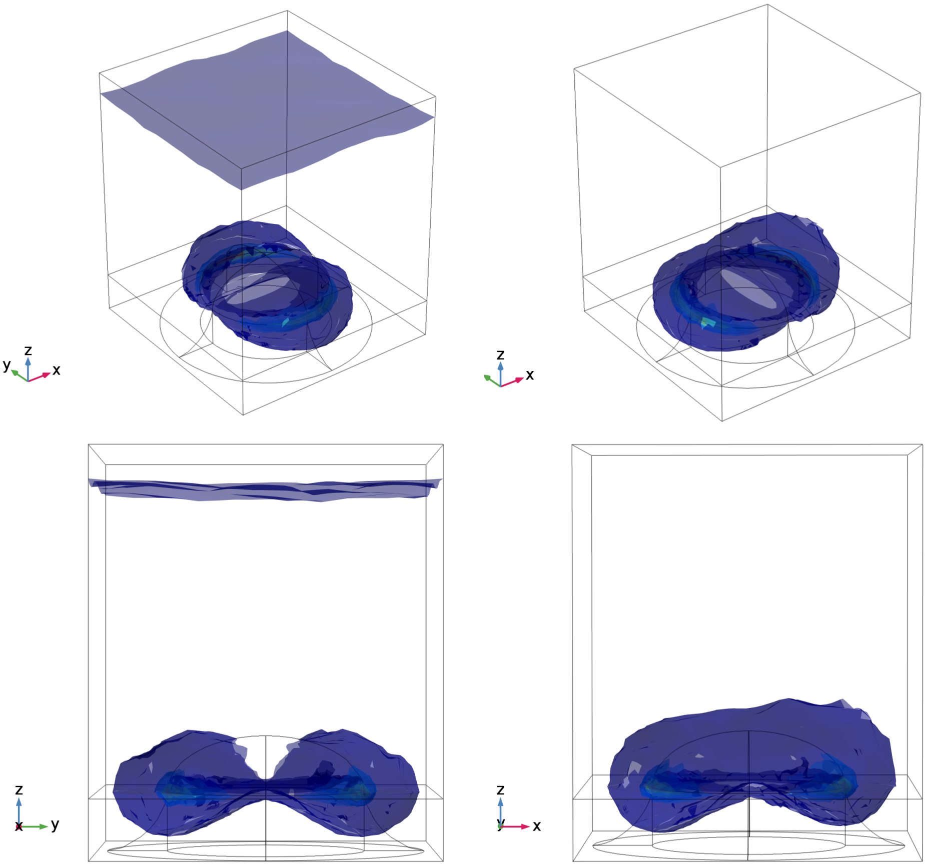

(a) TE **(b)** TM

Figure 5.27: The electric field norm E_{norm} plotted for five layers of isosurface when incident wave is (a) TE polarized and (b) TM polarized at wavelength $\lambda_{\text{LSPR}} = 620$ nm and azimuthal angle $\phi_0 = 0°$, i.e. propagating along $\hat{x}$-direction at polar incidence $\theta_0 = 55°$. Two viewpoints of each plot is given: a general view for both (top), $\hat{x}$ is pointing out of paper for TE (bottom left), and $\hat{y}$ is pointing into paper for TM (bottom right).

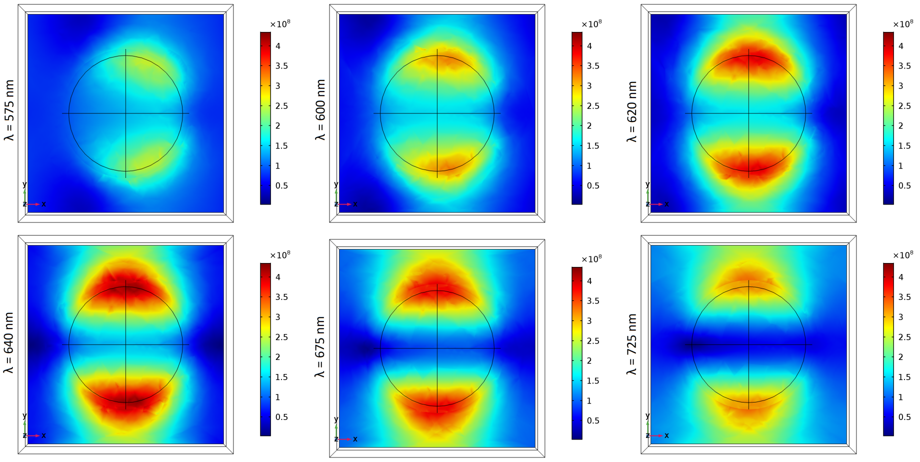

(a) TE

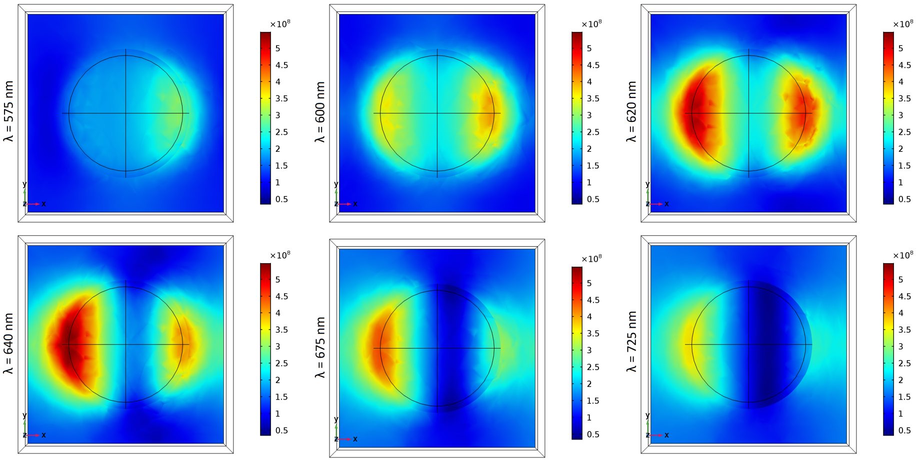

(b) TM

Figure 5.28: Electric field norm E_{norm} at increasing wavelengths between 575-725 nm distributed over sample 5A at a cross-section in xy-plane located at $z = -t/2$, as seen from the top of air domain and down towards the gold particle and substrate. The inner black circle marks the edges of the particle at $z = 0$, while the outer border-less circle indicate the mound cut right at the middle of its height. (a) shows the electric field norm when the incident light is TE polarized with azimuthal angle $\phi_0 = 0^\circ$, i.e. beam incident in +x-direction. Similar in (b) for TM-polarization. For both figures, from top left to bottom right in (a) and (b), the electric field distribution is shown subsequentially for wavelengths $\lambda_0 = 575\text{nm}, 600\text{nm}, 620\text{nm}, 640\text{nm}, 675\text{nm}, 725\text{nm}$. Axis directions are marked in the bottom left corner of each sub-figure. The colorbar marks the values for E_{norm} in units V/m.

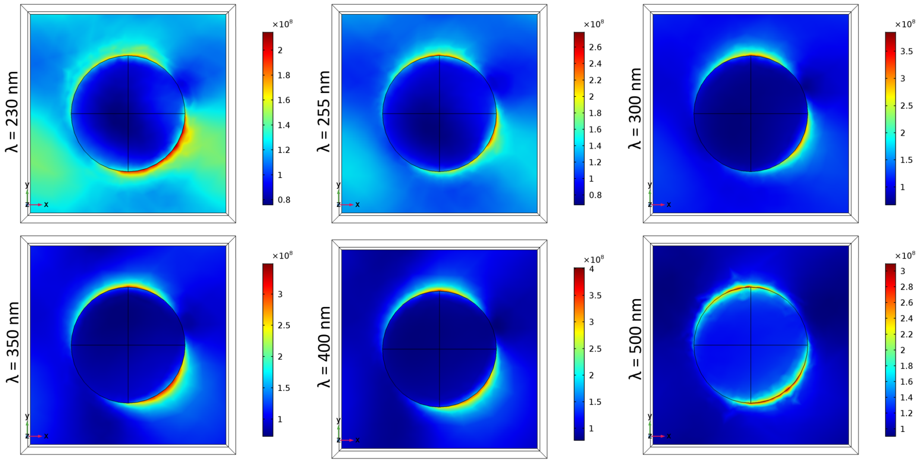

(a) TE

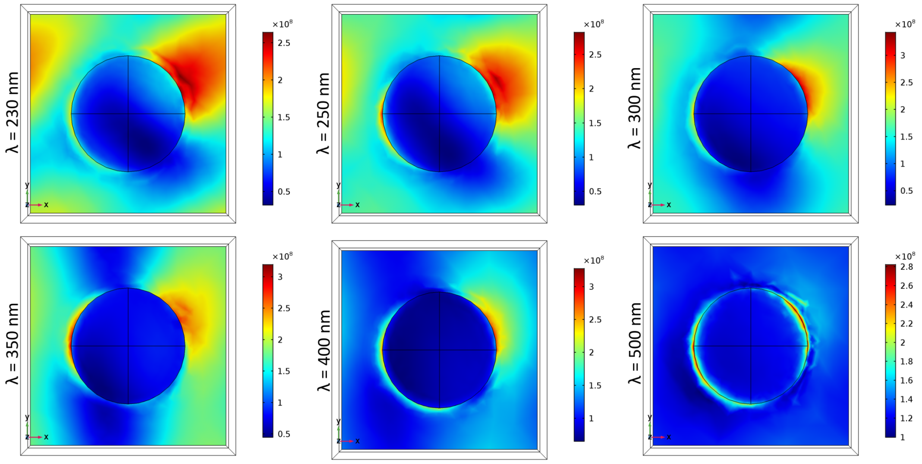

(b) TM

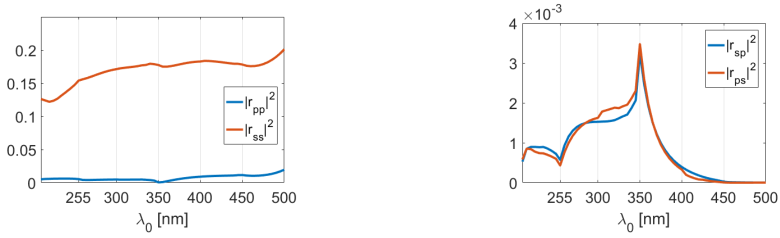

Figure 5.29: Electric field norm distribution of sample 5A at a cross section in the xy-plane located at $z = 0$ (i.e. at bottom base of Au particle) at wavelengths $\lambda_0 = 230$nm, 255nm, 300nm, 350nm, 400nm, 500nm and azimuthal incident angle $\phi_0 = 25°$. Reflectance plots of the relevant spectrum and ϕ_0 is included below.

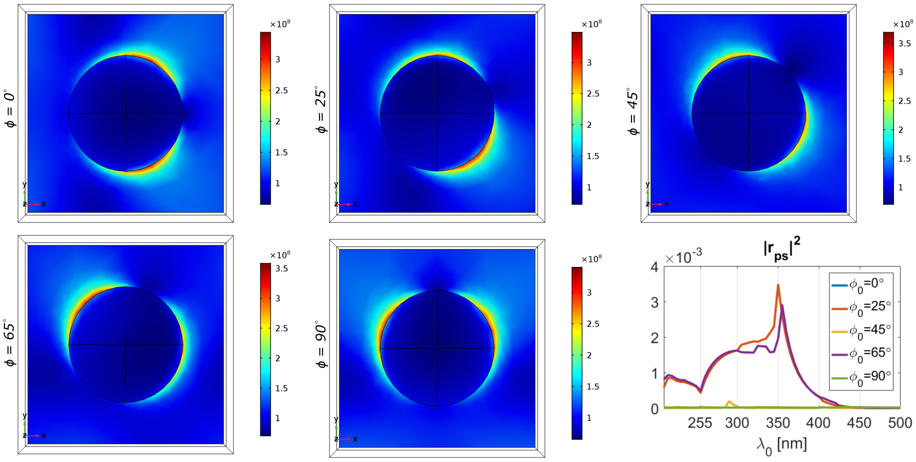

(a) TE

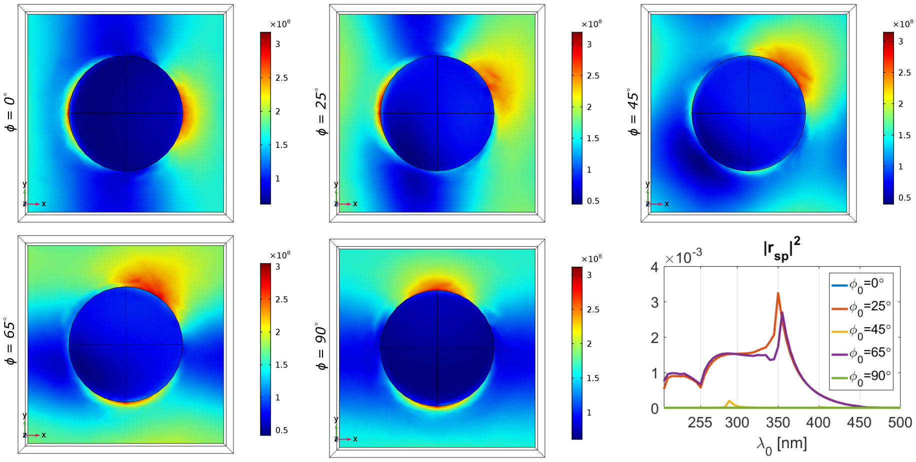

(b) TM

Figure 5.30: Electric field norm of sample 5A at wavelength $\lambda_0 = 350$ nm and azimuthal angles of incidence $\phi_0 = 0°, 25°, 45°, 65°, 90°$ when the incident beam is (a) TE- and (b) TM-polarized. The cross-section is located at the base of the Au particle, $z = 0$.

5.4.4 Comparing changes in lattice constants and particle ellipticity

This section will investigate the effect of sample 5A's non-uniform lattice constants and particle lateral parameters, in particular how they shape the LSPR resonance strength and wavelength position. Three models with similar geometry to sample 5A have been simulated; a completely uniform structure with square lattice and circular base of the Au particle; a structure with circular particle base but very rectangular lattice; lastly a structure with slightly elliptic Au particles and square lattice. The parameters for these are summarized in table 5.2, where sample 5A parameters are repeated for convenience. The models were simulated in COMSOL for wavelengths $\lambda = 500 - 800$ nm and incident azimuthal angles $\phi_0 = 0° - 180°$ in stepsizes of 5 nm and 5°, respectively, and incident polar angle was the usual $\theta_0 = 55°$.

Table 5.2: All quantities are given in nanometers.

	Uniform	Rectangular lattice	Ellipsoidal Au	Sample 5A
a_x	208.6	198.6	208.6	207.2
a_y	208.6	218.6	208.6	209.9
R_x	60.8	60.8	60.3	60.3
R_y	60.8	60.8	61.3	61.3
R_z	34.8	34.8	34.8	34.8
t	36.9	36.9	36.9	36.9

The main results of these simulations are found in figure 5.31, where peak Ψ_{pp} and the LSPR wavelength λ_{LSPR} is plotted with respect to incident azimuthal angle. The reader is reminded that $\phi_0 = 0°$ is defined along the x-axis. It is immediately observed that sample 5A follow closely the profile of the ellipsoidal particle. Sample 5A is seen to slightly shift towards the rectangular lattice profile at the extreme points of $\Psi_{pp}(\lambda_{\text{LSPR}})$, suggesting that its non-uniform lattice constants do have an effect, albeit small. In fact, in order for the rectangular lattice model to have noticeable effect on the LSPR, the lattice constants a_x, a_y had to be exaggerated compared to the estimated sample 5A parameters. Note that none of the models display a perfect 90° symmetry, not even the uniform sample where one might expect a 45° symmetry. Experimental data in figure 5.32 seem to inherit a symmetry similar to that of the ellipsoidal particle in figures 5.31.

The plasmonic properties of elongated gold particles (or nanorods) have been studied extensively the last decade [34] [16]. In particular the sensitive nature of plasmon resonances to their shape and orientation [45]. Figure 5.33 shows how Ψ_{pp} evolves into two separate LSPRs at $\phi_0 = 0°$ and $\phi_0 = 90°$ as the ellipticity of the Au particle increases. The resonance peak at $\phi_0 = 0°$ is blueshifted from 620 nm to a smaller peak at 580 nm where reflected s-polarized light dominates, while the resonance at $\phi_0 = 90°$ is redshifted from 630 nm to a stronger peak at 665 nm where most of the light reflected from the sample is p-polarized. This is in agreement with the intuition that light incident along the x-axis would experience a wider particle and thus strongly resonate with the s-polarized light, and similar for y-direction where light intuitively experiences a narrow but long Au particle that resonate with the p-polarization.

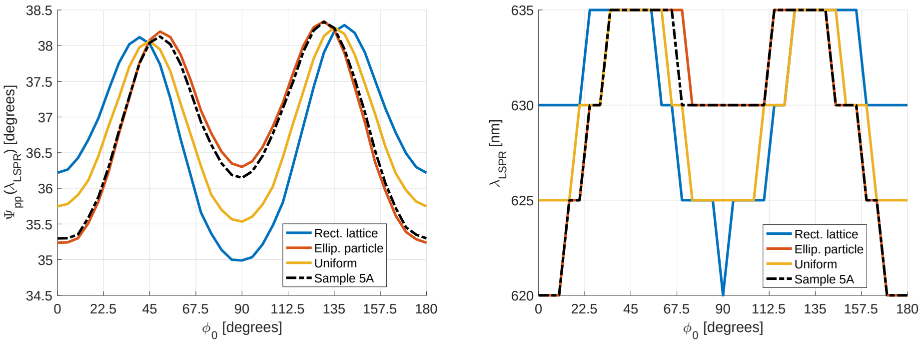

(a) **(b)**

Figure 5.31: Plots comparing models of Sample 5A with slightly different unit cell parameters; an exaggerated rectangular lattice with circular hemispheroidal gold particle; an ellipsoidal gold particle with square lattice; and a uniform model with hemispheroidal particle and square lattice. (a) Values of Ψ_{pp} at the peak LSPR resonance located at λ_{LSPR}, (b) shifts of λ_{LSPR} with respect to incident azimuthal angle ψ_0. Results of the original Sample 5A simulation, as in figure 5.20a, is also plotted (dash-dotted black line).

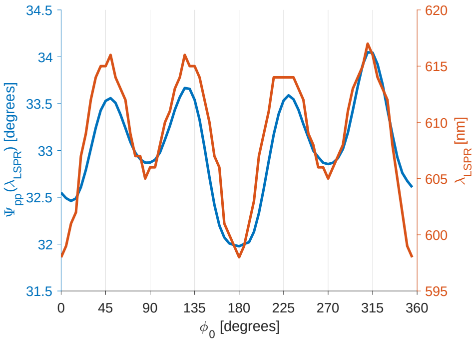

Figure 5.32: Experimental data of sample 5A revealing anisotropy of peak LSPR resonance with regards to wavelength and azimuthal angle of the incident light.

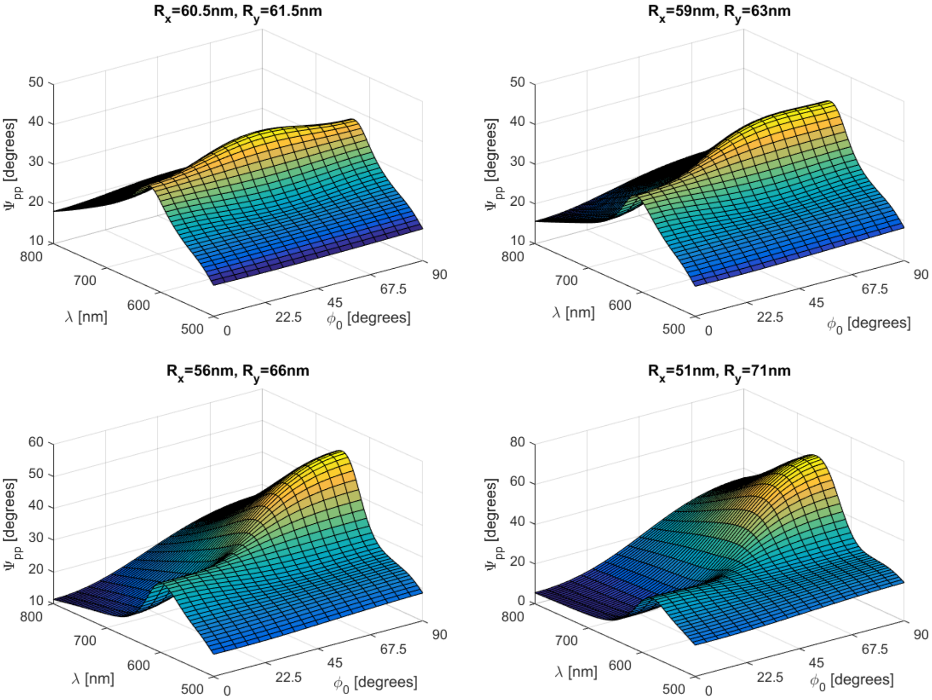

Figure 5.33: Variations of sample 5A parameters with increasing ellipticity of the gold particle, as marked in each subfigure. Common parameters for all four cases are the particle height $R_z = 34.8$nm, mound height $t = 36.9$nm, square lattice $a_{xy} = 209$nm and incident polar angle $\theta_0 = 55^\circ$. Azimuthal angle $\phi_0 = 0^\circ$ is defined along x-axis, while $\phi_0 = 90^\circ$ corresponds to light incident in positive y-direction.

5.5 Sample 5B

5.5.1 Experimental data

In figure 5.35 a SEM image of the experimental sample 5B together with a schematic of the reciprocal (square) lattice defining the azimuthal angle of incidence is repeated, for convenience. The reader is reminded of the sample being a rectangular lattice of anisotropic gold particles on a SiO_2 glass substrate, as discussed in section 3.1.3. The experimental MM showing contour plots of the elements with respect to photon energy and incident azimuthal angle is found in figure 5.34, while contour plots of ellipsometric amplitde angles Ψ_{pp}, Ψ_{sp} and Ψ_{ps} are found in figure 5.36 where Rayleigh lines corresponding to the first three BZ for air and glass are superposed. A plasmon resonance is observed in the energy region $1 - 1.5$ eV centered around $\phi_0 = 90°, 270°$, with strong polarization coupling observed around $\phi_0 = 45°, 135°$, etc. There is found a reduced symmetry in Ψ_{sp} and Ψ_{ps} compared to Ψ_{pp}, suggesting the sample has a $180°$ symmetry.

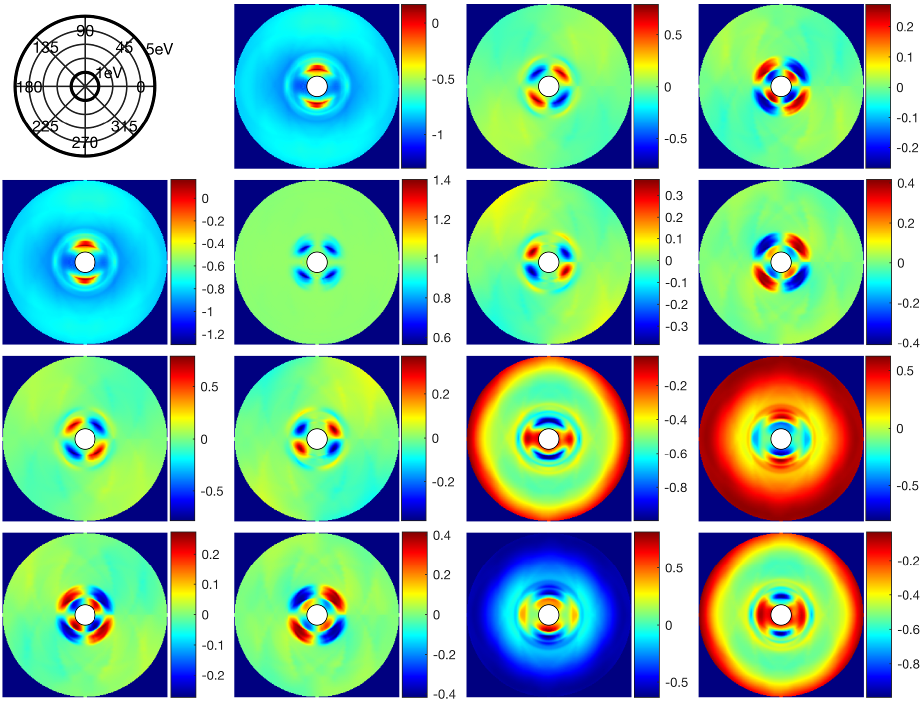

Figure 5.34: Contour plot of the MM elements of the experimental sample 5B measured at $\theta_0 = 55°$. Inner circle correspond to 0.73 eV while the outer circle is 5.9 eV.

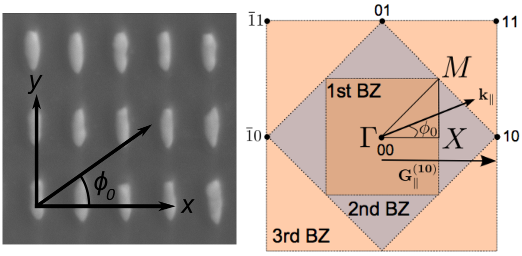

Figure 5.35: SEM image of sample 5B along with a definiton of incident azimuthal angle ϕ_0 (left). Conceptual sketch of a reciprocal square lattice (right).

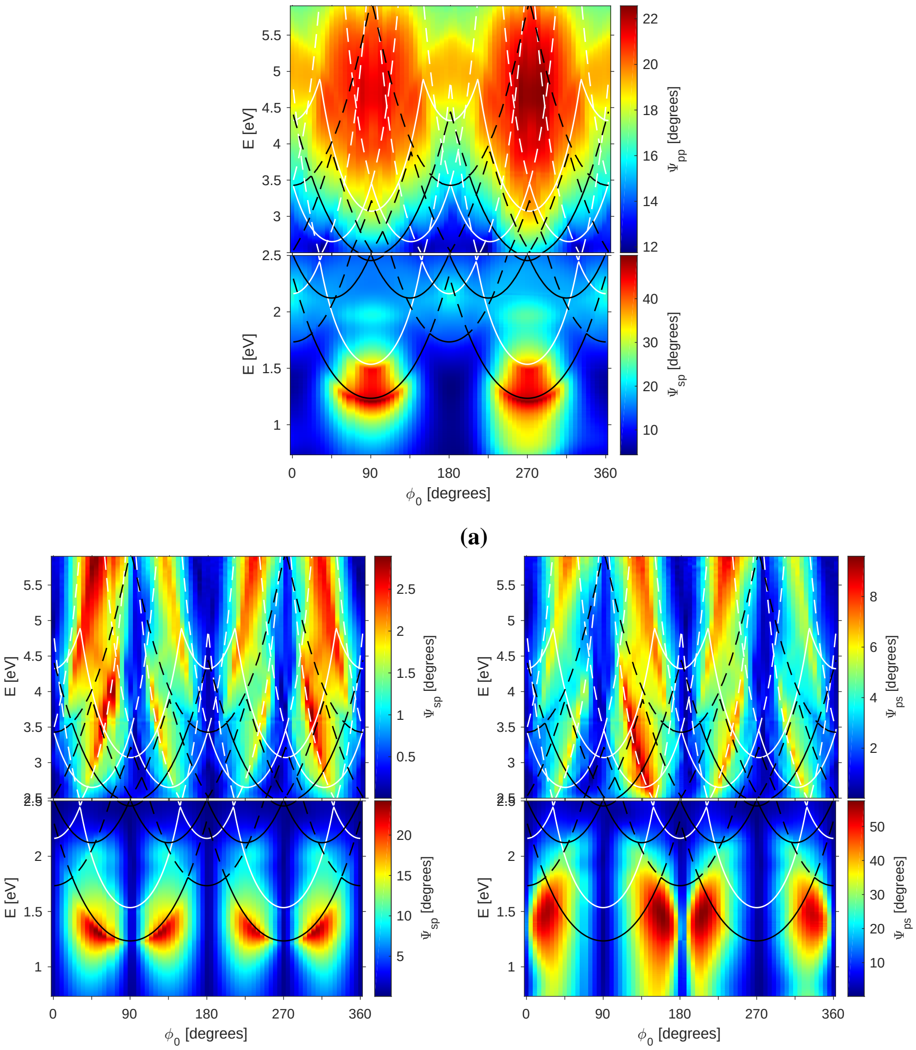

(a)

(b)

(c)

Figure 5.36: Contour plots of ellipsometric angles (a) Ψ_{pp} (b) Ψ_{sp} (c) Ψ_{ps} for the experimental data of sample 5B. To improve color contrast, each plot is plotted independently for energies above and below 2.5 eV. Rayleigh lines corresponding to the 1st, 2nd, and 3rd Brillouin zones are superposed for air (white lines) and substrate (black lines).

5.5.2 COMSOL simulation

Sample 5B has large lattice constants ($a_x = 315.4$ nm, $a_y = 443.9$ nm) compared to the spectrum of interest ($\lambda = 210 - 1700$ nm) thus creating a very large volume for the computational domain. As previously stated in section 3.1.3, the dielectric mound (with a height estimated at around 15 nm) was not included in the simulated geometry because the considerable amount of finite elements required to resolve the mound curvature. Even so, the desktop computer was not able to solve the model for the lower wavelengths due to the large amount of mesh elements, as defined in equation (5.1). The lowest wavelength resulting in a solvable mesh was 250 nm, i.e. the simulated region is $\lambda = 250 - 1700$ nm where each wavelength is swept for azimuthal angles $\phi_0 = 0° - 180°$. TE and TM simulations were not able to run simultaneously on the desktop computer due to the computationally demanding calculations. The program used at most 23.4 GB RAM during full wave calculation of the lowest wavelength, 250 nm, which was solved in 2 hours and 18 minutes in real-time. The solution time for each increasing wavelength decreased exponentially thereafter, finally solving for 1700 nm in just under 2 minutes. The total wall time, including both TE and TM simulations, was 94 hours and 59 minutes, where over 82% of this time was spent solving for wavelengths in the region $250 - 900$ nm. Multiplying the wall time by the number of CPU cores gives us an approximate CPU time of 23 days 17 hours and 54 minutes. In hindsight, creating a mound of triangular shape would not increase the amount of elements to the same degree as a curved mound, and could possibly result in a solvable model for a similar wavelength spectrum.

Contour plots of the optical response of the reflected COMSOL sample are given in figure 5.37 as R_{pp}, R_{ss} and Ψ_{pp}. Figure 5.37b reveal a resonance in R_{ss} around 1.4 eV excited by the transverse mode incident along the x-axis, i.e. $\phi_0 = 0°$, and a very small resonance at $\phi_0 = 90°$ around 2.1 eV. The longitudinal mode seen in figure 5.37a excites two plasmon resonances along the y-axis: a weak resonance sharply defined at 1.9 eV and a strong resonance between $1.20 - 1.54$ eV which is confined between the Rayleigh lines corresponding to the 1st BZs of SiO_2 and air. There is also observed a very weak resonance along the x-axis around 2.1 eV. Intuitively, one may interpret the weaker resonances at 2.1 eV at $\phi_0 = 0°$ and $\phi_0 = 90°$ for R_{pp} and R_{ss}, respectively, as weaker plasmon resonances appearing at higher energies due to the plasma electrons being driven to oscillate across the smaller width of the Au particles.

The field distributions for both modes at the strong LSPR located at photon energy 1.23 eV with $\phi_0 = 90°$ can be found in figure 5.38. It is clear that this plasmon resonance is mainly dipolar. Notice a factor 10 difference in field strength between TM and TE polarizations, where values for R_{pp} and R_{ss} at the same location is 0.20 and 0.128, respectively, confirming an enhanced field when the incident light is polarized along the semi-major axis of a particle with high aspect ratio. This is also observed for s-polarized light incident with azimuthal angles centered around the x-axis, i.e. the strong resonance around $\phi_0 = 0°, 180°$, in figure 5.37b. This resonance in reflected s-polarized light is not as obviously present in Ψ_{pp} in either COMSOL data (5.37c) or experimental data (5.36a). A disadvantage with reading data represented in ellipsometric amplitude angles such as Ψ_{pp} is the ambiguity in interpreting e.g. a low numerical value as either absence of reflected p-polarized light or an enhancement of s-polarized reflection. One can only assure with certainty a meaningful interpretation about their ratio, as $\Psi_{pp} = \arctan|r_{pp}/r_{ss}|$.

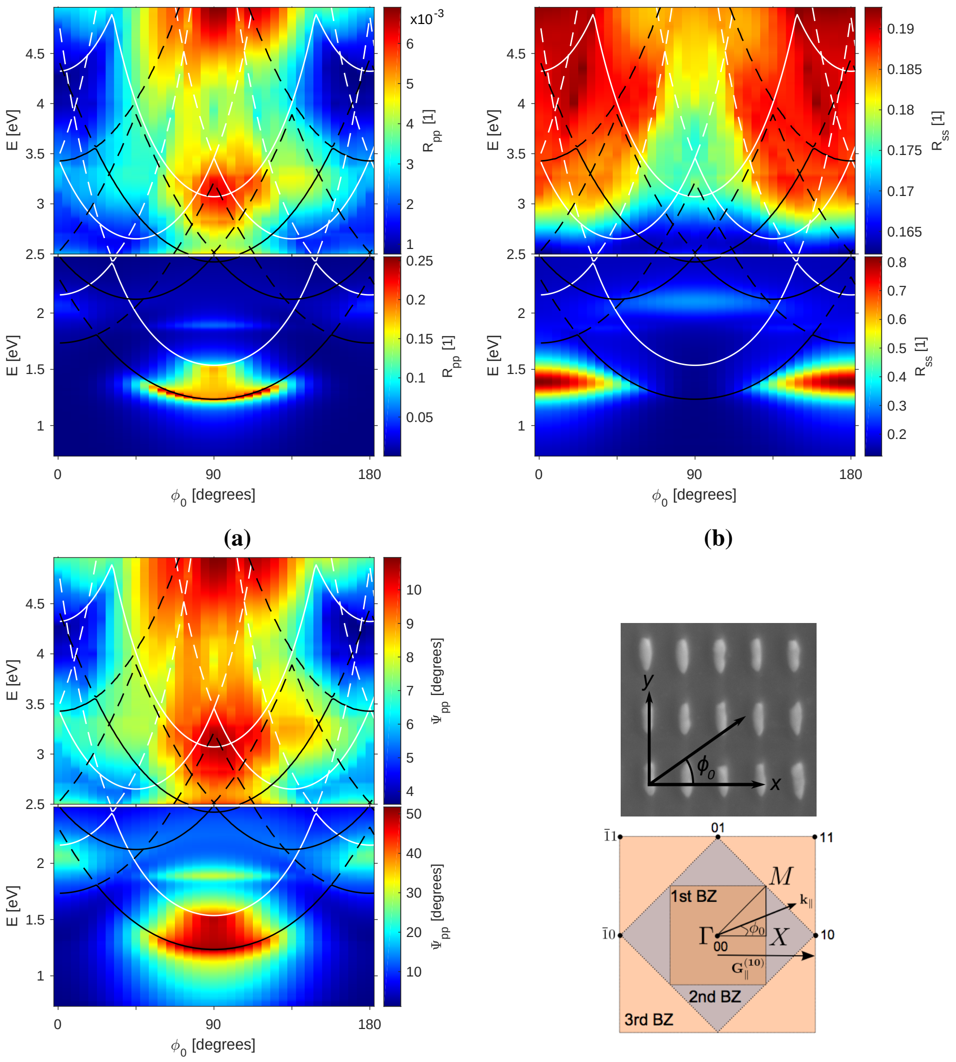

(a) **(b)**

(c)

Figure 5.37: Contour plots of (a) R_{pp} (b) R_{ss} and (c) Ψ_{pp} for sample 5B. For reasons of improved visibility, energies above 2.5 eV have independent colorbars. Rayleigh lines are shown corresponding to the boundaries of BZ-1 (confined by $\mathbf{G}_{\|}^{\bar{1}0}$ and $\mathbf{G}_{\|}^{0\bar{1}}$), BZ-2 ($\mathbf{G}_{\|}^{\bar{1}\bar{1}}$) and BZ-3 ($\mathbf{G}_{\|}^{\bar{2}0}$ and $\mathbf{G}_{\|}^{0\bar{2}}$) for air (white) and glass substrate (black). In addition, extended Rayleigh lines are shown in dashed lines. Brillouin zones with reciprocal lattice vectors $\mathbf{G}_{\|}^{\bar{1}\bar{1}}$ for air and substrate are recognized by their 45° symmetry, while the others are symmetric around 90°.

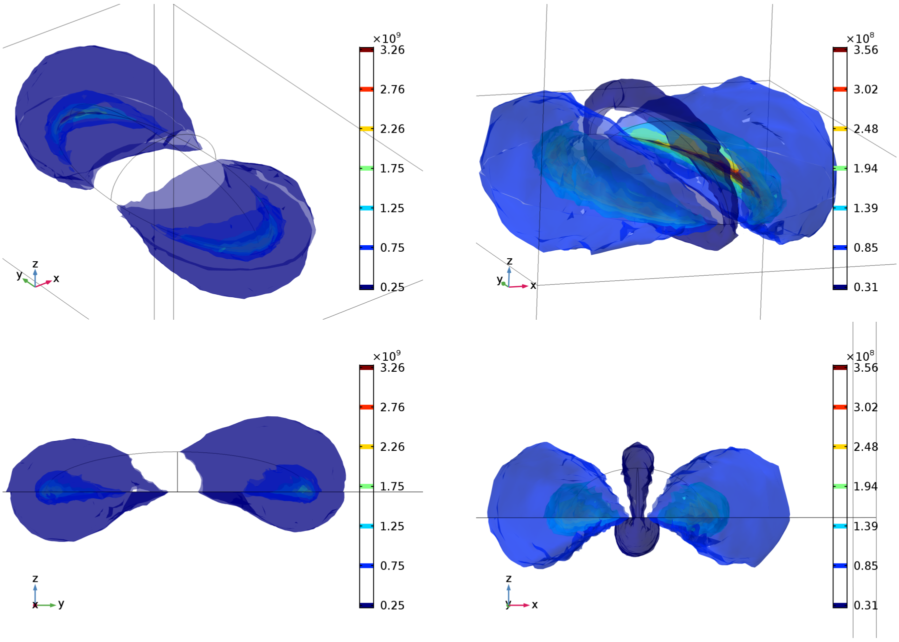

(a) TM **(b)** TE

Figure 5.38: Field concentration around the gold particles of sample 5B when the incident beam has wavelength $\lambda = 1010$ nm (1.23 eV) and azimuthal angle $\phi_0 = 90^\circ$ polarized (a) longitudinal and (b) transversal to the plane of incidence, where each plot is given at two different viewpoints (top and bottom). The interface between air and substrate is seen as a horizontal line in the bottom figures. The field amplitude E_{norm} is plotted for seven layers of isosurfaces given in SI units V/m.

Figure 5.37 reveal that 82% of light with photon energy 1.4 eV centered around the x-axis is reflected (the rest being transmitted or dissipated into the particle as heat), moreover, virtually all of it is reflected by s-polarized light.

The particle thickness in sample 5B is arguably similar to the Au particles of samples 5A and 6 ($R_x^{5\text{B}} = 47.4$ nm, $R_x^{5\text{A}} = 60.3$ nm, $R_x^{6} = 38$ nm), whereas sample 5B, however, is in comparison highly elongated with aspect ratio $e = R_y/R_x = 2.4$. In that regard, we observe a redshift of the LSPR (acting as a dipole resonance in figure 5.38a) in the elongated particle (5B) compared to the more circular particles (5A and 6) [45]. Furthermore, whereas the strong resonances of both p- and s-polarized light around $E = 1.4$ eV are dipolar, we suspect that the sharp resonance in R_{pp} at $E = 1.9$ eV might be a multipole as a product of the oblong particle shape [45]. Indeed, figure 5.39 reveal a field concentration around the Au particle at 1.9 eV that resembles a quadrupole. However, quadrupoles are expected to be forbidden at this orientation due to symmetry constraints. We thus speculate a multipole of order three, as is observed in [45] for single gold particles of similar thickness but higher aspect ratio ($e = 6$) excited by light polarized along the major particle axis.

With sample 5B being a rectangular lattice, the Rayleigh lines become more compli-

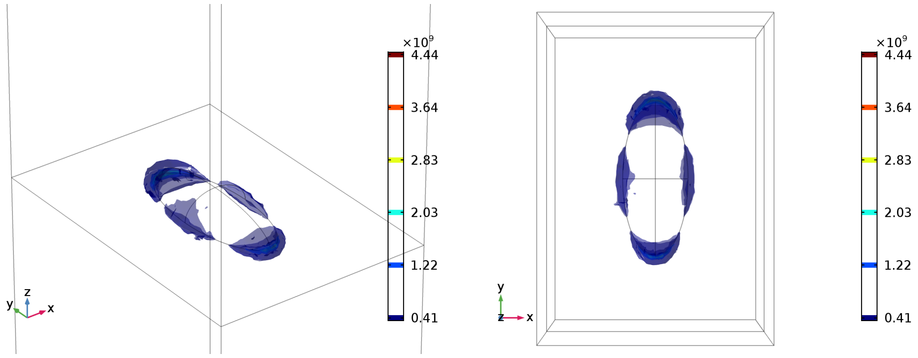

Figure 5.39: Six layers of isosurfaces showing E_{norm} (units V/m) when the incident field is p-polarized with azimuthal incidence $\phi_0 = 90°$ and photon energy 1.9 eV ($\lambda = 655$ nm), exposing what might look like a multipole resonance. Two viewpoints: (left) general view and (right) $\hat{z}$ pointing out of paper.

cated to interpret. The lowest energy Rayleigh line for glass (black line) has an abrupt change at $\phi_0 = 22.5°$ where $\mathbf{G}_{\|}^{0\bar{1}}$ begin to appear at lower energies than $\mathbf{G}_{\|}^{\bar{1}0}$. The Rayleigh line of glass calculated using $\mathbf{G}_{\|}^{\bar{1}0}$ in equation (2.53) is still visible in the region $\phi_0 = 22.5° - 157.5°$ as dashed black lines (i.e. as an extended Rayleigh line). The same abrupt changes can be observed for the 3rd BZ Rayleigh line in glass at $E = 3.5$ eV for angles $\phi_0 = 22.5°, 157.5°$ due to $\mathbf{G}_{\|}^{0\bar{2}}$ appearing at lower energies than $\mathbf{G}_{\|}^{\bar{2}0}$ in the Rayleigh line equation. The lines corresponding to 2nd BZ boundary, i.e. with $\mathbf{G}_{\|}^{\bar{1}\bar{1}}$, are seen to have symmetry around $\phi_0 = 45°$. The same patterns can be observed for Rayleigh lines in air (white lines).

As a consequence of the large lattice constants the Rayleigh lines for the 1st BZ go deep into the LSPR region of the particles. These are seen to sharply define the edges of the resonance located around $\phi_0 = 90°$ in R_{pp}, while the 1st BZ in glass also seem to dampen the R_{ss} resonance at the X-point. This effect has previously been studied in [52].The extended Rayleigh line of $\mathbf{G}_{\|}^{\bar{1}0}$ in air appear to dictate, to a certain degree, the response of R_{pp} and R_{ss} for $E > 2.5$ eV.

An attempt has been made to plot the peak values of R_{pp} and R_{ss} in figure 5.40. It is observed that the peak resonance of p-polarized reflected light around $\phi_0 = 90°$ follow the Rayleigh line for glass, and the strongest reflectance is actually at $\phi_0 = 65°, 115°$. It is again emphasized that the majority of reflected light is s-polarized, suggesting that mainly p-polarized light couples with the electron plasma. Heat dissipation is plotted in figure 5.41 for both TE and TM modes. For TM, the Au particles are observed to undergo heating at the major LSPR at $\phi_0 = 65°, 115°$, as well as the quadrupole and the secondary LSPR at $\phi_0 = 0°$. The majority of heat dissipation from the EM field into the Au particles for TE mode is observed to happen at the secondary LSPR centered around $\phi_0 = 90°$ at 2.1 eV. There is heating to a lesser extent at the LSPR at $\phi_0 = 0°$ which is seen to be exceedingly reflective of s-polarized light in figure 5.37b.

Seeing as the LSPR is consentrated along the rim base of the Au particles in direct contact with the substrate, they may be subject to the dispersive SiO_2 refractive index which

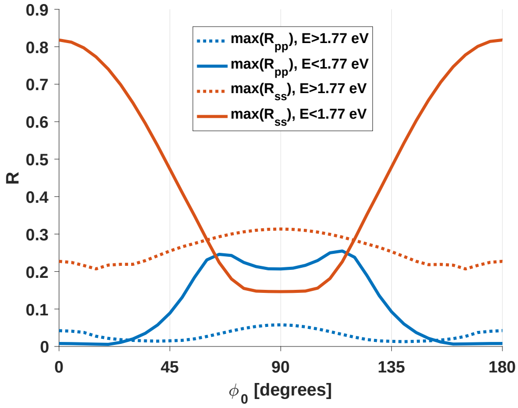

Figure 5.40: Peak values of reflectances of p- and s-polarized light, $\mathtt{max}(R_{pp})$ and $\mathtt{max}(R_{ss})$. An attempt to distinguish the strong resonances observed around 1.4 eV from the weaker resonances around 2 eV has been made by plotting peak values above and below 1.77 eV ($\lambda = 700$ nm) separately.

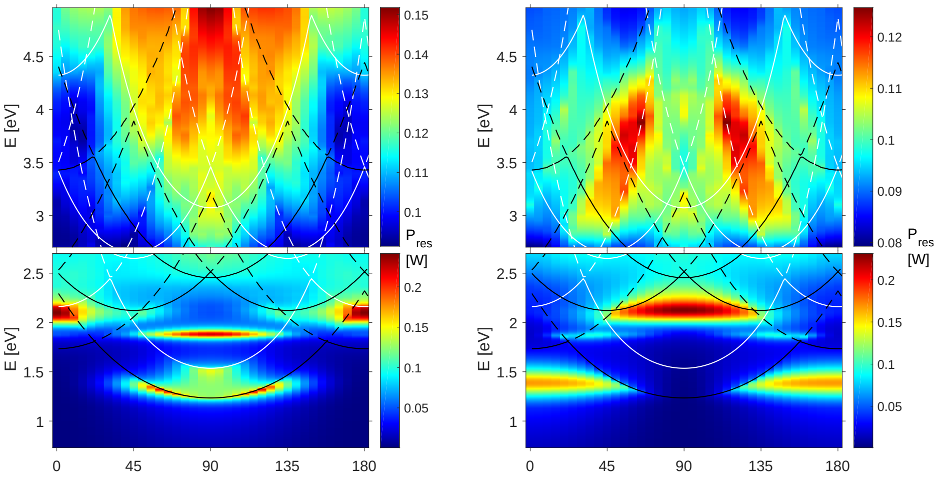

(a) TM

(b) TE

Figure 5.41: Energy from the incident light dissipated into the gold particle (given in SI units W) as a function of energy E and azimuthal incident angle of the incoming beam. Resistive heating $P_{\text{resistive}}$ of the gold particle when the incident light is (a) p-polarized (TM) and (b) when the incident light is s-polarized (TE). For visual clarity in the color coding, both figures have independent colorbars for energies above and below 2.7 eV. Rayleigh lines are superimposed corresponding to the borders of BZ-1, BZ-2 and BZ-3 for the ambient air (white lines) and the glass substrate (black lines), as well as their respective extended lines (dashed lines).

varies from 1.514 to 1.446 in the simulated region. It has been shown that gold nanoparticles with high aspect ratios are extremely sensitive to the ambient refractive index, where the longitudinal LSPR peak redshifts as the refractive index increases and the shift amplitude inreases with the aspect ratio [16] [34]. Although the difference would likely be minimal, it could be interesting to note the effect of the dispersive glass substrate by comparing the results with a similar simulation where the glass refractive index is constant, which could be a source for future work.

The Mueller matrix of the simulated data can be found in figure 5.42. For energies above 2.5 eV the sample is mostly isotropic, as the reflection MM resembles equation (2.19) and the majority of light is either dissipated into the paricles as shown in figure 5.41 or transmitted through the glass (transmission results not shown). There is, however, a weak polarization coupling present for $E > 2.5$ eV, as seen in figure 5.43, which to a certain extent seem to follow the Rayleigh lines for air, particularly the extended lines for $\mathbf{G}_{\parallel}^{\bar{1}0}$. This weak conversion of polarization is also visible in the upper block off-diagonal elements in figure 5.42 where a scaling has been applied to improve visibility. The $180°$ symmetry of the experimental sample, as mentioned in section 5.5.1, share its symmetry with R_{ps} of the simulated data, whereas R_{sp} is $90°$ symmetric. The cause of this uneven symmetry in polarization conversion is unknown. The conversion of s-polarized light to p-polarized light and vice versa is observed to be equal in the lower energy LSPR region, however, with peak resonance at $\phi_0 = 50°, 130°$.

The experimental MM is already found in figure 5.34. Note that the off-diagonal MM elements of the experimental sample are overall larger than its COMSOL counterpart. This suggest a structure-induced anisotropy caused by the dielectric mound, which has been neglected in the simulation. Judging from their Mueller matrices, the COMSOL model is found to be in good qualitative agreement with the experimental ellipsometric data. By comparing their values side-by-side as in figure 5.44, however, we see a quantitative disparity immediately following the resonances around 2 eV.

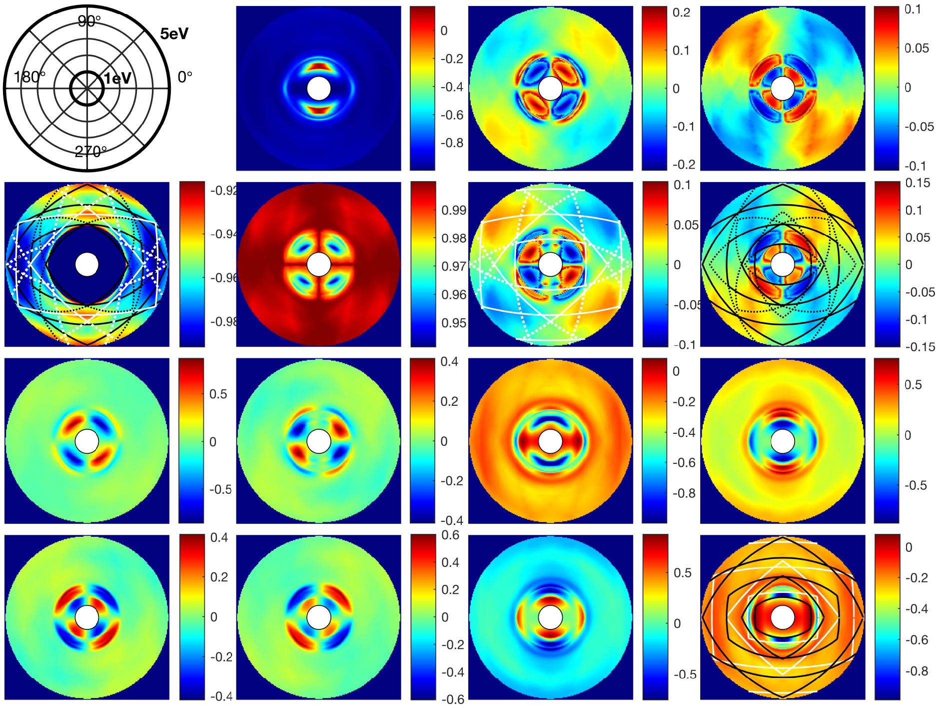

Figure 5.42: Contour plots of the normalized Mueller matrix elements for the simulated sample 5B. Energy and azimuthal angle of the incident light are represented by radius and rotation angle in each polar plot, respectively. Inner circle of the schematic in m_{11} corresponds to photon energy 0.73 eV while the outermost circle corresponds to 4.96 eV. Scaling has been applied to a few elements, for reasons of improved clarity in energy regions above 2.3 eV; Resonant values in the upper off-block elements m_{13}, m_{14}, m_{23} and m_{24} were reduced by $|m_{ij}|^{1/4}\text{sign}(m_{ij})$ and similar for m_{22}, while element $m_{21} = m_{12}$ has been set completely void for energies below 2.35 eV. Furthermore, in m_{44}, reduced Rayleigh lines are drawn for air (white lines) and glass substrate (black lines). For glass, the first four Brillouin zones can be seen in this element, as well as parts of BZ-5 ($\mathbf{G}_{\|}^{\bar{3}0}$ and $\mathbf{G}_{\|}^{0\bar{3}}$) . The first BZ can be seen as the innermost upright rectangle, BZ-2 is the tilted semi-square, BZ-3 is again an upright semi-rectangle but larger, while BZ-4 ($\mathbf{G}_{\|}^{\bar{2}\bar{2}}$) is the largest tilted semi-square, seen only for glass. In elements m_{23} and m_{24}, the extended Rayleigh lines (dotted lines) are also included for air and substrate, respectively. Lastly, in element m_{21} all Rayleigh lines (excluding BZ-1) for both air and substrate are superimposed.

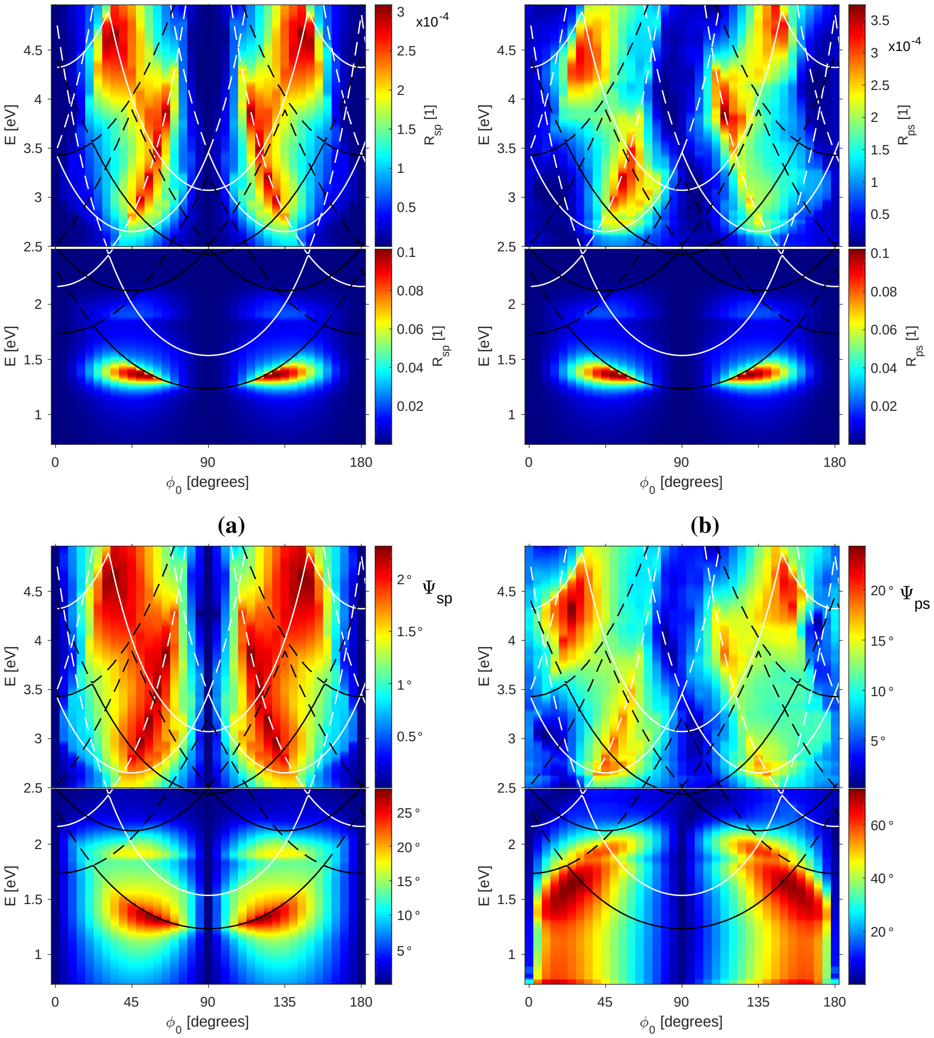

(a) **(b)**

(c) **(d)**

Figure 5.43: Contour plots of (a) R_{sp} (b) R_{ps} (c) Ψ_{sp} and (d) Ψ_{ps} for sample 5B. To improve color contrast, each plot is plotted independently for energies above and below 2.5 eV.

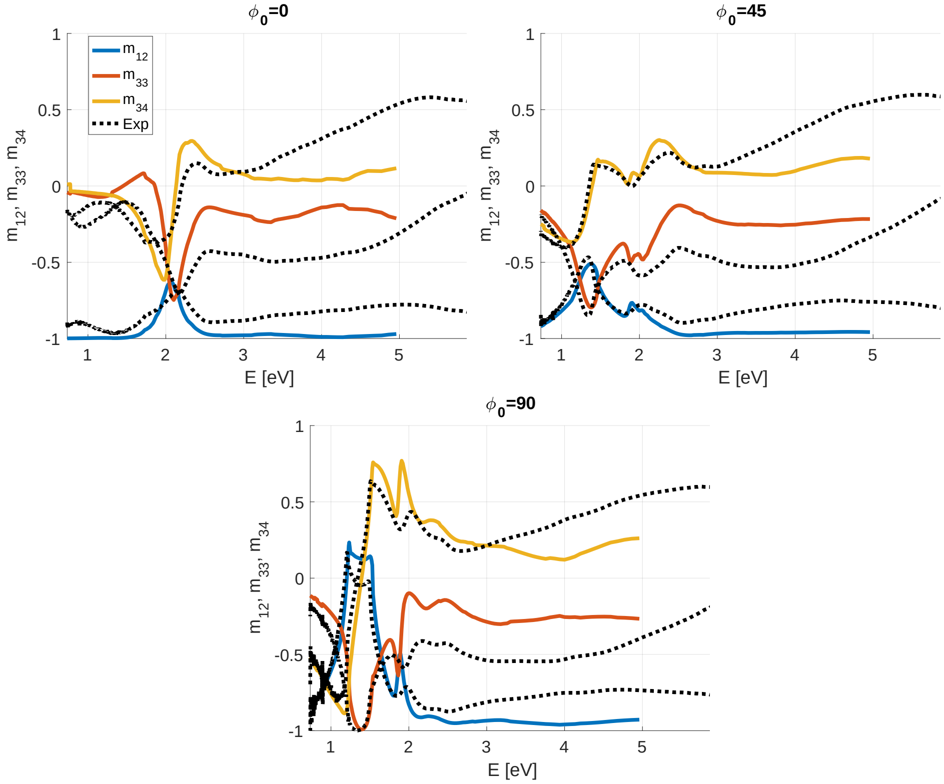

Figure 5.44: Normalized MM elements m_{12}, m_{33} and m_{34} compared with experimental data for sample 5B at three chosen angles of azimuthal incidence.

5.6 Tilted GaSb cones

The COMSOL model for the tilted GaSb cones was created using the previous Au particle model as a template. The geometry was changed to suit the sample, including a hexagonal lattice where Floquet periodicity was applied to all six sides, similar to what was shown for the square lattice in figure 5.3. A motivation for modelling these densely packed GaSb cones was to retrieve a high energy optical response beyond what was achieved in [35], i.e. up to 24 eV. This would not be possible without the model improvements on optimization discussed in section 5.2. Even so, the desktop computer managed at most to compute the model for 13.78 eV, or 90 nm wavelength, before running out of memory. Furthermore, each TE and TM simulation had to be split into three parts running for different regions of the wavelength spectrum, otherwise the computer would run into memory issues. The elapsed real time (wall time) of these simulations are shown in table 5.3. Total wall time for the entire process was 4 days, 4 hours and 1 minute, however, for wavelengths larger than 195 nm it was possible to run both TE and TM simulations simultaneously. The total CPU time, assuming the labour was at all times divided evenly among the 6 CPU cores, was approximately 25 days and 6 minutes. Again, figure 5.6 reveals how the computation time of each iteration depends on the wavelength.

Table 5.3: Elapsed real time for the calculation of the, in total, six simulations that had to be computed in order to retrieve a full TE- and TM-wave optical response of the tilted GaSb cones in the wavelength region 90 nm to 1600 nm. Total run time for the entire simulation process was 100hr 1min.

Spectrum [nm]	TE	TM
90-195	20hr 23min	20hr 29min
200-900	20hr 50min	20hr 35min
905-1600	8hr 52min	8hr 52min

In both the experimental sample and simulated model the cones are aligned so that their tilts are pointing in the direction of the incident plane at $\psi_0 = 0°$. Figure 5.45 includes both the simulated and experimental MM plotted with respect to incident photon energy and azimuthal angle, for energies limited by the ellipsometer instrumentation. They are deemed in good agreement with each other. However, it is clear that the simulated results does not exhibit the rotational asymmetry in the off-diagonal elements $m_{23}, m_{24}, m_{32}, m_{42}$ to the same extent as the ellipsometry results. This implies subtle differences in the cone geometry of the model and experimental sample. The sample is observed to be pseudo isotropic along $\phi_0 = 0°$ as block off-diagonal elements are zero.

The full spectrum MM of the simulation can be seen in figure 5.46, revealing strong polarization coupling around $6 - 10$ eV as the incidence plane is rotated. Note that the manifestations of polarization coupling seen in the block off-diagonal elements in figure 5.45 are too weak to be seen here, although they are considered to be the onset of polarization conversion observed for the higher energies. The block off-diagonal elements have two alternating maxima and minima. The coupling is also clearly observed in the cross-polarized reflectance plots in figure 5.47, reporting an equal amount of conversion from both polarizations with a slightly unequal sensitivity to the angle of incidence. We can

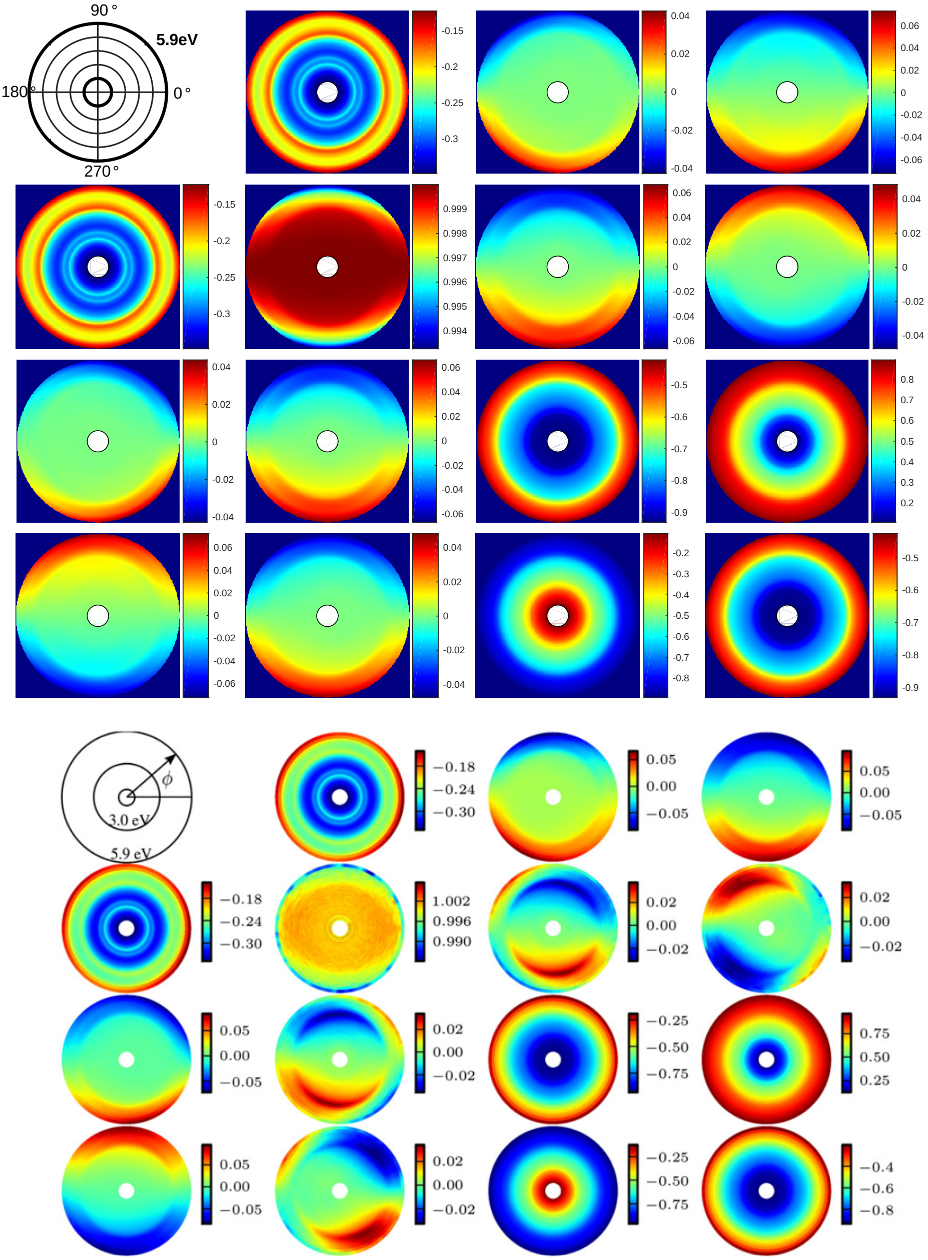

Figure 5.45: MM contour plots of tilted GaSb cones simulated in COMSOL (top) compared to experimental results (bottom) as found in [35], for incident polar angle $\theta_0 = 45^\circ$. Inner radius for simulated and experimental plots corresponds to 0.775 eV and 0.73 eV, respectively, while outer circle corresponds to 5.9 eV for both.

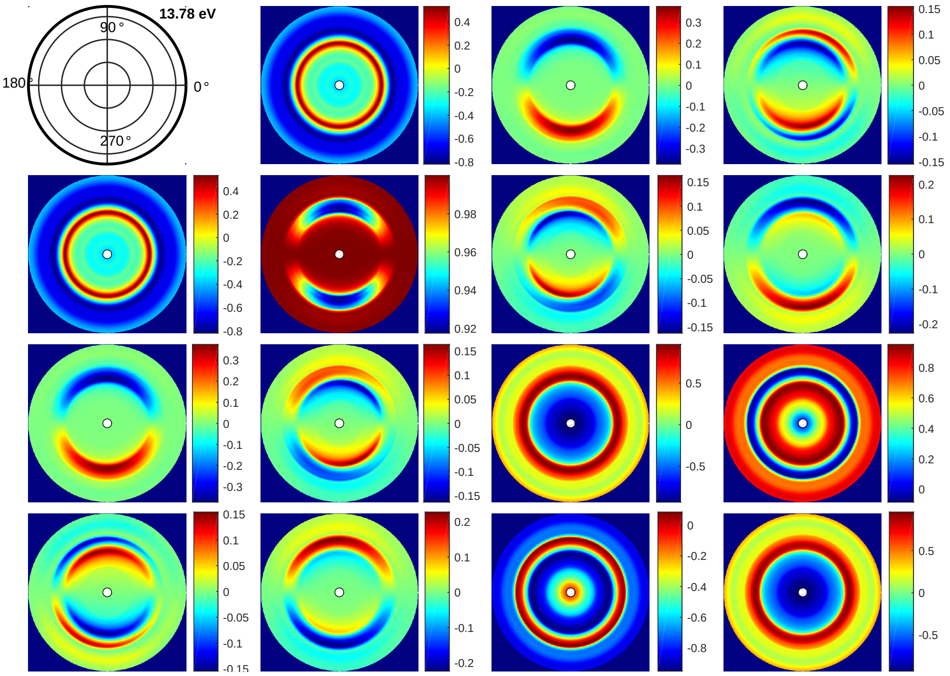

Figure 5.46: Contour plots of the MM elements for the simulated GaSb tilted cones in the energy range 0.775 eV (innermost circle in each element) to 13.78 eV (outer circle). The inner circles in the schematic replacing the m_{11} element marks the radii at energies 4 eV, 8 eV and 12 eV.

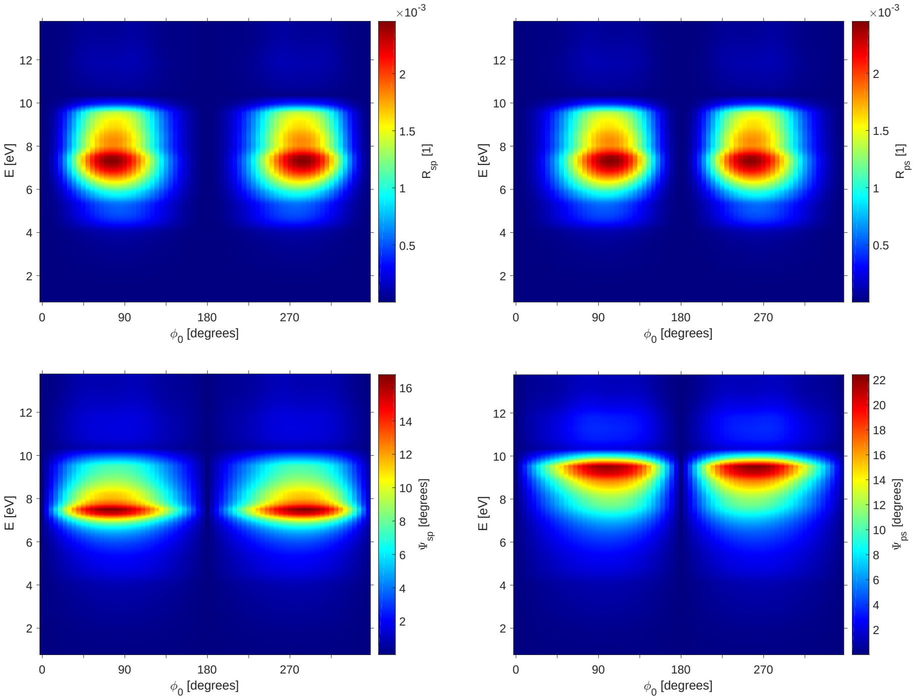

Figure 5.47: Contour plots of (a) R_{sp} (b) R_{ps} (c) Ψ_{sp} and (d) Ψ_{ps} for inclined GaSb cones simulated in COMSOL.

conclude a maximum sensitivity to the cones' inclination at around 7.5 eV with incident azimthual angle normal to the tilt angle.

It is likely possible to further optimize the model in order to simulate the tilted GaSb cones for energies up to 24 eV without upgrading the computer hardware. One could attempt to further reduced the height of the physical domain. However, we have seen that the amount of elements increases exponentially with decreasing wavelength (figure 5.6), while there is a linear relationship to the amount of elements with a change in height. Another solution, if feasible, is to exploit the 180° symmetry of the unit cell and only build half the geometry. The other half could be simulated using symmetry boundary conditions, e.g. a perfect electric conductor. If this fails, one could utilize COMSOL's cluster computing functionality to distribute the workload in parallel with other computers. For example, parametric sweeps (here: wavelength iterations) can be distributed with individual parameter cases to each cluster node.

Chapter 6

Conclusion and outlook

Conclusion

The primary goal of the work on this thesis - developing a functioning COMSOL model of infinite periodic plasmonic surfaces and testing its validity against established experimental work - has been fulfilled. The simulation results were found in good correspondence with the experimental data from three variations of hemispheroidal gold particles on glass substrates. Their complete polarization dependent optical responses were reproduced, including plasmon resonances, polarization coupling, and dependencies on Rayleigh anomalies. Time would allow to test the model on only one additional system, a nanostructure of densely packed tilted GaSb cones. There is confidence in the finished state of the COMSOL model, which can be used as a template for modeling the optical response of other structures with 2D periodicity of both rectangular and hexagonal lattices. Minor adjustments such as mesh setup will likely be necessary when implementing a new system, depending on the structure geometry.

COMSOL is effective in computing the full-wave solution for single wavelengths, however, solving for a large range of wavelengths was found to be very time consuming. Efforts put into optimizing the model drastically reduced the computational costs. For each increasing wavelength iteration, both the memory usage and computation time were found to decrease exponentially. Computational cost is heavily dependent on the size of the unit cell compared to the wavelength, which ultimately decides the amount of finite elements the computer has to solve.

Results from these simulations can be represented as ellipsometry angles (both amplitude and phase differences), Mueller matrices, reflection coefficients, reflectance, heat dissipation and field distributions. There is also confidence in the possibility to extract phase shift information from S-parameters.

Outlook

We have shown that the COMSOL models work for a full 3D representation of each sample unit cell. However, there are symmetries in the nanostructures that have not been exploited.

For example, by building the geometry only to its symmetry point and simulating the omitted geometry using symmetry boundary conditions, one may potentially reduce the computational cost by a significant amount. The solution may even be more accurate as a much denser mesh can be used. For sample 5B, this could mean a successful solution of wavelengths much lower than 250 nm, while the tilted GaSb cones would come closer to its 24 eV goal. Furthermore, COMSOL's support for cluster computing remains unexplored, which could result in an extreme reduction in computation time.

The COMSOL model developed in this thesis may be used to study and optimize the optical response of ordered nanostructures, notably applicable to structures with dimensions beyond the limit of effective medium models. This can be useful both in terms of designing new structures e.g. metasurfaces, and for parameter retrieval and characterization of existing structures.

Bibliography

[1] George B. Arfken and Hans J. Weber. *Mathematical Methods for Physicists*. Elsevier Academic Press, sixth edition, 2005.

[2] Hans Arwin. *Thin Film Optics and Polarized Light*. Hans Arwin, the aureus edition, Jan 2014.

[3] D.E. Aspnes. Plasmonics and effective-medium theories. *Thin Solid Films*, 519:2571–2574, 2011.

[4] R.M.A. Azzam and N.M. Bashara. *Ellipsometry and polarized light*. North-Holland, 1977.

[5] R. T. Lechner H. Ditlbacher J. R. Krenn A. Leitner F. R. Aussenegg B. Lamprecht, G. Schider. Metal nanoparticle gratings: Influence of dipolar particle interaction on the plasmon resonance. *Physical Review Letters*, 84(20), 2000.

[6] Jean-Philippe Banon, Torstein Nesse, Zahra Ghadyani, Morten Kildemo, and Ingve Simonsen. Critical dimension metrology of a plasmonic photonic crystal based on mueller matrix ellipsometry and the reduced rayleigh equation. *Optics Letters*, 2017. (in press).

[7] Jan Becker, Andreas Trügler, Arpad Jakab, Ulrich Hohenester, and Carsten Sönnichsen. The optimal aspect ratio of gold nanorods for plasmonic bio-sensing. *Plasmonics*, 5(2):161–167, 2010.

[8] Dick Bedeaux and Jan Vlieger. *Optical Properties Of Surfaces (2nd Edition).*, volume 2nd ed. Imperial College Press, 2004.

[9] Jean-Pierre Berenger. A perfectly matched layer for the absorption of electromagnetic waves. *Journal of Computational Physics*, 114:185–200, 1994.

[10] Jean-Pierre Berenger. Three-dimensional perfectly matched layer for the absorption of electromagnetic waves. *Journal of Computational Physics*, 127(0181):363–379, 1996.

[11] Jean-Pierre Berenger. Numerical reflection of evanescent waves from perfectly matched layers. In *IEEE Antennas and Propagation Society International Symposium 1997. Digest*, volume 3, pages 1888–1891 vol.3, July 1997.

[12] Jean-Pierre Berenger. Evanescent waves in pml's: origin of the numerical reflection in wave-structure interaction problems. *IEEE Transactions on Antennas and Propagation*, 47(10):1497–1503, Oct 1999.

[13] Craig F. Bohren and Donald R. Huffman. *Absorption and Scattering of Light by Small Particles*. Wiley-VCH Verlag GmbH, Dec 2007.

[14] Thomas Brakstad. Spectroscopic mueller matrix analysis of plasmonic nanostructures fabricated by focused ion beam. Master's thesis, Norges teknisk-naturvitenskapelige universitet, Fakultet for naturvitenskap og teknologi, Institutt for fysikk, 2014.

[15] Thomas Brakstad, Morten Kildemo, Zahra Ghadyani, and Ingve Simonsen. Dispersion of polarization coupling, localized and collective plasmon modes in a metallic photonic crystal mapped by mueller matrix ellipsometry. *Opt. Express*, 23(17):22800–22815, Aug 2015.

[16] Yong Chen and Hai Ming. Review of surface plasmon resonance and localized surface plasmon resonance sensor. *Photonic Sensors*, 2(1):37–49, 2012.

[17] Weng Cho Chew and William H. Weedon. A 3d perfectly matched medium from modified maxwell's equations with stretched coordinates. *Microwave and Optical Technology Letters*, 7(13):599–604, 1994.

[18] J.A. Woollam Co. Ellipsometry data analysis. https://www.jawoollam.com/resources/ellipsometry-tutorial/ellipsometry-data-analysis, 2017. Online; accessed July 2017.

[19] Bruce T. Draine and Piotr J. Flatau.

[20] M. S. Dresselhaus. *Solid State Physics Part II, Optical Properties of Solids*. MIT, revised lecture notes edition, 2001. Online; accessed July 2017.

[21] U. Fano. The theory of anomalous diffraction gratings and of quasi-stationary waves on metallic surfaces (sommerfeld's waves).

[22] Walter Frei. *How Much Memory Is Needed to Solve Large COMSOL Models?* COMSOL Inc., Oct 2014. https://www.comsol.com/blogs/much-memory-needed-solve-large-comsol-models/, Online; accessed August 2017.

[23] Walter Frei. *Modeling Electromagnetic Waves and Periodic Structures*. COMSOL Inc., Jan 2014. https://www.comsol.com/blogs/modeling-electromagnetic-waves-periodic-structures/, Online; accessed July 2017.

[24] Walter Frei. *Simulation Tools for Solving Wave Electromagnetics Problems*. COMSOL Inc., June 2015. https://www.comsol.com/blogs/simulation-tools-for-solving-wave-electromagnetics-problems/, Online; accessed July 2017.

[25] Walter Frei. *Using Perfectly Matched Layers and Scattering Boundary Conditions for Wave Electromagnetics Problems*. COMSOL Inc., Jan 2015. https://www.comsol.com/blogs/using-perfectly-matched-layers-and-scattering-boundary-conditions-for-wave-electromagnetics-problems/, Online; accessed July 2017.

[26] Walter Frei. *Keeping Track of Element Order in Multiphysics Models*. COMSOL Inc., Feb 2016. https://www.comsol.com/blogs/keeping-track-of-element-order-in-multiphysics-models/, Online; accessed July 2017.

[27] Russell J. Gehr and Robert W. Boyd. Optical properties of nanostructured optical materials. *Chem. Mater.*, 8:1807–1819, 1996.

[28] Accurion GmbH. Principle of ellipsometry. http://www.accurion.com/spectroscopic-ellipsometry, 2017. Online; accessed July 2017.

[29] Dennis Goldstein. *Polarized Light*. CRC Press, second edition, revised and expanded edition, 2003.

[30] P. Grahn, A. Shevchenko, and M. Kaivola. Interferometric description of optical metamaterials. *New Journal of Physics*, 13, Nov 2013.

[31] David J. Griffiths. *Introduction to Electrodynamics*. Pearson, third edition edition, 1999.

[32] P. S. Hauge, R. H. Muller, and C. G. Smith. Conventions and formulas for using the mueller-stokes calculus in ellipsometry. *Surface Science*, 96:81–107, June 1980.

[33] M.-J. Hitoshi Kuwata, M.-J. Hiroharu Tamaru, M.-J. Kunio Esumi, and M.-J. Kenjiro Miyano. Resonant light scattering from metal nanoparticles: Practical analysis beyond rayleigh approximation. *Applied Physics Letters*, 83(22):4625 – 4627, 2003.

[34] Qian Li Huanjun Chen, Lei Shao and Jianfang Wang. Gold nanorods and their plasmonic properties. *Chem. Soc. Rev.*, 42, 2013.

[35] Kristin Høydalsvik, Lars Martin S. Aas, Ellen Døli, Elin Søndergård, Morten Kildemo, and Dag Werner Breiby. Combining surface x-ray scattering and ellipsometry for non-destructive characterization of ion beam-induced gasb surface nanostructures. *Thin Solid Films*, 571, Part 3:538 – 542, 2014. 6th International Conference on Spectroscopic Ellipsometry (ICSE-VI).

[36] M.S. Bradley I.F. Almog and V. Bulovi. The lorentz oscillator and its applications, 2011. http://ocw.mit.edu.

[37] COMSOL Inc. *COMSOL Multiphysics Reference Manual*. Comsol 5.2a edition, 2016.

[38] COMSOL Inc. *Wave Optics Module - User's Guide*. Comsol 5.2a edition, 2016.

[39] COMSOL Inc. *Detailed Explanation of the Finite Element Method*. 2017. https://www.comsol.com/multiphysics/finite-element-method, Online; accessed June 2017.

[40] John David Jackson. *Classical Electrodynamics*. John Wiley Sons, Inc., third edition, 1999.

[41] Jian-Ming Jin. *Theory and Computation of Electromagnetic Fields*. Wiley-IEEE Press, online edition, september 2010.

[42] Jianming Jin. *The Finite Element Method in Electromagnetics*. John Wiley Sons, Inc., 1993.

[43] P. B. Johnson and R. W. Christy. Optical constants of the noble metals. *Phys. Rev. B*, 6:4370–4379, Dec 1972.

[44] Steven G. Johnson. Notes on perfectly matched layers (pmls). MIT OpenCourseWare, 2007. http://math.mit.edu/ stevenj/18.369/pml.pdf.

[45] Boris N. Khlebtsov and Nikolai G. Khlebtsov. Multipole plasmons in metal nanorods: Scaling properties and dependence on particle size, shape, orientation, and dielectric environment. *J. Phys. Chem. C*, 111:11516–11527, 2007.

[46] M. Kildemo, C. Cobet, N. Esser, M. Juan, and N. Podraza. The dielectric function of gasb in the thz, ir, nir-vis-uv and vuv range determined by spectroscopic ellipsometry. (manuscript in preparation).

[47] Morten Kildemo, Jean-Philippe Banon, Alexandre Baron, Brage B. Svendsen, Thomas Brakstad, and Ingve Simonsen. Optical response of gold hemispheroidal lattices on transparent substrates. *Applied Surface Science*, 2017.

[48] Charles Kittel. *Introduction to Solid State Physics*. John Wiley Sons, Inc., eighth edition, 2005.

[49] Th. Kokkinakis and K. Alexopoulos. Observation of radiative decay of surface plasmons in small silver particles. *Phys. Rev. Lett.*, 28:1632–1634, Jun 1972.

[50] Alexander B. Kostinski, Clark R. Givens, and John M. Kwiatkowski. Constraints on mueller matrices of polarization optics. *Appl. Opt.*, 32(9):1646–1651, Mar 1993.

[51] Clark R. Givens Alexander B. Kostinski. A simple necessary and sufficient condition on physically realizable mueller matrices. *Journal of Modern Optics*, 40(3):471–481, 1993.

[52] V. G. Kravets, F. Schedin, and A. N. Grigorenko. Extremely narrow plasmon resonances based on diffraction coupling of localized plasmons in arrays of metallic nanoparticles. *Phys. Rev. Lett.*, 101:087403, Aug 2008.

[53] M. Kretschmann and A. A. Maradudin. Band structures of two-dimensional surface-plasmon polaritonic crystals. *Phys. Rev. B*, 66:245408, Dec 2002.

[54] Stefan A. Maier. *Plasmonics: Fundamentals and Applications*. Springer US, 2007.

[55] A. A. Maradudin, I. Simonsen, J. Polanco, and R. M. Fitzgerald. Rayleigh and wood anomalies in the diffraction of light from a perfectly conducting reflection grating. *Journal of Optics*, 18(2), 2016.

[56] Antonello De Martino, Tatiana Novikova, Sami BenHatit, Bernard Drévillon, and Denis Cattelan. Characterization of gratings by mueller polarimetry in conical diffraction. *Proc. SPIE*, 5752:217–228, 2005.

[57] Kenneth A. Mauritz. Dielectric Responses. https://en.wikipedia.org/wiki/File:Dielectricresponses.svg, Online; accessed August 2017.

[58] Daniel Maystre. Theory of wood's anomalies. In *Plasmonics - From Basics to Advanced Topics*, chapter 2. Springer Series in Optical Sciences, 2012.

[59] M. Meier and A. Wokaun. Enhanced fields on large metal particles: dynamic depolarization. *Opt. Lett.*, 8(11):581–583, Nov 1983.

[60] Francesco Monticone and Andrea Alù. Metamaterials and plasmonics: From nanoparticles to nanoantenna arrays, metasurfaces, and metamaterials. *Chin. Phys. B*, 23(4), 2014.

[61] NTNU Nanolab. E-Beam Evaporator. http://www.norfab.no/technologies/deposition/ntnu-nanolab-2/e-beam-evaporator/, Online; accessed August 2017.

[62] NTNU Nanolab. FEI Helios NanoLab DualBeam FIB. http://www.norfab.no/technologies/characterization/ntnu-nanolab-2/focused-ion-beam-fib-microscopy/, Online; accessed August 2017.

[63] NTNU Nanolab. NanoSurf easyScan 2 Atomic Force Microscope. http://www.norfab.no/technologies/characterization/ntnu-nanolab-2/afm-nanosurf/, Online; accessed August 2017.

[64] Frédéric Nataf. Absorbing boundary conditions and perfectly matched layers in wave propagation problems. direct and inverse problems in wave propagation and applications. *Appl. Math.*, 14:219–231, 2013.

[65] I.S. Nerbø, M. Kildemo, S. Le Roy, and E. Søndergård. In-situ and real time study of the formation of nanopatterns on gasb by ion abrasion. *Opt. Express*, 19, 2011.

[66] I.S. Nerbø, S. LE Roy, N. Foldyna, M. Kildemo, and E. Søndergård. Characterization of inclined gasb nanopillars by mueller matrix ellipsometry. *Journal of Applied Physics*, 108(014307), 2010.

[67] G.A. Niklasson, C.G. Granqvist, and O. Hunderi. Effective medium models for the optical properties of inhomogeneous materials. *Applied Optics*, 20(1), 1981.

[68] T.W.H. Oates, H. Wormeester, and H. Arwin. Characterization of plasmonic effects in thin films and metamaterials using spectroscopic ellipsometry. *Progress in Surface Science*, 86(11):328 – 376, 2011.

[69] Wounjhang Park and Jinsang Kim. Negative-index materials: Optics by design. *MRS Bulletin*, 33:907–914, October 2008.

[70] Lord Rayleigh O.M. P.R.S. Iii. note on the remarkable case of diffraction spectra described by prof. wood. *Philosophical Magazine Series 6*, 14(79):60–65, 1907.

[71] Lord Rayleigh. On the dynamical theory of gratings. *Proceedings of the Royal Society of London A: Mathematical, Physical and Engineering Sciences*, 79(532):399–416, 1907.

[72] Raymond C. Rumpf. Computational electromagnetics - lecture notes. University of Texas at El Paso. http://emlab.utep.edu/ee5390cem.htm, Online; accessed August 2017.

[73] Jon A. schuller, Edward S. Barnard, Wenshan Cai, Young Chul Jun, Justin S. White, and Mark L. Brongersma. Plasmonics for extreme light concentration and manipulation. *Nature Materials*, 9, 2010.

[74] Ingve Simonsen. Optics of surface disordered systems. *The European Physical Journal - Special Topics*, 181:1–103, 2010.

[75] Mark I. Stockman. Nanoplasmonics: past, present, and glimpse into future. *Opt. Express*, 19(22):22029–22106, Oct 2011.

[76] Allen Taflove and Susan C. Hagness. *Computational Electrodynamics: The Finite-difference Time-domain Method*. Artech House, 3rd edition, 2005.

[77] Asman Tamang, Minoli Pathirane, Rion Parsons, Miriam M. Schwarz, Bright Iheanacho, Vladislav Jovanov, Veit Wagner, William S. Wong, and Dietmar Knipp. Zinc oxide nanowire arrays for silicon core/shell solar cells. *Optics Express*, 22(S3), May 2014.

[78] Harland G. Tompkins and Eugene A. Irene. *Handbook of Ellipsometry*. William Andrew Publishing, Norwich, NY, 2005.

[79] Andreas Trügler. *Optical Properties of Metallic Nanoparticles*. Springer Series in Materials Science, 2016.

[80] A. Wokaun, J. P. Gordon, and P. F. Liao. Radiation damping in surface-enhanced raman scattering. *Phys. Rev. Lett.*, 48:957–960, Apr 1982.

[81] R. W. Wood. On a remarkable case of uneven distribution of light in a diffraction grating spectrum. *Proceedings of the Physical Society of London*, 18(1):269, 1902.